# Sensitivity of ENSO dynamics to wind stress formulation as simulated by a hybrid coupled GCM

Heiko Hansen

Sensitivität der ENSO Dynamik gegenüber der
Parameterisierung der Windschubspannung in Simulationen
mit einem hybrid gekoppelten allgemeinen Zirkulationsmodell

# Sensitivity of ENSO dynamics to wind stress formulation as simulated by a hybrid coupled GCM

Dissertation zur Erlangung des Doktorgrades der Naturwissenschaften
im Departement Geowissenschaften der Universität Hamburg
vorgelegt von

## Heiko Hansen
aus Schleswig

Hamburg 2007

Heiko Hansen
Max-Planck-Institut für Meteorologie
Bundesstrasse 53
20146 Hamburg
Germany

# Sensitivity of ENSO dynamics to wind stress formulation as simulated by a hybrid coupled GCM



Nino 3 SSTA, period as function of mean wind stress
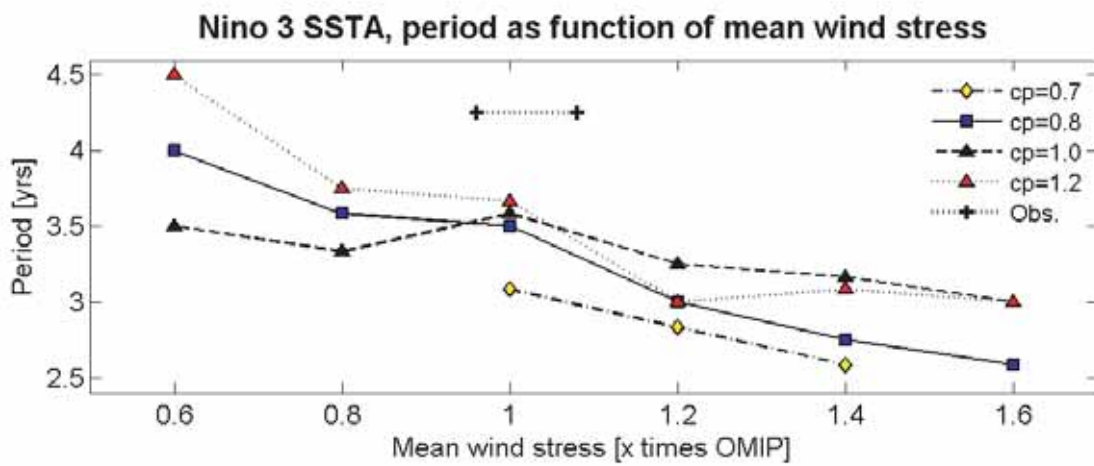
# Heiko Hansen

Hamburg 2007

# CONTENTS

# Abstract

The sensitivity of the El Niño/Southern Oscillation phenomenon (ENSO) with respect to different wind stress formulations is simulated by a hybrid coupled general circulation model (HCM). The HCM consists of a version of the MPI-OM general circulation model (GCM) coupled to a statistical atmosphere model. The design of the HCM allows mean wind stress and the anomalous sea surface temperature (SST) to wind stress coupling to be prescribed.

Two main aspects are addressed: First, ENSO variability and equatorial Pacific ocean thermal structure are investigated with respect to variations in the mean background climatology, and second, improved parameterizations of the momentum flux at the ocean to atmosphere boundary in GCMs of the tropical Pacific are analyzed.

To address the first aspect, the climatology of the tropical Pacific is varied via the strength of the mean wind stress and the ocean-to-atmosphere coupling. The results of the coupled model simulations show that the ENSO period decreases as the mean wind stress is increased. Furthermore, the zonal SST gradient along the equator as well as the mean thermocline depth increase with increasing mean wind stress, while the thermocline intensity is reduced. The ENSO amplitude is more sensitive to the anomalous ocean to atmosphere coupling, where a stronger coupling leads to higher amplitudes. The results are compared to recent studies with intermediate complexity models (ICMs) and to results from intercomparison studies with coupled atmosphere ocean GCMs (AOGCMs). At first view, the prediction of ENSO period from the ICM contradicts the HCM results. This is explained by the setup of the ICM, where the thermocline intensity is prescribed by a parameter, while in the HCM the thermal intensity is modelled. The AOGCMs do not exhibit relationships similar to the results of the HCM.

To address the second aspect, the common bulk formula for wind stress is corrected for a moving ocean surface and improved parameterizations of the drag coefficient $C_d$. Sensitivity studies are carried out for various parameterizations in coupled and uncoupled mode, to give an overview of possible changes. The results of the uncoupled simulations suggest that the correction for a moving surface and the improved parameterization generally lead to reduced mean wind stress and reduced ENSO variability. The correction partly improves the equatorial east Pacific SST and thermal structure. Accounting for surface motion also reduces the variability in coupled simulations. In some experiments the system moves from a self sustained to a damped ENSO mode. The results partly sustain findings in recent sensitivity studies with the ECHAM5/MPI-OM AOGCM, which account for surface motions. The results emphasize the need for an accurate parameterization of the momentum flux also for very low wind speeds.

# 1. INTRODUCTION

The El Niño/Southern Oscillation (ENSO) phenomenon is known to be the largest climatic fluctuation on interannual time scales. It appears as an anomaly of the sea surface temperature (SST) of the whole equatorial Pacific, but most notable in the eastern equatorial Pacific. El Niño appears irregularly every 2 to 7 years and is now understood as an internal mode of the tropical Pacific ocean-atmosphere system (Neelin *et al.* (1998)). Under normal conditions the equatorial easterly trade winds transport vast amounts of warm water to the tropical western Pacific, a region thereby known as the western Pacific warm pool (Yan *et al.* (1992)). Due to its persistent sea surface temperatures (SSTs) higher than 28°C the warm pool is a region of intense deep atmospheric convection and rainfall (McPhaden *et al.* (1998)). Further to the east the SST is decreasing, until in vicinity of the Galápagos islands and the coasts of Peru a tongue of cold water with a mean SST of 23°C predominates (Dijkstra and Burgers (2002)). Associated with the SST gradient is a sea level pressure (SLP) gradient with low SLP over the warm pool and high SLP over the eastern equatorial Pacific.

During El Niño the equatorial warm-pool-cold-tongue temperature gradient is weakening and anomalously warm waters are observed in the central to eastern Pacific. This is accompanied by a weakening of the surface pressure gradient and thereby a slackening of the trade winds, which further enhances the warming in the eastern equatorial Pacific through reduced upwelling of cold water and a less shallow thermocline. The variable SLP field was first discovered by Sir Gilbert Walker (Walker (1924)) who named it Southern Oscillation. The pioneering works of Bjerknes (Bjerknes (1969)) and Wyrtki (Wyrtki (1975)) finally revealed the connection between El Niño and the Southern Oscillation.

These anomalous tropical conditions have profound influence on the global weather variability. The fields of deep atmospheric convection and precipitation over the warm pool are shifting eastward and thus dry conditions occur over the tropical western Pacific regions, while wet conditions occur over the central and eastern Pacific and the western South American coasts. However, the ENSO anomaly also affects the general atmospheric circulation and thus the signal is communicated via atmospheric bridges to the whole extra tropics (Trenberth *et al.* (1998)). Walker already recognized the relation to Indian monsoon rainfall, however, the significant

teleconnections are detected in North and South America, South Africa, East China, Japan and Europe (Trenberth *et al.* (1998); Diaz *et al.* (2001); Merkel (2003)). Since ENSO globally affects weather patterns and climate conditions its influence on society, economy and environment are numerous (e.g. Glantz (2000)). Recently, the worldwide economic losses from the record El Niño in 1997/98 have been estimated to 36 billion US-Dollar (Office of Global Programs (1999)). However, for instance the US economy actually benefited from El Niño, mainly due to the El Niño-induced reduction of Atlantic hurricane activity and reduced heating costs (Chagnon (1999); Goddard and Dilley (2005)). Chagnon (1999) pointed out, that the net benefit was especially a result of the predictions of ENSO, which are now regularly carried out (Latif *et al.* (1998); Landsea and Knaff (2000); Cane (2005)). Advances in the understanding and predicting of ENSO in recent time was a result of the large observational efforts and the many human and technical resources around the world that where activated in the recent decades. However, despite the efforts, elementary questions have yet not been solved. Some of these questions regard the onset and termination of individual ENSO events as well as the general amplitudes and periods. Furthermore, it is unclear how ENSOs behavior might change due to a variable mean background state. It is known, that the climatic background changes on decadal and longer time scales. Also, it is now generally accepted that the anthropogenically emitted greenhouse gases will generally warm the atmosphere by 1.5 to 4.5°C within the next century (Houghton *et al.* (2001)). Attempts to quantify the effect on the tropical Pacific system have not yet come to a settled conclusion. Recent multi-model ensemble studies (Collins and The CMIP Modeling Groups (2005); van Oldenborgh *et al.* (2005)) indicate a slightly more El Niño-like mean state and slightly higher ENSO frequency, but the issue is far from being settled.

In this thesis, two main aspects are addressed: First, the behavior of El Niño under an altered mean climatic background state is investigated.

The second aspect addresses some problems of El Niño simulations in state-of-the-art atmosphere ocean general circulation models (AOGCMs). Recent intercomparison studies (Latif *et al.* (2001); AchutaRao and Sperber (2002); Davey *et al.* (2002)) showed that there are still a number of problems in simulating a correct ENSO signal with respect to spatial location and extension of the anomalies, their amplitudes and periods. One important factor may be the bulk parameterization of surface wind stress in AOGCMs, which, in the past, generally neglected surface current motions. Here, alternative bulk formulas are investigated, which take surface currents and improved drag parameterizations into account.

To investigate these aspects, a hybrid coupled model (HCM) of the tropical Pacific basin is developed, which combines the advantages of a fully developed ocean model with a simple but reasonable atmosphere model. In its complexity, the HCM bridges the gap between coupled models of inter-

mediate complexity and the fully coupled AOGCMs. A number of model runs with the HCM is carried out, to give an overview of possible changes due to the formulation of the wind stress. The simulations are investigated with respect to the amplitude and period of El Niño and the mean ocean thermal structure.

The thesis is organized as follows: In Chapter 2 the hybrid coupled model is introduced and the performances in coupled and uncoupled mode are discussed. In Chapter 3 the behavior of the tropical Pacific mean state and the El Niño variability are investigated under altered mean and anomalous wind stress products. The results are compared to ICM studies as well as to results from recent AOGCM intercomparison studies. Chapter 4 addresses the question of improved wind stress parameterizations. Surface motions are taken into account and the drag coefficient in the wind stress bulk formula is altered with respect to recent studies of drag functions. Again, the influence on the general mean thermal structure and on ENSO variability are shown. Chapter 5 gives a summary and outlook.

# 2. THE HYBRID COUPLED MODEL

## 2.1 Introduction

The aim of this chapter is to introduce the hybrid coupled ocean-atmosphere model used in this study. The term hybrid coupled model (HCM) was created by Neelin (1990) and generally refers to a type of model where the ocean component is of much higher complexity than the atmospheric component. Thereby, the physical and numerical complexity of a HCM lies between the models with reduced physics, such as intermediate complexity models (ICMs, e.g. Zebiak and Cane (1987); Jin and Neelin (1993); Fedorov and Philander (2001)) and fully coupled atmosphere-ocean general circulation models (AOGCMs, e.g. Stockdale *et al.* (1998); Delecluse *et al.* (1998)). HCMs of the tropical Pacific combine the advantages of a fully developed ocean GCM with the conceptual ideas of the El Niño mechanism: On monthly or longer time scales the atmosphere is considered as a system in quasi-equilibrium, which is strongly forced by the ocean sea surface temperature (SST) (Bjerknes (1969), Wyrtki (1975), Philander (1990)). HCMs are now regularly used, both for ENSO studies as well as for ENSO predictions (e.g. Latif *et al.* (1998); Syu *et al.* (1995); Eckert and Latif (1997); Blanke *et al.* (1997); Tang *et al.* (2001); Harrison *et al.* (2002)). The following section gives a description of the ocean and atmosphere components of the model. The coupling procedure and the general experimental setup are explained, followed by a description of the model performance in uncoupled and coupled mode.

## 2.2 The ocean model

The ocean model used in this study is based on the Max-Planck-Institute ocean model (MPI-OM) as described in Marsland *et al.* (2003). The MPI-OM is a z-coordinate global general circulation model based on the primitive equations for a Boussinesq-fluid on a rotating sphere. It includes parameterizations of sub grid-scale mixing processes, like isopycnal diffusion of the thermohaline fields, eddy-induced tracer transport, and a bottom boundary
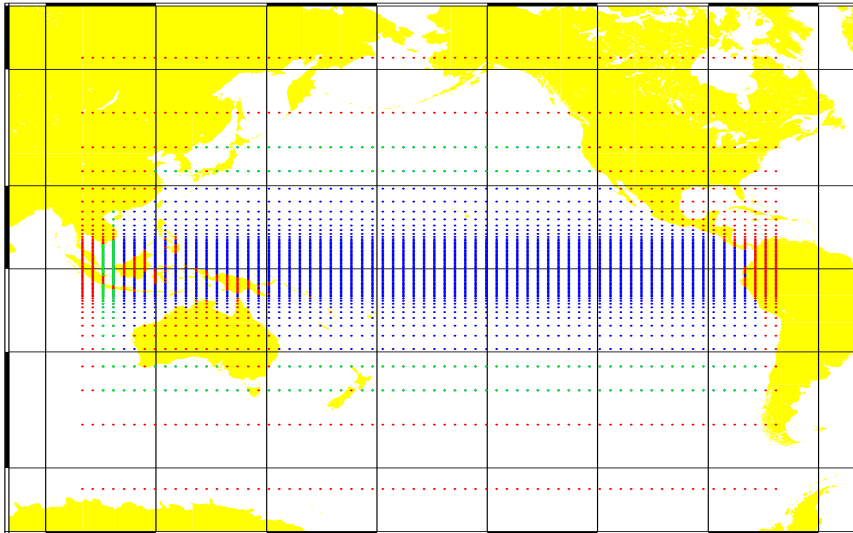
**Fig. 2.1:** *The curvilinear orthogonal grid of the MPI-OM used in this study. The equatorial resolution is 0.5° in latitude between 10° N-10° S. The longitudinal resolution is 2.8°.*

layer slope convection scheme. The model contains a free surface and a state-of-the-art sea ice model with viscous-plastic rheology and snow.

For the purpose of this study, the MPI-OM was restricted to the tropical Pacific basin between 105°E to 77°W, 40°N to 40°S. A sponge layer is applied at the meridional boundaries. The zonal grid resolution is 2.8°. In latitude the grid spacing is 0.5° between 10°S to 10°N, and then non-linearly increases to 7.1° at 40°N and 40°S. The grid is sketched in Figure 2.1. The model has 23 vertical layers, with layer thickness increasing with depth; 10 layers are located in the first 300 meter. As described in Marsland *et al.* (2003) the ocean model is driven by the fluxes of latent and sensible heat, momentum and freshwater at the ocean-atmosphere boundary. In this study the climatological surface fluxes from the ocean model intercomparison project (OMIP, Röske (2001, 2006)) are used. The OMIP fluxes are based on the ECMWF reanalysis project (Gibson *et al.* (1997); Uppala (2001)).

## 2.3 The wind stress model

The wind stress model is an anomaly model and statistical in nature. Earlier works by Latif and Villwock (1990) and Latif and Fluegel (1991) showed that tropical wind stress anomalies can, to a good approximation, be modeled as a linear response to SST anomalies. To relate wind stress to SST anomalies, Barnett *et al.* (1993) used empirical orthogonal function (EOF, see e.g. Preisendorfer (1988); Peixoto and Oort (1992); von Storch and Zwiers (1999)) decompositions to build a statistical model. First, anomalies of wind stress, $\tau$ and SST, $T$, are decomposed into their EOFs and principal components (PCs):

$$T(x,t) = \sum_m \alpha_m(t)\, e_m(x) \tag{2.1}$$

$$\tau(x,t) = \sum_n \beta_n(t)\, f_n(x) \tag{2.2}$$

where $\alpha_m(t)$ and $\beta_n(t)$ denote the n-th and m-th temporal principal components. The spatial EOFs $e_m(x)$ and $f_n(x)$ are the eigenvectors of the corresponding covariance matrices for the anomalous SST and wind stress vectors. From this, a matrix of regression coefficients can be estimated as:

$$C_{n,m} = \frac{<\alpha_m \beta_n>}{<\alpha_m^2>} \tag{2.3}$$

where $< \ldots >$ denotes the time average. Note that in Chapter 3 and 4 the regression coefficient of the first principal components of wind stress and SST, $C_{1,1}$, will be calculated and used as a measure of the ocean-to-atmosphere coupling. Thus, with a given SST anomaly $\hat{T}(x,t)$ a linear wind stress anomaly $\hat{\tau}(x,t)$ can be obtained via the following sequence of equations:

$$\hat{\alpha}_m(t) = \sum_x \hat{T}(x,t)\, e_m(x), \tag{2.4}$$

$$\hat{\beta}_n(t) = \sum_m C_{n,m}\, \hat{\alpha}_m(t), \tag{2.5}$$

$$\hat{\tau}(x,t) = \sum_n \hat{\beta}_n(t)\, f_n(x). \tag{2.6}$$

Since the spatial distribution of geophysical data on a sphere is usually not uniform it is necessary to weight the data with respect to the spatial area they represent (Cohen and Jones (1969); Buell (1971)). For this, the equations 2.1 to 2.6 need to be extended as described in Appendix 6.
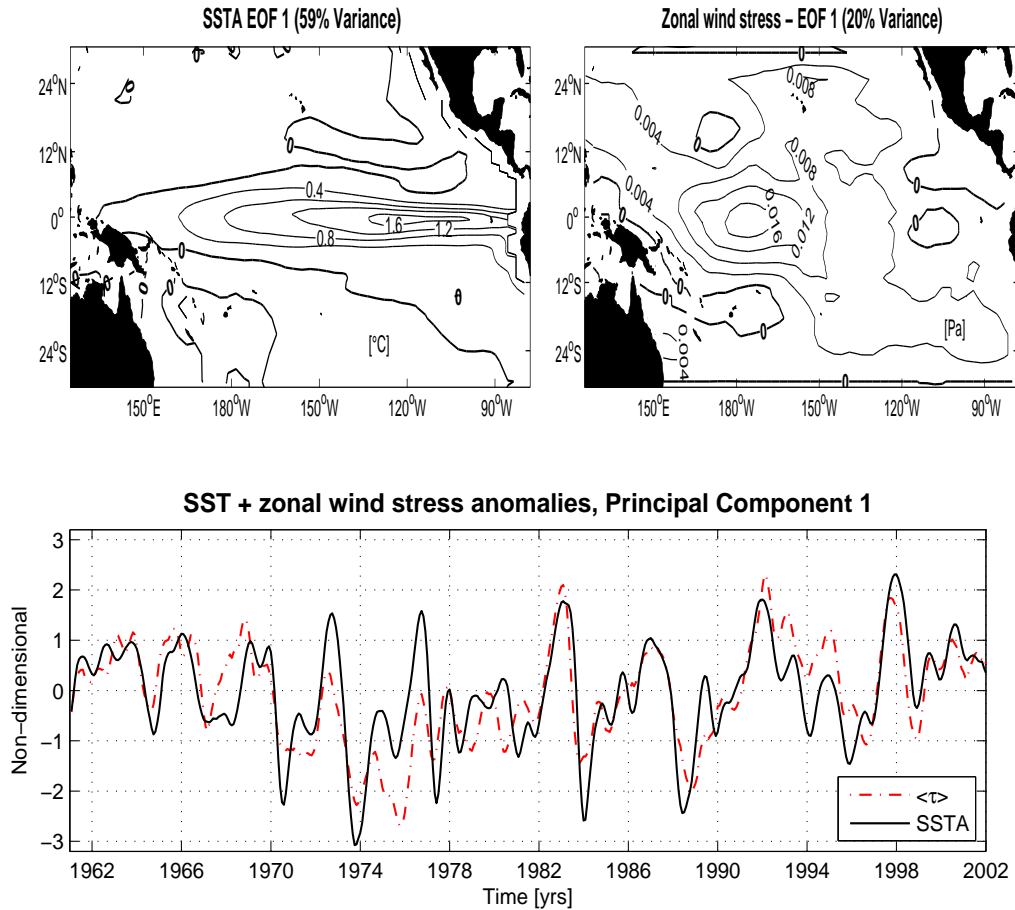
**Fig. 2.2:** *First empirical orthogonal function for SST (upper left panel) and zonal wind stress (upper right panel) anomalies. Lower panel: Principal components of SST and zonal wind stress anomalies ($< \tau_x >$). For this plot, the PCs and EOFs are scaled so that the PCs have unit normal distribution.*

In this study, the pseudo wind stress product of the Florida State University (FSU) is used (Stricherz *et al.* (1997)). The FSU pseudo wind stress consists of 41 years of monthly mean data from January 1961 to December 2001. To obtain wind stress, the pseudo wind stress is multiplied with a drag coefficient of $C_d = 0.0013$ and an air density $\rho = 1.026 kg/m^3$. The SST data is taken from an ocean model run forced by climatological fluxes plus the FSU wind stress. To obtain the anomalies for the regression, the two data sets are smoothed with a 5-month running mean, detrended and the seasonal cycle is removed. Following Barnett *et al.* (1993) the first 5 EOFs of SST and wind stress are used for the construction of the model. As an example, the first EOF of wind stress and their respective SST anomalies and their PCs are shown in Fig. 2.2. It can be seen that the maximum in the zonal wind stress EOF is located in the western equatorial Pacific, while the maximum in the SST EOF is located in the eastern equatorial Pacific.

## 2.4   Coupling considerations

The ocean-atmosphere coupling is accomplished as follows: the SST anomaly is calculated from the model SST, with respect to a prescribed climatological SST. Subsequently, the wind stress anomalies are calculated via the equations 2.3. The anomalies are added to the OMIP climatological wind stress forcing and this is fed back to the ocean model. There are two considerations which have to be taken into account: First, due to the missing noise variance in the neglected EOFs the wind stress model systematically underestimates the total variance. Two common procedures to scale the variance up, are to add a noise term to the modelled wind stress, or to multiply the wind stress by a constant factor, usually termed coupling coefficient. In this study no noise term is applied, instead the modelled wind stress is multiplied with a coupling constant, generally in the range between 0.7 and 1.2, but 1.4 in some experiments. The motivation for this is to study the eigenmodes of the coupled system. The addition of noise may mask their characteristics.

The second point concerns the calculated SST anomalies. The anomalies are calculated with respect to a reference background state, which itself is the climatological SST calculated a priori from an uncoupled run. However, in coupled mode the models internal background state may differ from the uncoupled state. It is known that the annual cycle of SST is the complex nonlinear response of the climate system to the annual solar forcing (Pezzulli *et al.* (2005)). There is no a priori reason, why the SST cycle should stay the same from year to year. It is especially known that seasonal and interannual mode interfere, most prominently visible in the general peak of El Niño during the boreal winter time. (Rasmussen and Carpenter (1982); Philander (1990); Xie (1995); Tziperman *et al.* (1997)). It is noted that this interference may explain aspects of El Niño's irregular behavior through nonlinear interactions which lead to chaotic behavior (Tziperman *et al.* (1994); Jin *et al.* (1994); Neelin *et al.* (1998)). A difference between a prescribed reference background state and the mean state of the model would result in a biased SST anomaly with non-zero mean. It is therefore desirable to have a reference background state that adapts to the mean state of the coupled model. In this study the accumulated mean (ACME) adaption scheme described by Maćias *et al.* (1999) and Maćias (2000) is applied. Suppose $T_n$ is the SST of the current model year and $\tilde{T}_{n-1}$ the reference state SST of the previous year, then the next year's reference state is calculated as

$$\tilde{T}_n = \alpha_n \tilde{T}_{n-1} + (1 - \alpha_n)T_n \tag{2.7}$$

where

$$\alpha_n = \frac{n + m}{n + m + 1}. \tag{2.8}$$

Here $n$ denotes the current model year and $m$ is a constant. Following Maćias *et al.* (1999) $m = 2$ is taken. As pointed out by Maćias *et al.* (1999) the adaptable reference state is converging to the long term mean of the model and thus, the anomalies are unbiased.

In coupled mode, the model is first spun up with five years of climatological forcing to get an approximation of the reference state, followed by five years of FSU forcing to give the system an initial perturbation. Generally, the length of a model simulation without the initial phase is 480 month, but is extended where reasonable.

## 2.5 Model validation

The aim of this section is to validate the model results in coupled and uncoupled mode. Key components of the Pacific ocean atmosphere system are the climatological states of SST, wind stress and thermocline structure. Thus, the validation is mainly focused on these variables, which are compared to observations. First, a brief description of conceptual models for ENSO is given. The theoretical results of the conceptual models will be used as a reference in the discussion of the coupled simulations.

### 2.5.1 ENSO theory

During the recent decades a number of conceptual models have been developed, which explain the main features of the oscillatory behavior of the equatorial tropical Pacific climate. These conceptual models include the delayed-action oscillator (Schopf and Suarez (1988); Battisti and Hirst (1989)), the recharge-discharge oscillator (Jin (1997)), the advective-reflective oscillator (Picaut *et al.* (1997)) and various more (e.g. Dijkstra and Neelin (1999); Wang (2001)). To compare the HCM performance with conceptual frameworks, the model by Jin (1997) is briefly introduced, which can also be seen as a generalization of the delayed-action oscillator model (Kessler (2002)). The Jin model is an extension of the ideas by Bjerknes (1969) and Wyrtki (1975). Bjerknes (1969) stated that an initial SST anomaly in the equatorial Pacific induces an anomaly in the prevailing trade winds, which further enhances the SST anomaly. Furthermore, Wyrtki (1975) noted that prior to an El Niño a buildup of warm water in the western Pacific warm pool occurred, which is released during El Niño. Variations in the warm water volume (WWV) set the interannual timescale between cool and warm states and thus serve as a memory. Jin (1997) extended the idea of a

recharge-discharge mechanism, where ENSO dynamics can be viewed as a cyclic accumulation and release of warm water, with release during El Niño and accumulation during La Niña events[1]. The oscillatory behavior of the recharge-discharge mechanism stems from the disequilibrium between equatorial trade winds, associated with the SST anomalies, and the zonal mean thermocline depth (on ENSO time scales). The anomaly model of the SST and thermocline depth according to Jin (1997) is:

$$\frac{dh_W}{dt} = -r\left(h_W + \alpha\,\tau\right) \tag{2.9}$$

$$\frac{dT_E}{dt} = -\epsilon\left(T_E - \gamma_h\,h_E\right) \tag{2.10}$$

$$\tau = b\,T_E \tag{2.11}$$

$$h_E = h_W + \tau \tag{2.12}$$

Here, $h_W, h_E$ are the anomalous depth of the thermocline in the western and eastern Pacific, respectively. $T_E$ is the eastern Pacific temperature anomaly, $\tau$ is the anomalous wind stress, and the coefficients $r, \alpha, b$ and $\epsilon$ denote coupling parameters, estimated from observed or modelled data (see e.g. Jin (1997); Mechoso *et al.* (2003); Burgers *et al.* (2006)).

The recharge-discharge oscillator has four phases, which are illustrated in Figure 2.3. During the El Niño phase (Fig. 2.3 a), the thermocline is tilted and the WWV is released poleward. The sketch of the thermocline depth below the boxed images denotes the anomalous thermocline depth (thick black line). Thus, as a result of the released poleward heat, the equatorial heat content is reduced and the thermocline is shallow (Fig. 2.3 b). The transition to the La Niña phase (Fig. 2.3 c) due to increased entrainment of cold water from the depth and the subsequent recharge of the WWV (Fig. 2.3 d) with a deeper than usual thermocline, completes the cycle.

The recharge-discharge oscillator model has two advantages: First, the model is reasonably well sustained by observations (e.g. Meinen and McPhaden (2000); Meinen *et al.* (2001); Kessler (2002)). Second, it can be used to test results from more complex models (Mechoso *et al.* (2003); Burgers *et al.* (2006); Jin *et al.* (2006)).

---

[1] During La Niña, the eastern equatorial SST is cooler than normal and the trade winds are enhanced. La Niña is seen as the opposite phase of El Niño in the ENSO oscillation (Trenberth (1997)).
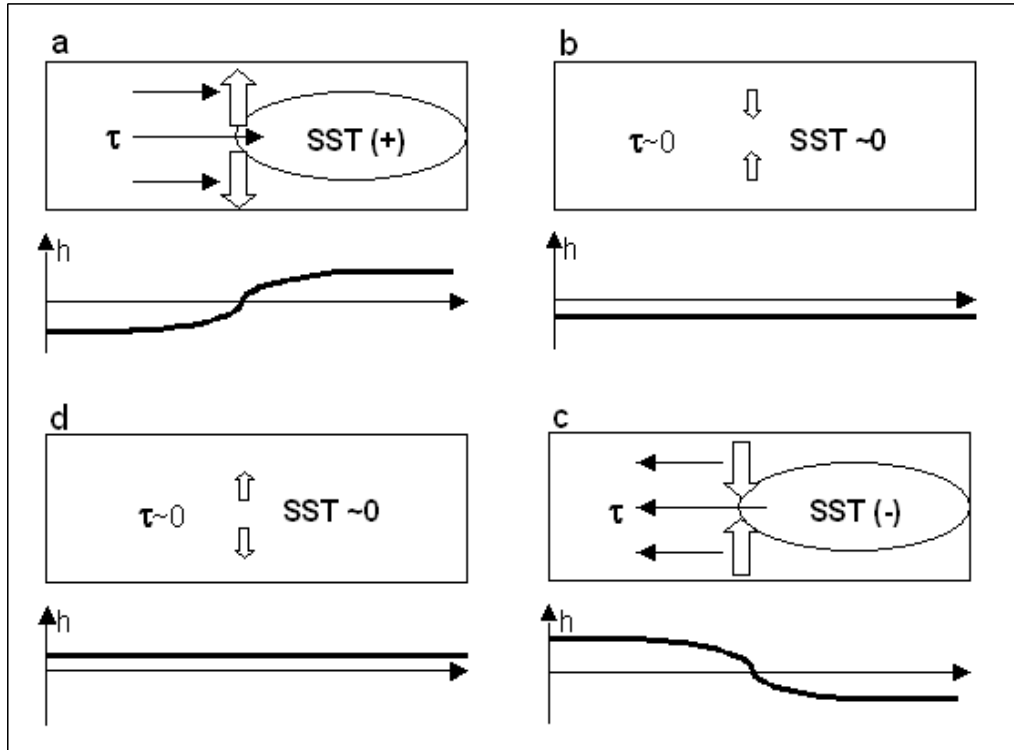
**Fig. 2.3:** *Schematic of the four phases of the recharge-discharge model by Jin (1997). The shown quantities are anomalies relative to the climatological mean. The values in the four boxed images (a-d) are sketches of the Pacific ocean surface. τ represents the wind stress, SST is the positive (+) or negative (-) surface temperature. The upgoing and downgoing arrows denote poleward or equatorward transport of heat. The associated anomalous thermocline depth, h, is sketched below the four boxes. Note that the thermocline (thick black line) is anomalously shallow in panel b) and anomalously deep in d). The eastern Pacific thermocline is anomalously deep in a) and anomalously shallow in c).*

## 2.5.2   Uncoupled model performance

In uncoupled mode, the ocean is forced with the OMIP climatological flux product, plus the FSU wind stress anomalies for the years 1961-2001. The terms uncoupled and forced will be used synonymously. Since wind stress is prescribed, this section focuses on SST and thermocline structure. The mean SST and the bias with respect to observed Levitus observations (Levitus and Boyer (1994)) are shown in Fig. 2.4. While the Pacific warm-pool-cold-tongue features are very well represented, temperatures are about 1-2°C cooler than observed in the eastern Pacific regions. The western Pacific, SST shows a warm bias by 1-1.5°C.

The equatorial temperature sections, zonally along the equator and meridionally at 110°W, reveal a cooler than observed subsurface and a too weak thermocline intensity when compared to Levitus observations (Fig. 2.5). This cold bias and the too weak thermocline intensity are robust features of coupled atmosphere-ocean models (Latif *et al.* (2001); Stockdale *et al.* (1998); Wilson (2000)). The equatorial subsurface at 110°W is warmer than observed (Fig. 2.5 c,d), while the subsurface at 10°N and 10°S is too cool. Attempts to mitigate the cold bias have recently focused on the possibility of missing physics (Jungclaus *et al.* (2006); Luo *et al.* (2005)); these are discussed further in Chapter 4. It is unclear what causes the warm SST bias in the eastern equatorial Pacific. Wilson (2000) concluded that zonally restricted models may suffer from a geostrophic imbalance, which results in an equatorward reflow of warm water to the tropics.

The structure and amplitude of the seasonal cycle of SST are well represented (Fig. 2.6), but too weak by 0.5°C in the east.
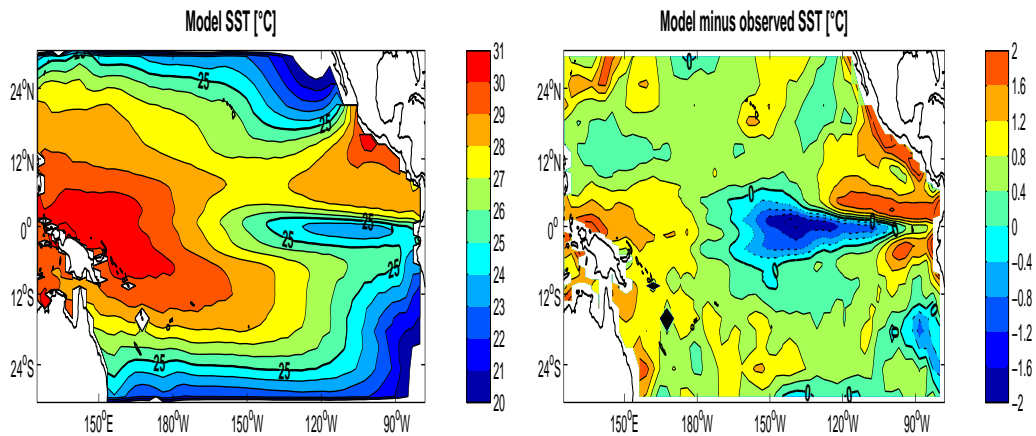


**Fig. 2.4:** *Annual mean SST (left panel) of the uncoupled model and difference to observations (right panel). Observed values are taken from Levitus and Boyer (1994)).*
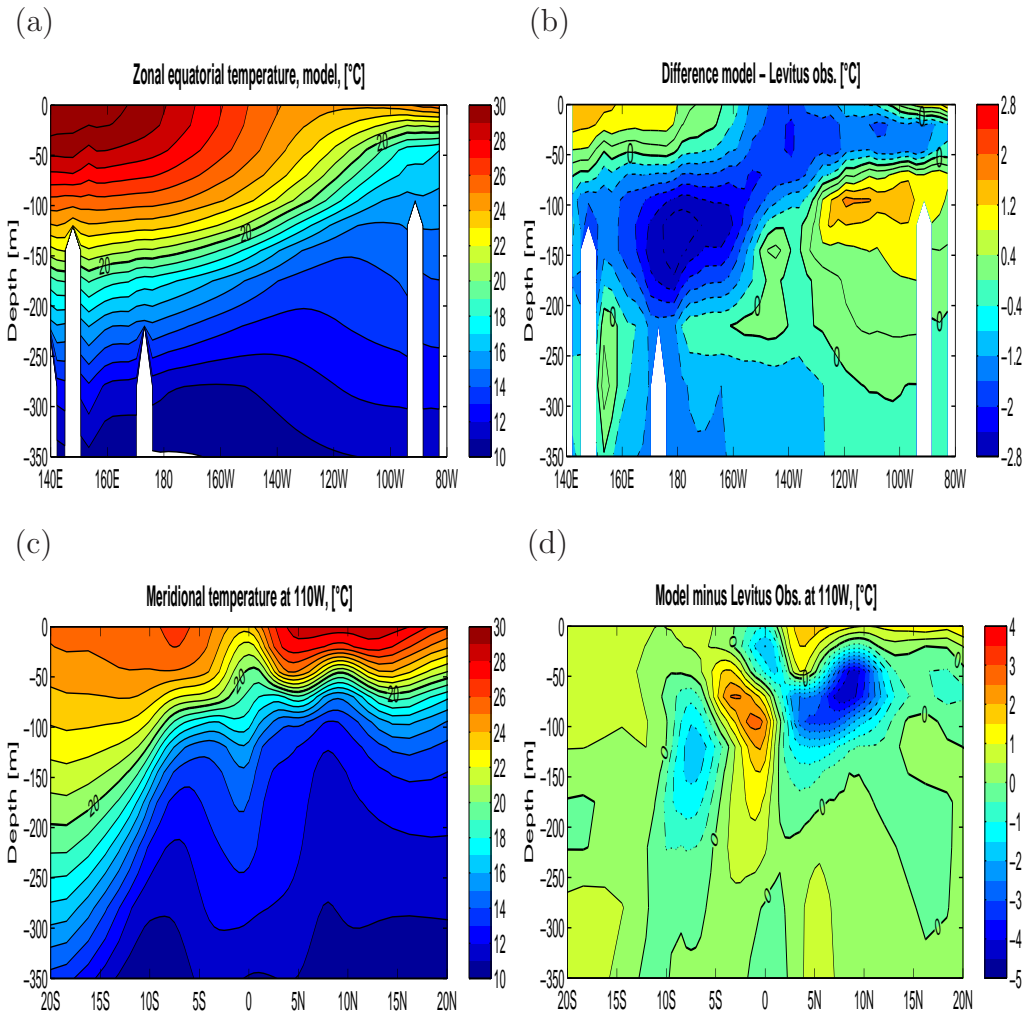
(a)

(b)

**Zonal equatorial temperature, model, [°C]**

**Difference model – Levitus obs. [°C]**

(c)

(d)

**Meridional temperature at 110W, [°C]**

**Model minus Levitus Obs. at 110W, [°C]**

**Fig. 2.5:** *Zonal equatorial temperature structure of the HCM (upper left panel) and the difference to observations (upper right panel). Lower left panel: the temperature at the meridional section at 110° W. Lower right panel: Difference of the meridional section to observations. Observed values are taken from Levitus and Boyer (1994)).*

As a measure of the tropical Pacific SST variability the standard deviation of the monthly SST anomalies is calculated for every grid point. In general, the variability is well represented, but a little too strong and slightly too extended to the west, compared to observations (Fig. 2.7). Furthermore, the modelled variability is more meridionally confined to the equator than in observations. The too strong anomalies result from an apparent deficiency of the model to simulate the skewness of the ENSO variability correct. The uncoupled model has a marginal positive to neutral skewness in the eastern Pacific, in contrast to the observed positive skewness (Burgers and Stephenson (1999); Trenberth (1997)). This deficiency carries over to
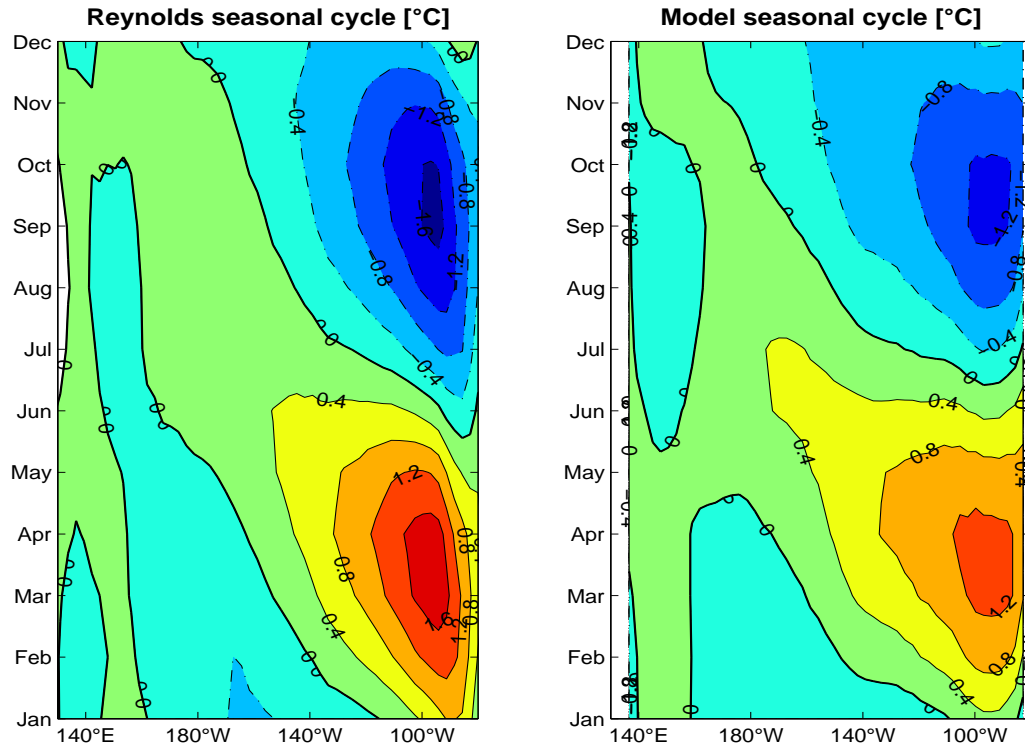
**Fig. 2.6:** *Hovmoeller diagrams of the seasonal cycle of SST at the equator of the uncoupled model (right panel) and the Levitus and Boyer (1994) observed values (left panel). Shown are the anomalies with respect to the annual mean.*

the coupled system, which results in generally negative skewness. The inter-annual variability can be seen from the Nino-3 time series of SST anomalies, which is an average for the area between 5°N-5°S and 90°W-150°W (Fig. 2.8), and in a Hovmoeller diagram (Fig. 2.9). As can be seen, Nino-3 variability is reasonably well represented. The model has slightly too cool La Niñas in comparison to observations, which results in a too high amplitude of 0.95°C for the standard deviation. This is slightly above observed values between 0.7-0.9°C (e.g. Trenberth (1997); Burgers and Stephenson (1999); Latif *et al.* (2001)). The spectrum of the uncoupled model is also reasonable in comparison to observations (Fig. 2.13).

The Hovmoeller diagrams illustrate that the strong El Niño events in 1982-83 and 1997-98 as well as the extended warm phase in the 1990s are well represented in the model. While observations show both very weak eastward or westward propagating modes (Neelin *et al.* (1998)), the HCM shows eastward propagation during the strong warm events and generally westward propagation during modest warm and cold events. The propagation characteristics are not uncommon for models, since the transitions between east- and westward propagation can result already from modest changes of the model parameters (Neelin *et al.* (1998)), p.14277).
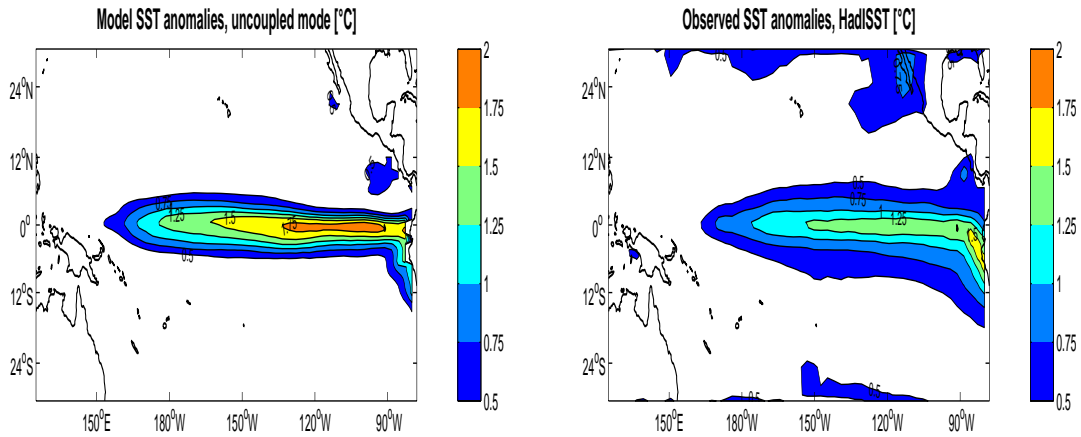
**Fig. 2.7:** *Right panel: Interannual SST variability of the uncoupled model. Shown are the standard deviations for every spatial grid point. Left panel: observed variability (HadISST, Rayner et al. (2003)).*
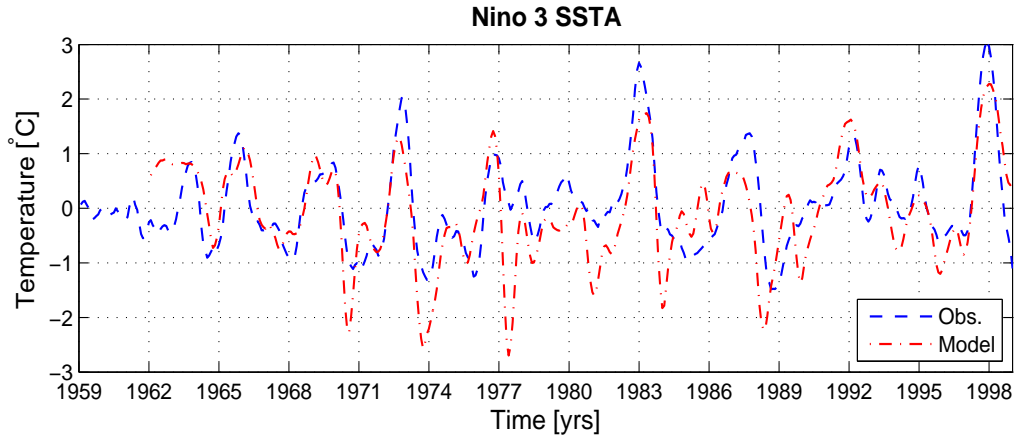


**Fig. 2.8:** *Nino-3 time series of SST from the uncoupled model and from observations. The observed Nino-3 is calculated from the HadISST (Rayner et al. (2003)).*

In Chapter 4 the speed of the surface currents will be taken into account for the calculation of the ocean-to-atmosphere momentum flux. The zonal currents from the model represent the main features of the Reverdin *et al.* (1994) observations (Fig. 2.10). The model has a weaker than observed north equatorial counter current and the southern current is too strong in the eastern Pacific.
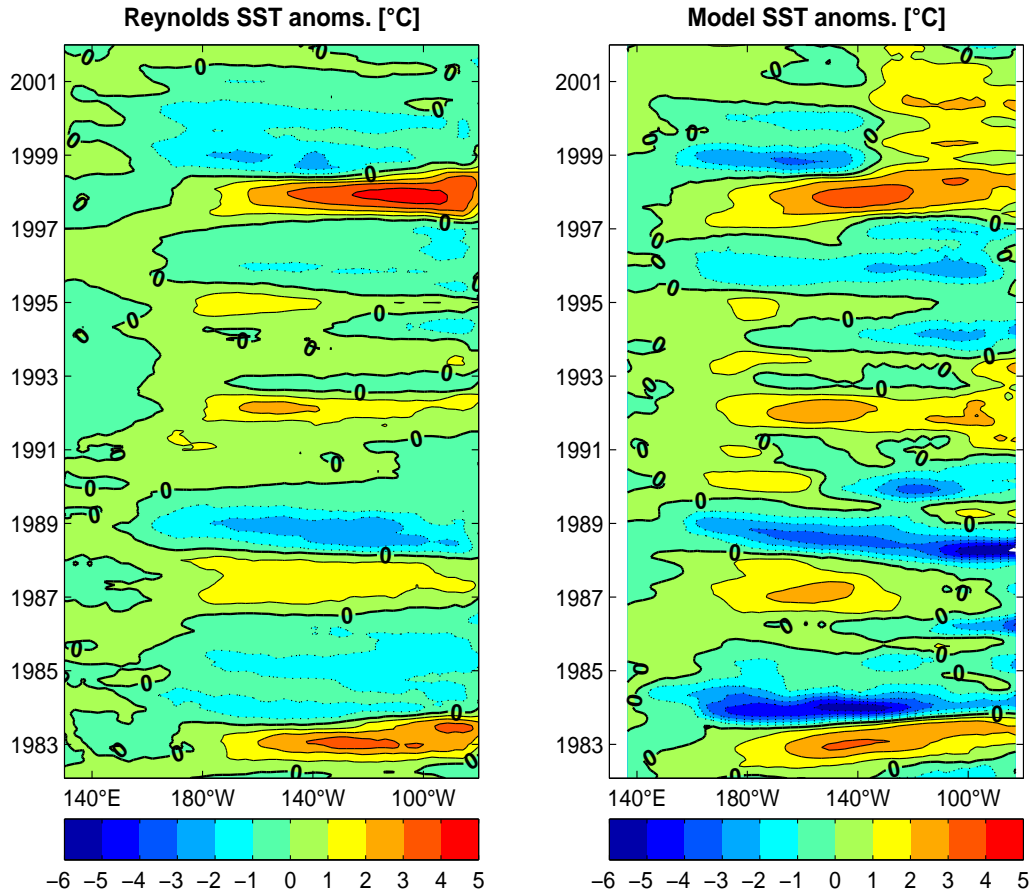
**Fig. 2.9:** *Hovmoeller diagrams of uncoupled model (right panel) and observed (left panel) zonal SST anomalies. Time is going upward. Observations are calculated from Reynolds and Smith (1994).*
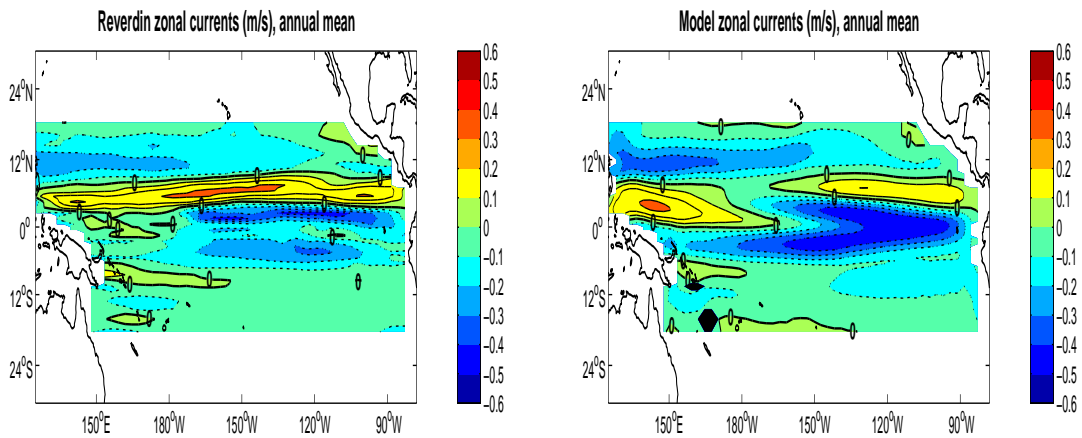
**Fig. 2.10:** *Zonal surface currents from the model (right panel) and Reverdin et al. (1994)) observations (left panel).*

### 2.5.3   Coupled model performance

As mentioned before, the model starts with 5 years of climatological forcing to calculate an a priori background state, followed by 5 years with observed wind stress anomalies to give the system an initial kick. This section is focused on the modelled interannual variability. A further analysis of the seasonal cycle is neglected, however, it is noted that the coupled model runs of Chapter 3 indicate a sensitivity of the seasonal cycle to the prescribed mean state. It was beyond the scope of this thesis to further investigate this sensitivity, but it is noted that potential interactions between mean state and seasonal cycle were also found by Timmermann *et al.* (2004) in AOGCM greenhouse gas experiments.

A typical Nino-3 time series from the coupled model is shown in Fig. 2.11. Although the model has no noise component, the model exhibits an irregular ENSO mode, which stays irregular if the run is extended to 100 years. The time series shows a realistic amplitude, with a standard deviation of 1.01°C, which is slightly above observed values between 0.7-0.9°C (e.g. Trenberth (1997); Burgers and Stephenson (1999); Latif *et al.* (2001)). The spectrum of the coupled model (Fig. 2.13) shows a peak between 3 and 5 years, a typical timescale for ENSO.

The Hovmoeller diagrams for wind stress, SST and thermocline anomalies illustrate that some of the anomalies are too strong in comparison to observations (Fig. 2.12). In particular, the SST anomalies are too cool, with temperatures below -4°C. The SST shows a standing or slightly westward propagating mode. In some events, (year 1-2 and 15-17) the thermocline exhibits an eastward propagation. In comparison to the observed variability (Fig. 2.8 and 2.9) the model shows a reasonable positive anomaly but over-estimates the negative events. Thus, the skewness is negative, in contrast to the observed positive skewness mentioned previously.
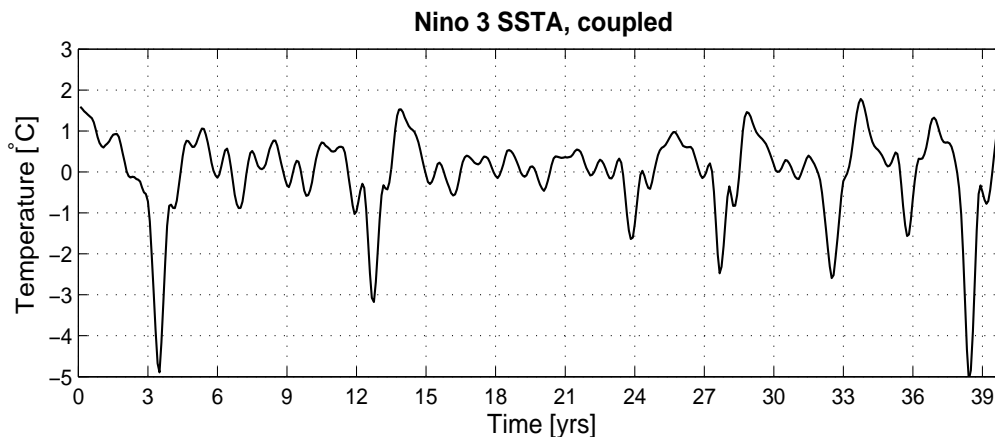


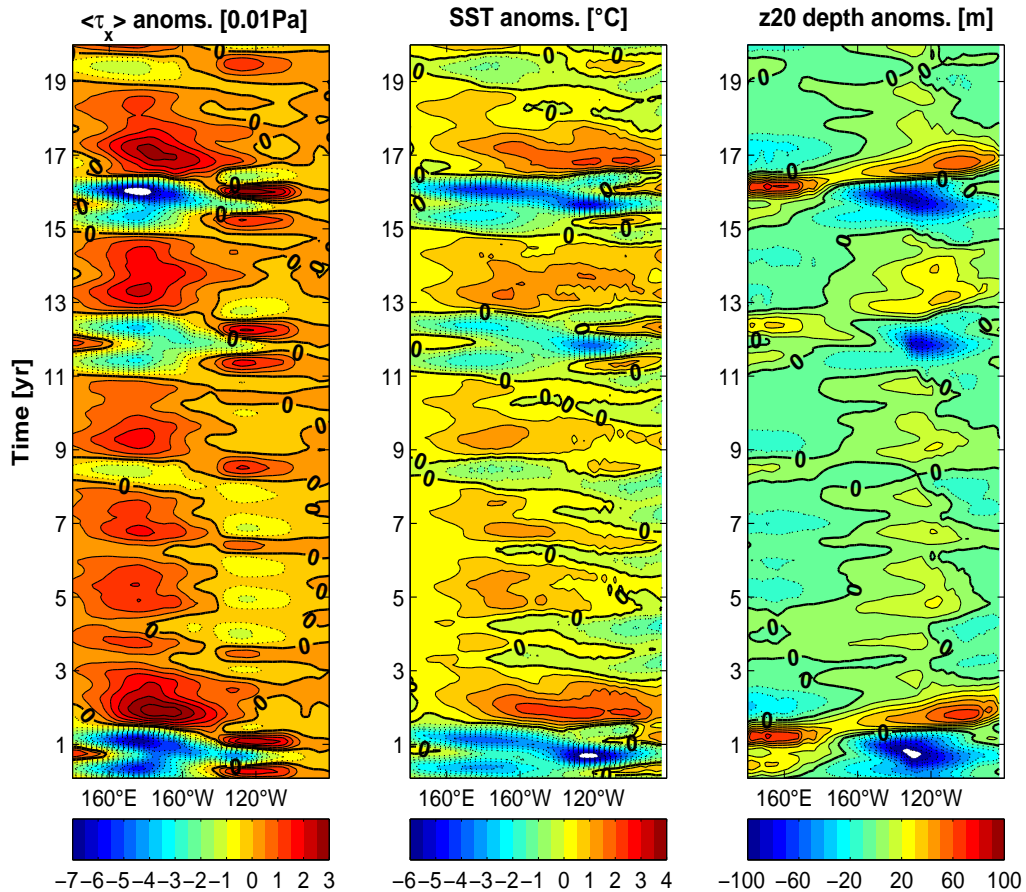**Fig. 2.11:** *Nino-3 time series as simulated by the coupled model.*

**Fig. 2.12:** *Hovmoeller diagrams of zonal wind stress (left panel), SST (middle panel) and z20 anomalies (right right panel) in coupled mode for model years 0-20. Time is going upward.*

Theoretical studies of ENSO underpin the important relationship between the subsurface structure and the surface variability. The theoretical investigation of the Jin model described in Section 2.5.1 emphasizes a recharge of heat and a deepening of the thermocline in the western Pacific prior to El Niño and a discharge and shallowing of the thermocline after the event. Latif *et al.* (2001) computed the correlation of the upper ocean heat content with the Nino-3 SST anomalies for the models and observations, to compare the modelled and observed subsurface structure. For the HCM, the equatorial 20°C isotherm depth averaged between 5°N-5°S is used as a measure for the heat content. As can be seen (Fig. 2.14), the modelled and observed correlations agree well in the eastern equatorial Pacific at zero lag. The model overestimates the correlation in the western and eastern Pacific about 10-20 month prior to the SST event. Meinen and McPhaden (2000) tested the theoretical framework of the Jin (1997) model (described in Section 2.5.1). They used the 20°C isotherm depth (z20) anomaly as a measure for the anomalous slope of the main thermocline. They identified the first
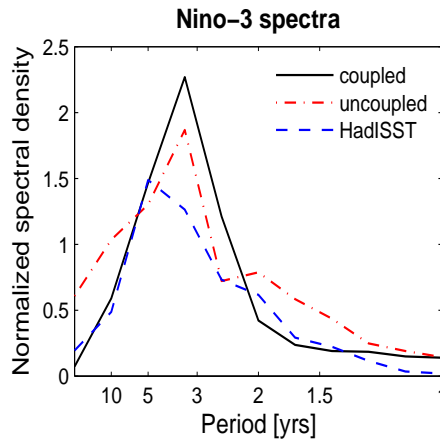
**Fig. 2.13:** *The period of the uncoupled, coupled and observed Nino-3 SST variability. The normalized spectra are estimated via multi taper spectral estimation.*

EOF as the east-west tilting mode depicted in Figure 2.3 a) and c), while the second EOF can be identified as the discharged or recharged system in Figure 2.3 b) and d). Thus, the first EOF of Meinen and McPhaden (2000) (their Figure 3, not shown) shows an east-west dipole structure, with an axis around 155°W, and the second EOF shows a uniform basinwide equatorial structure. Both EOFs in Meinen and McPhaden (2000) account for 28% and 21%, respectively. In Figure 2.15 the EOFs and principal components for the coupled HCM model are shown. While the first EOF of the coupled HCM also shows the east-west tilting structure, the second differs from the observed one. The modelled EOF shows a basinwide structure slightly south of the equator together with an opposite patch at 120°W. Further, the first and second model EOF account for 46% and 23% of the variance, respectively. The principal components in the lower panel of Fig. 2.15 show that PC 1 is leading PC 2 by 4-9 months (correlation > 0.6), which is roughly in agreement with the findings by Meinen and McPhaden (2000) (9 month lead with a peak correlation of 0.77).
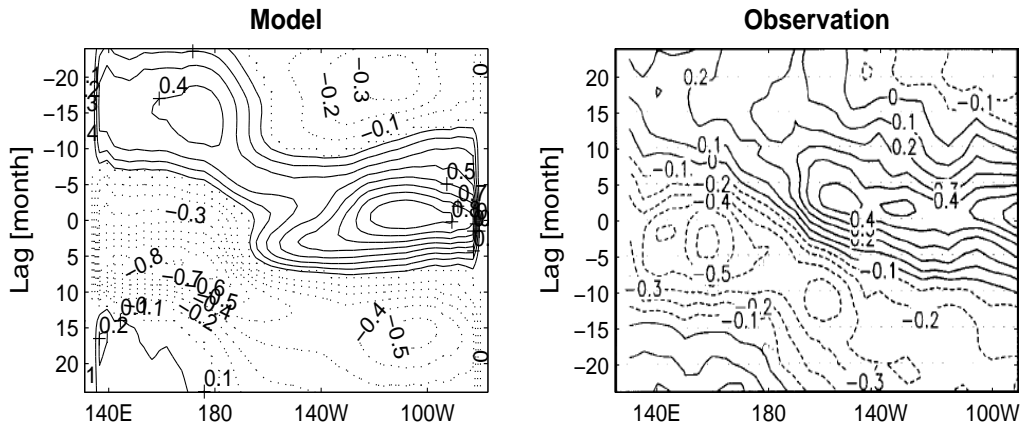
**Model**                    **Observation**



**Fig. 2.14:** *Nino-3 SST anomalies vs. heat content correlation for different time lags. For the model (left panel) the z20 depth was used as measure for the heat content. The observed correlations (right panel) are taken from Latif et al. (2001).*
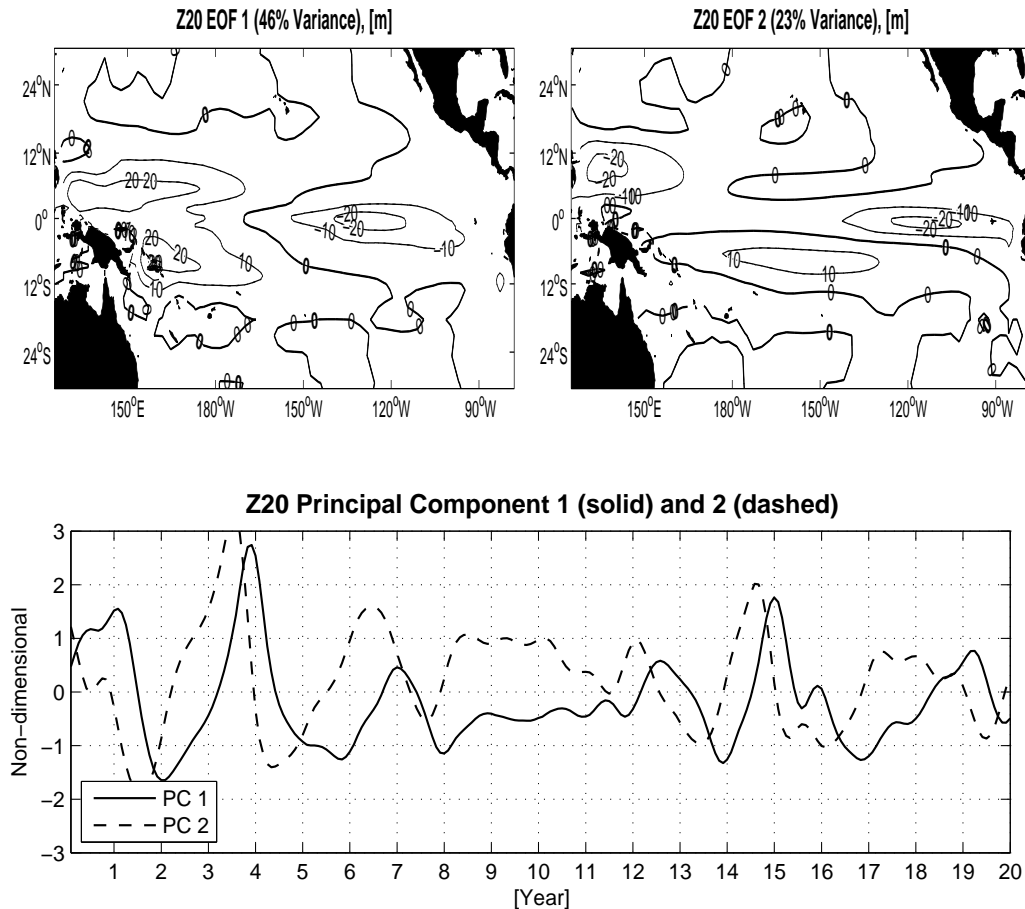
**Z20 EOF 1 (46% Variance), [m]**          **Z20 EOF 2 (23% Variance), [m]**



**Z20 Principal Component 1 (solid) and 2 (dashed)**



**Fig. 2.15:** *Upper panels: First and second EOFs of the $20^\circ C$ isotherm depth from the coupled model experiment. Lower panel: first two principal components of the z20 anomalies.*

# 2.6 Summary

In this chapter, the hybrid coupled model of the tropical Pacific basin was introduced. The model consists of a version of the MPI-OM general circulation model, which is confined to the equatorial Pacific region. The MPI-OM is coupled to a statistical atmospheric model, based on EOF decomposition of observed and modelled anomalies. Model simulations in uncoupled and coupled mode were presented, and the mean climatological values in terms of sea surface temperature, thermal ocean structure, mean wind stress and ocean surface currents were validated against observations. Further, the variability of the coupled model were compared with results from the conceptual recharge-discharge oscillator and observed values. The analysis showed that the mean climatologies are reasonably well represented. However, the model suffers from a cold bias in the eastern equatorial Pacific, which is a common bias in coupled ocean models. Attempts to mitigate this bias are presented in Chapter 4. Furthermore, in coupled mode the model exhibits a reasonable amplitude and period in comparison to observations. A caveat of the model is the wrong skewness of the model, with too strong cold events and slightly to weak warm events. As a consequence, the model shows slightly too high variability. Features of the recharge-discharge model by Jin (1997) and the observational results by Meinen and McPhaden (2000) could be reproduced by the model, but with slight differences of the EOF structure of the anomalous thermocline depth, which serves as a measure of the warm water volume and thus of the recharge-discharge mechanism. It is concluded that the model is reasonably well suited to reproduce the important characteristics of the tropical Pacific system.

# 3. ENSO SENSITIVITY TO WIND STRESS VARIATIONS

**Abstract**

The El Niño/Southern Oscillation (ENSO) phenomenon is the most influential climatic fluctuation on interannual time scales. ENSO characteristics, like frequency and amplitude, depend on the mean climate state of the tropical Pacific, which itself is maintained by various internal and external processes. The question how modifications of the mean state, e.g. due to anthropogenic greenhouse warming or tropical-extratropical interactions, affect ENSO variability is investigated with the hybrid coupled model (HCM). The setup of the HCM allows the prescription of both climatic variations, through changes of the mean wind stress field, and the strength of the anomalous ocean-to-atmosphere coupling. In this chapter the impact of both of these on ENSO variability and mean sea surface temperature (SST) and upper ocean thermal structure are studied in coupled simulations. Various coupled runs are carried out to give an overview of possible ENSO changes in terms of amplitude and frequency as well as changes in the mean SST and ocean thermal structure. The results suggest that ENSO frequency increases with increasing mean wind stress, while ENSO amplitude is more sensitive to the strength of the anomalous coupling. Furthermore, enhanced mean wind stress increases the zonal SST gradient along the equator and deepens the mean thermocline depth, while the thermocline intensity is reduced.

## 3.1 Introduction

ENSO is known to be the most influential climatic fluctuation on interannual timescales. Its occurrence has profound influence on global atmospheric circulation and precipitation patterns (e.g. Philander (1990); McPhaden *et al.* (1998); Cane (2005)). The climatic variations have influence on the seasonal weather patterns around the world, affecting society and economy in both positive and negative ways (McPhaden (2004); Goddard and Dilley (2005)). Although El Niño has been the subject of numerous studies, some basic questions remain unanswered. For instance, the potential change of

interannual variability induced through changes in the mean climatic background state is a matter of debate. Theoretical studies reveal that El Niño is sensitive to the background climatic state upon which it evolves (e.g. Zebiak and Cane (1987); Philander (1990); Dijkstra and Neelin (1995)). Justifications for these results come from observations of the tropical Pacific system in the past. Here, a brief overview of these results is given.

ENSO observations with monthly resolution, which are available for the last 150 years, indicate an apparent tropical climate shift in the 1970s: ENSO frequency decreased, from a period of 2-4 years to 4-6 years (An and Wang (2000)), and the El Niños became generally stronger. Furthermore, the most intense and prolonged ENSO events have been observed in the recent decades (Fedorov and Philander (2000); Trenberth (1997); Cane (2005)). It is now assumed that this change is part of a decadal climatic variation involving the tropical east-west SST gradient and trade wind structure. In the mid-1970s the tropical central and southeast Pacific warmed by 0.5°C, while the structure of the easterly trade winds changed regionally (An and Wang (2000); Wang and An (2001)). The mechanisms underlying tropical Pacific decadal variability are still under investigation (e.g. Rodgers *et al.* (2004); Yeh and Kirtman (2005, 2006); Lohmann and Latif (2005); Matei (2007)).

On longer time scales, the ENSO variability has to be estimated from proxy observations, such as tree rings, geochemical data from corals, ice cores and various others (see e.g. Mann and Jones (2003) for a review). Temperature reconstructions of the last millennium reveal climate variability on multi-centennial timescales. For instance, a northern hemisphere warming that lasted from AD 800-1400 was strong enough to be termed Medieval Warm Period (MWP), while a later cooling between the 16th and 19th century is now generally referred to as Little Ice Age (LIA). These climatic changes are mainly recognized in the northern hemisphere, but the signal can also be identified in the tropics and the southern hemisphere (Houghton *et al.* (2001) and references therein; Jones and Mann (2004)). A proxy reconstruction from fossil-coral data by Cobb *et al.* (2003) reveals a less strong mean equatorial zonal SST gradient during the LIA, while during the MWP the mean zonal SST gradient was enhanced. Furthermore, the reconstructions indicate a generally weaker variability of ENSO during MWP, while frequencies were higher and amplitudes were stronger during LIA. A model study by Mann *et al.* (2005) reveals that variations in solar insolation due to reduced/enhanced volcanic aerosols is forcing the tropical Pacific zonal SST structure and the El Niño variability.

During the Holocene (12.000 years BP until present) a general increase in ENSO activity until 1.200 years BP is noted (Rodbell *et al.* (1999); Adams *et al.* (2003)). The mid-Holocene, i.e. 6.000 BP, seems to have stronger zonal SST gradients and weaker ENSOs than today (Clement *et al.* (2000)). The variability in the mean background state on these time scales is mainly

correlated with the periods of orbital solar radiation changes (Clement *et al.* (1999); Moy *et al.* (2002); Rodó and Rodriguez-Arias (2003)). Further in the past, the reconstruction of both past climatic states and ENSO variability are difficult to obtain and more difficult to interpret. The ENSO signal can be traced back for the past 130000 years (Tudhope *et al.* (2001)). A relationship to the boreal summer perihelion is found, however, it is unclear how to interpret this in the context of potential future climatic changes.

From a theoretical point of view, the SST variability results from an interplay of zonal and meridional temperature advection processes, exchange with deeper layers and with the atmosphere. In a simplified version which neglects the relatively small meridional advection and parameterizes all dissipative processes with a first order damping term, the temperature equation is:

$$\frac{dT'}{dt} + \bar{u}\frac{dT'}{dx} + u'\frac{d\bar{T}}{dx} + \bar{w}\frac{dT'}{dz} + w'\frac{d\bar{T}}{dz} = -\alpha T' \qquad (3.1)$$

In this equation the overbar denotes climatological mean values and the prime deviations therefrom. $\frac{dT}{dx}$ and $\frac{dT}{dz}$ denote zonal and vertical temperature gradients and $u$ and $w$ are the zonal and vertical surface velocities. Thus, the temperature change on ENSO timescales is affected by the mean fluxes of anomalous temperature gradients (term 2 and 4 on the left) and on anomalous fluxes of mean temperature gradients (terms 3 and 5, on the left). It is easy to see that a change in the climatological values feed back onto the anomalous temperature. However, a purely theoretical examination is hardly feasible because the fully coupled dynamics of the tropical ocean-atmosphere system reveal a plethora of connections and interactions, which affects all terms in the temperature equation. It is therefore necessary to use numerical ocean-atmosphere models, which solve the dynamical equations of the climate system.

Recent work by Fedorov and Philander (2000, 2001) with an intermediate coupled model (ICM) gives an overview of possible ENSO period changes due to changes in mean SST, wind stress and thermocline structure. Their results suggest that ENSO is currently close to the point of neutral stability, between a self-sustained mode and a damped mode forced by weather noise. A comparison of the observed ENSO variability in the 1980s and 1990s with results from the ICM suggest that a deepening of the mean thermocline and a weakening of the trade winds caused an increase of the period from 3 to 5 years. However, in the ICM the values of thermocline depth and intensity and the trade winds are prescribed as independent parameters, while in reality they interact as they themselves change the mean state. Coupled GCM studies provide a more realistic picture, but they are computationally expensive and partly suffer from problems in simulating a realistic tropical Pacific climatology and variability (Latif *et al.* (2001); AchutaRao and Sper-

ber (2002)). The few studies with coupled GCMs that have been performed yet to simulate future climatic conditions in the tropical Pacific climate and ENSO variability show an unclear picture (see Houghton *et al.* (2001) for a review). Some indicate a more El Niño-like mean state, with a warmer mean SST in the east, and stronger and more frequent ENSO activity (Timmermann *et al.* (1999); Collins and The CMIP Modeling Groups (2005); van Oldenborgh *et al.* (2005)), while other models show a more La Niña like situation.

In this chapter two questions are addressed: How do frequencies and amplitudes of ENSO vary as a function of the mean background state, and how do the thermal structure and SST vary as functions of the mean wind stress? For this purpose the HCM described in Chapter 2 is used. The setup of the HCM allows to vary the climatological background state through changes in the mean wind stress forcing and to perform extensive experiments, so that an overview of potential changes and sensitivities can be given.

## 3.2 Method

HCM model runs with various climatological mean wind stresses and coupling coefficients are carried out. Mean wind stress is prescribed from the OMIP climatology (Röske (2001, 2006)). For the different experiments the OMIP mean wind stress is multiplied by a factor between 0.6 and 1.6. Furthermore, the experiments are carried out for different values of the coupling coefficient, for Cp=0.7, 0.8, 1.0, 1.2. For Cp=0.7 the simulations with a mean wind stress of 0.6, 0.8 and 1.6 times OMIP did not lead to reasonable oscillatory behavior and are therefore neglected. Table 3.1 gives an overview of the parameterizations for the experiments.

| Exp. | Cp = 0.7 | Cp = 0.8 | Cp = 1.0 | Cp = 1.2 |
|---|---|---|---|---|
| $\tau$=0.6 | – | x | x | x |
| $\tau$=0.8 | – | x | x | x |
| $\tau$=1.0 | x | x | x | x |
| $\tau$=1.2 | x | x | x | x |
| $\tau$=1.4 | x | x | x | x |
| $\tau$=1.6 | – | x | x | x |

**Tab. 3.1:** *Parameterizations of the performed coupled HCM experiments. Cp is the coupling coefficient and $\tau$ denotes the factor by which the original OMIP wind stress is multiplied. The coupled experiments denoted with 'x' are analyzed. Experiments denoted with '-' did not exhibit ENSO variability and were therefore neglected.*

The ENSO periods and amplitudes are estimated from the Nino-3 SST

anomaly time series (temperature averaged for the area between 5°N-5°S
and 90°W-150°W). The period is calculated as the delay of the second
positive maximum of the autocorrelation function and the amplitude is
measured as the standard deviation of the Nino-3 SST anomaly (Nino-3
SSTA). The resulting periods and amplitudes of the Nino-3 SST anoma-
lies are shown as functions of mean wind stress, mean 20°C thermocline
depth (z20), thermocline intensity and zonal SST gradient along the equa-
tor. Following Meehl *et al.* (2001) the mean thermocline depth is calculated
as the annual mean 20°C isotherm depth, spatially averaged between 2°S-
2°N, 120°E-85°W. The thermocline intensity is calculated as the difference
in meters between the 16°C and 22°C isotherm depths, where the isotherm
depths are calculated in the same manner as for the 20°C isotherm depth.
The zonal SST gradient is calculated as the equatorial surface temperature
difference between 170°E and 120°W.

To give an overview of the relationships, the computed values are plotted
and least squares linear regression coefficients are calculated. These results
are compared to other model studies and to observations.

Observed quantities are calculated in the same manner as for the coupled
model experiments, or are taken from the literature. The observed mean
wind stresses are calculated from the NCEP (Kalnay *et al.* (1996)) and
FSU (Stricherz *et al.* (1997)) wind stress products. The observed mean
thermocline depth is calculated from the SODA dataset (Carton and Giese
(2007)). The observed zonal SST gradient is estimated from the HadISST
dataset (Rayner *et al.* (2003)). For these values, upper and lower bounds
were calculated. (See Appendix 6.2.2 for details on the calculations of the
upper and lower bounds.) The observed thermocline intensity is calculated
from Levitus and Boyer (1994). The upper and lower bounds for the Nino-3
amplitudes are taken from Burgers and Stephenson (1999) and Latif *et al.*
(2001). Published values for observed ENSO periods are between 2-7 years
with a peak between 3-5 years (Trenberth (1997)). Here, the observed ENSO
period is calculated from the HadISST dataset (Rayner *et al.* (2003)).

The calculated numbers for the coupled model experiments of this chap-
ter are summarized in the Tables 6.1 and 6.2, in Appendix 6.2.

## 3.3   Results

Figure 3.1 gives an overview of the ENSO periods for the different model
simulations as functions of mean wind stress and mean thermocline depth.
A value of 1.0 corresponds to the original OMIP forcing. Thus, a value of
1.2 means a 20 percent stronger mean wind stress. As can be seen in the
upper panel of Fig.  3.1, the period decreases with increasing mean wind
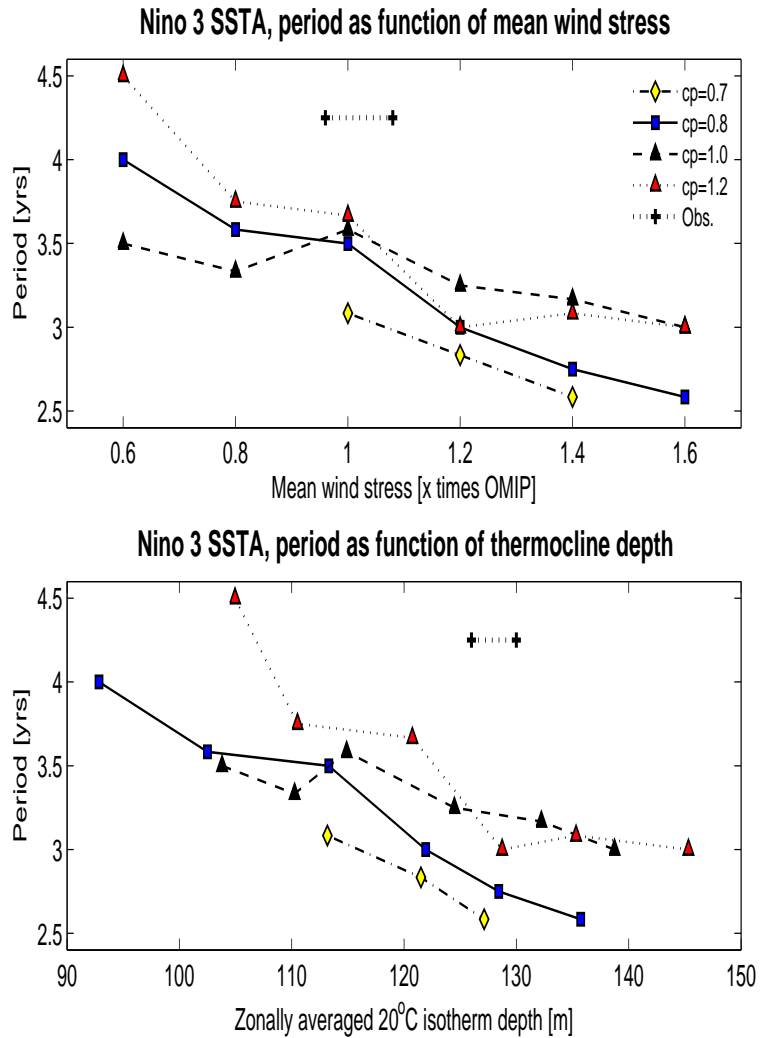stress. For example, the simulations with a coupling coefficient of 0.8, show

**Fig. 3.1:** *Upper panel: Nino-3 period for the coupled model experiments as a function of the mean wind stress. Lower panel: period as a function of the mean thermocline depth. The model simulations with the same coupling coefficient are connected by lines. Ranges for observations are calculated as described in Section 3.2.*

a period of 4.0 years for a mean wind stress of 0.6 times OMIP and decreases to around 2.6 years for a mean wind stress of 1.6 times OMIP.

Using the Nino-3 periods of all experiments as dependent variable and their associated mean wind stresses as independent variable, a least squares linear regression is calculated. On average a mean wind stress increase (decrease) by 10 percent leads to a period decrease (increase) by 1.4 month, with an absolute correlation of 0.82. (The least squares linear estimates of this chapter are listed in Table 3.2 (Sec. 3.5). The associated correlations can be found in Table 6.3, in Appendix 6.2). This result is generally in agreement with the period change in the mid-1970s, where a reduction of

the trade winds in the western equatorial Pacific was accompanied by an increase in ENSO period (An and Wang (2000)).

The coupling coefficient has only weak influence on the period, with a tendency to lower periods for weaker coupling. In the lower panel of Fig. 3.1, the same is shown as a function of the thermocline depth. As a function of the thermocline, the curves show generally the same behavior as for mean wind stress, where a deeper thermocline leads to shorter periods. A linear approximation for all points of the curves is 3.1 month per 10 meter depth variation (Table 6.3).

The period is also found to be linearly related to the east-west SST gradient (Fig. 3.2, upper panel), where the period is decreasing with increasing zonal SST gradient. The simulated zonal SST gradient, however, is generally too strong compared to the observations. This is a result of the cold bias mentioned in the model validation Chapter 2. Least squares linear regression indicates that the period is decreased by 0.48 years per $1.0°C$ increase in the zonal gradient. A stronger coupling generally leads to a reduced zonal SST gradient.

A linear relationship also exists between the period and the thermocline intensity (Fig. 3.2, lower panel), where periods are decreasing with weakening thermocline intensity. A stronger coupling increases the distance between the 16-22°C isotherm depths, however, the thermocline intensity is generally too low compared to the Levitus and Boyer (1994) observations. As mentioned in the model Chapter 2, capturing the correct thermocline intensity is a common problem of GCMs.

In the following the ENSO amplitudes of the different experimental setups are discussed. The Nino-3 amplitudes of the coupled experiments are generally slightly too strong compared to observations. Relatively low amplitudes (0.99-1.2°C) are found for low couplings of Cp=0.7 and Cp=0.8 and mean wind stresses of 0.6, 0.8 and 1.6 times OMIP. Generally, as a function of the mean wind stress, the amplitude increases between 0.6 and 1.2 (Fig. 3.3, upper panel). Between 1.2 and 1.6 times OMIP the amplitude is decreasing. Furthermore, the amplitude is increasing with increasing coupling coefficient, where a coupling of 1.2 generally leads to a standard deviation above 1.7°C. The amplitude as a function of the mean thermocline depth shows similar structures, where an amplitude increase for increasing mean thermocline depth is noted (Fig. 3.3, lower panel). The amplitude is decreasing if the zonally averaged thermocline depth is deeper than 120 meters.

The relationship between the simulated zonal SST gradient and the Nino-3 amplitude is non-linear, where an increase of the zonal SST gradient may generally lead to increasing amplitudes (Fig. 3.4, upper panel). The simulated zonal SST gradient is generally too strong compared to observations. An increasing coupling leads to weaker zonal SST gradients.
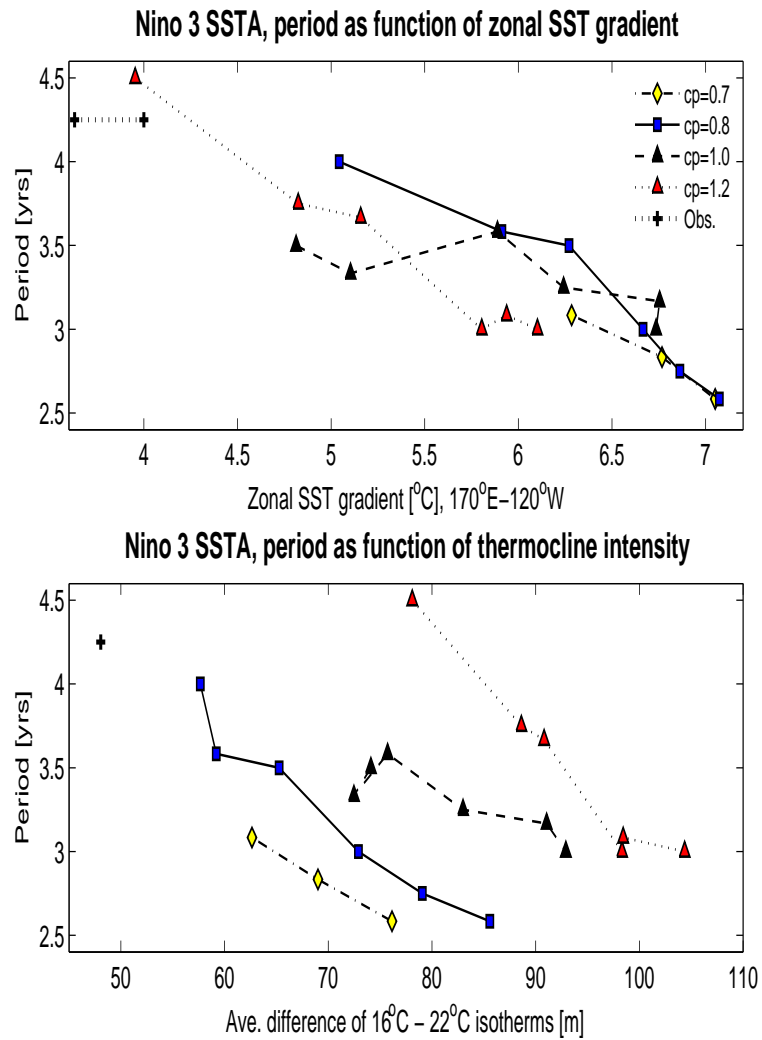
**Fig. 3.2:** *Upper panel: Nino-3 period for the coupled model experiments as a function of the zonal SST gradient along the equator. Lower panel: period as a function of thermocline intensity. The model simulations with the same coupling coefficient are connected by lines. The upper and lower bounds for observations are calculated as described in Section 3.2.*

A weaker thermocline intensity is associated with a stronger amplitude (Fig. 3.4, lower panel). A least squares linear regression calculates a 0.016°C amplitude increase, if the 16-22°C isotherm distance is increased by 1 meter, with a correlation of 0.83.
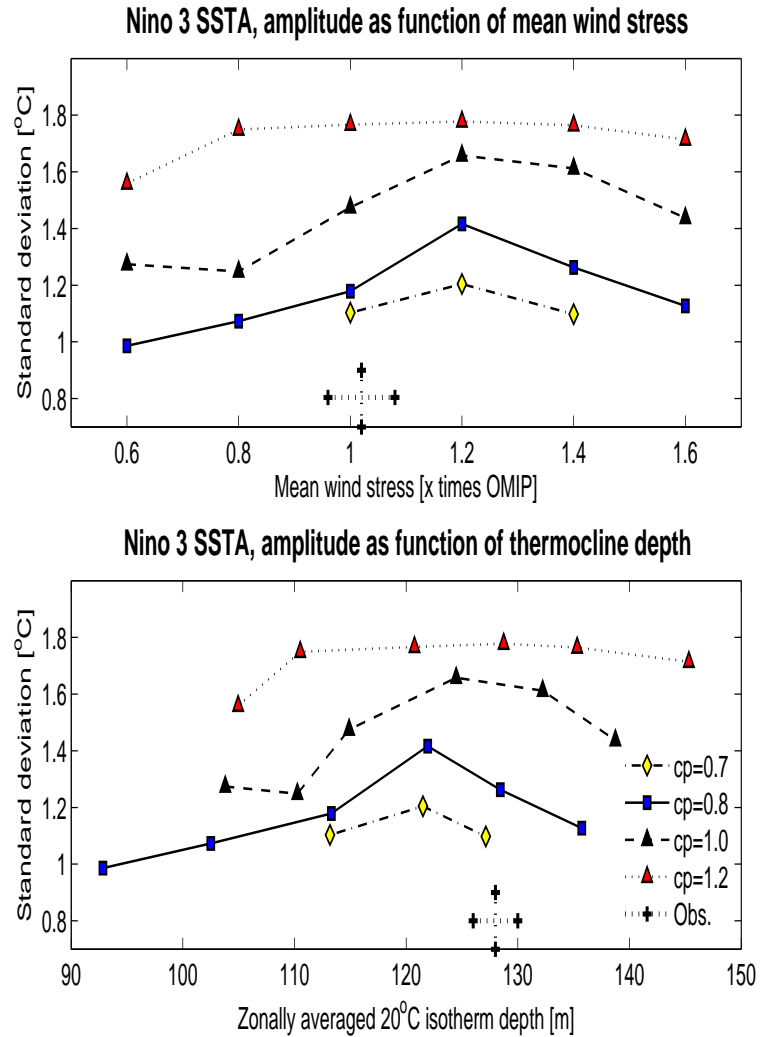
**Fig. 3.3:** *Upper panel: Nino-3 standard deviation for the coupled model experiments as function of the mean wind stress. Lower panel: Nino-3 standard deviation as a function of the mean thermocline depth. The coupled model simulations with the same coupling coefficient are connected by lines. Ranges for observations are estimated as described in Section 3.2.*
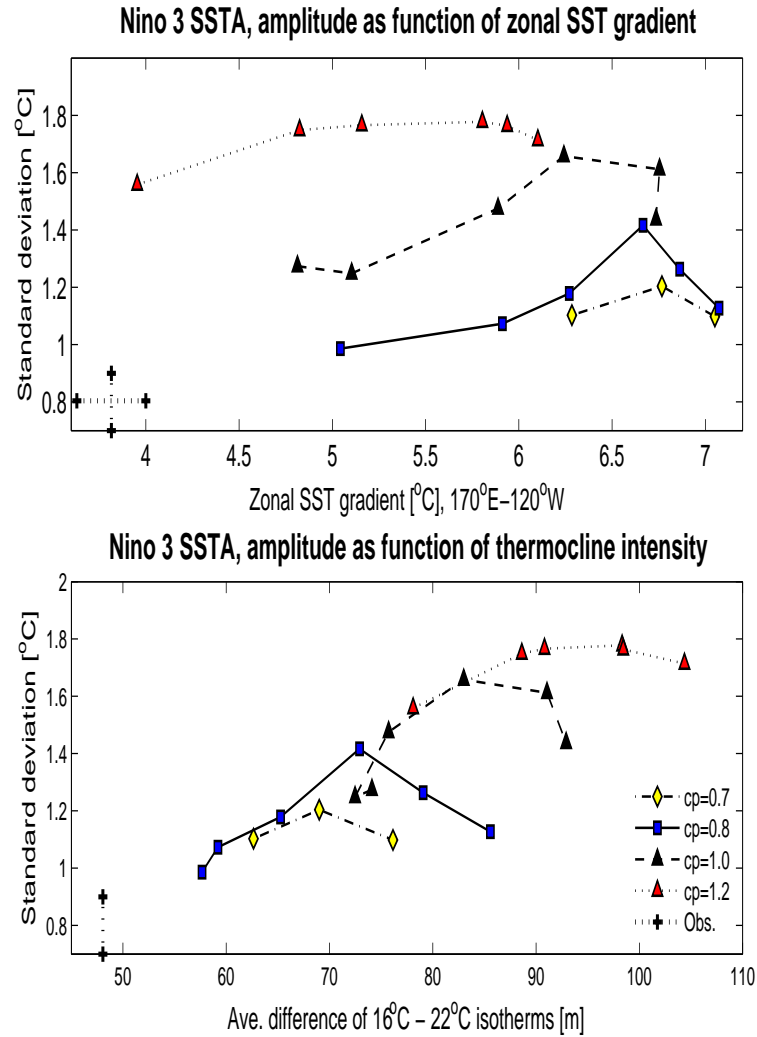
**Fig. 3.4:** *Upper panel: Nino-3 standard deviations for the coupled model experiments as function of the zonal SST gradient. Lower panel: amplitude as a function of the thermocline intensity. The model simulations with the same coupling coefficient are connected by lines. Ranges for observations are estimated as described in Section 3.2.*
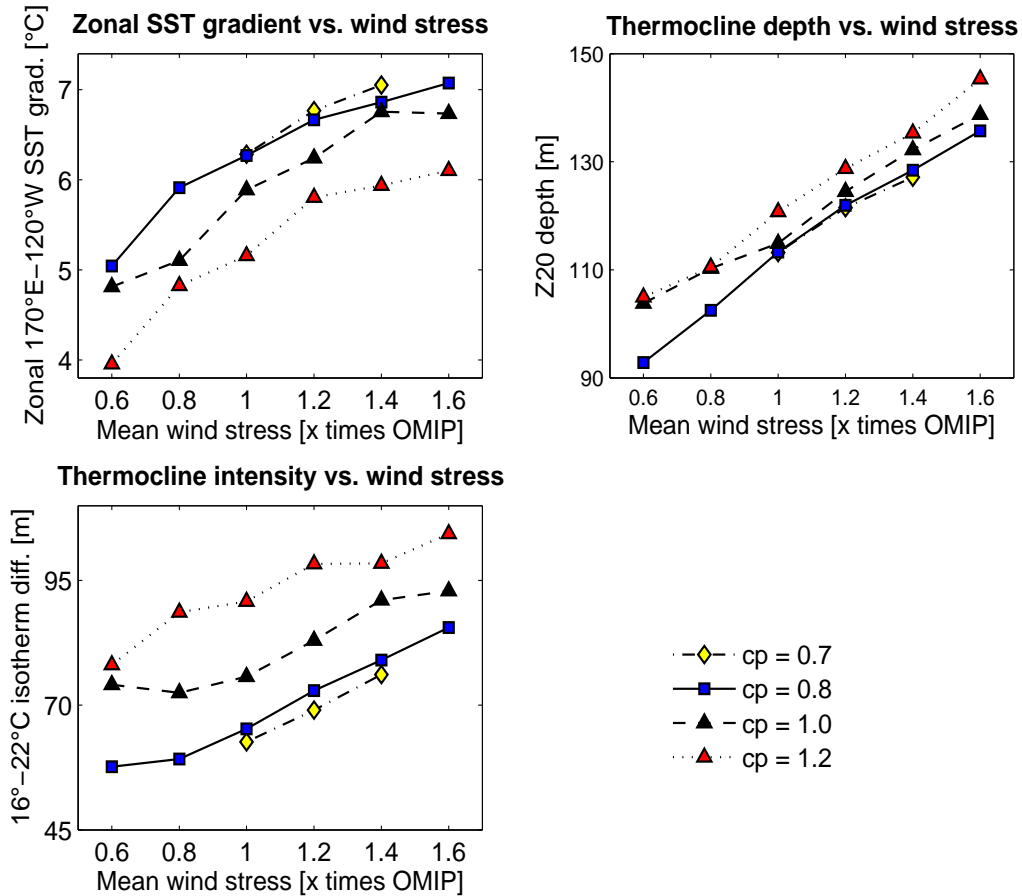
**Fig. 3.5:** *Relationships between the mean quantities for the coupled experiments. Upper left: zonal SST gradient versus mean wind stress. Upper right: mean thermocline depth versus mean wind stress. Lower left: thermocline intensity versus mean wind stress. The model simulations with the same coupling coefficient are connected by lines.*

Figure 3.5 summarizes the relationships among the mean background quantities. It can be seen that the mean thermocline depth is nearly a linear function of the mean wind stress, and depends only weakly on coupling coefficient Cp (Fig. 3.5, upper right). The least squares linear trend estimate is a 3.9 meter deepening of the mean thermocline per 10 percent wind stress increase, with a correlation of 0.96. The zonal SST gradient increases if the mean wind stress is increased (Fig. 3.5, upper left). On average the gradient increases by 0.2°C if the mean wind stress is increased by 10 percent, with a correlation of 0.82. The thermocline intensity gets weaker when the mean wind stress is increased (Fig. 3.5, lower).

Figure 3.6 presents the results of the HCM experiments as a function of the coupling coefficient Cp. Model simulations with the same mean wind stress are connected. The period shows a non-linear behavior as function

of the coupling (Fig. 3.6 a). On average, the Nino-3 standard deviation is increasing if the coupling coefficient Cp is increased (Fig. 3.6 b). Furthermore, the thermocline intensity (z20 intensity) is linearly related to the coupling coefficient, where an increase of the coupling Cp by 10 percent leads to an increase of the 16-22°C isotherm distance of 5.2 meters on average, with a correlation of 0.74 (Fig. 3.6 d). A weak linear correlation of 0.19 is found between the thermocline depth (z20 depth) and the coupling (Fig. 3.6 c). The zonal SST gradient is decreasing at a rate of 0.26°C per 10 percent increase of coupling, with a correlation of 0.58 (Fig. 3.6 e). The least squares linear regression coefficients are also summarized in Table 6.1.

In the HCM, the ocean-to-atmosphere coupling is prescribed by the coupling coefficient Cp. It is difficult to compare the ocean-to-atmosphere coupling and the associated coupling coefficient to other modelling studies and to observations. A method to make the coupling more accessible is to calculate the first EOF of the anomalous SST and wind stress, and the regression coefficient of the first principal components for every experiment. (The calculation is similar to the calculation of $C_{1,1}$ in Section 2.3 of Chapter 2). Thus, the EOF regression coefficient $C_{1,1}$ is used as a measure of the ocean-to-atmosphere coupling, which allows to compare the results of the HCM experiments to other model experiments and to observations. A scatter plot of the coupling coefficients and the EOF regression coefficients $C_{1,1}$, calculated for the coupled model experiments, is shown in Fig. 3.7 (upper left). A linear behavior can be seen, where an increase of Cp leads to an increase of $C_{1,1}$. The correlation of the linear fit is 0.83, where an increase of Cp by 10 percent leads to an increase of $C_{1,1}$ by 0.003 Pa/°C. Furthermore, the values of period and amplitude of the Nino-3 time series are plotted versus $C_{1,1}$. Consistent with previous results the period is rather poorly related to $C_{1,1}$ (Fig. 3.7, upper right), where a higher $C_{1,1}$ leads to higher periods. A good linear relation exists between amplitude and $C_{1,1}$ (Fig. 3.7, upper lower), where a higher $C_{1,1}$ leads to higher amplitudes.
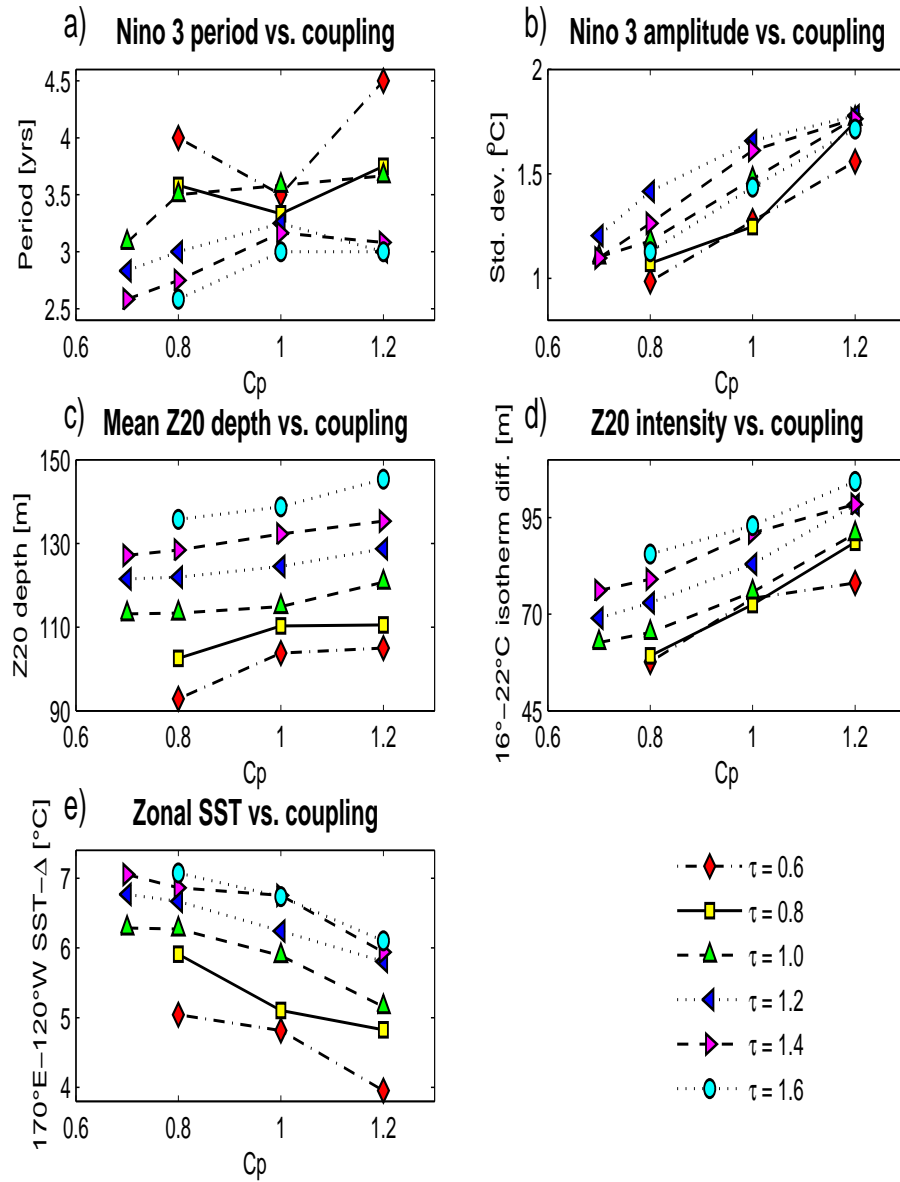
**Fig. 3.6:** *Results of the coupled model experiments as function of the coupling coefficient Cp. The model simulations with identical mean wind stress forcing are connected by lines. Displayed in the panels a)-e) are: period of the Nino-3 SSTA versus Cp (a), Nino-3 SSTA standard deviation vs. Cp (b), mean thermocline depth (z20) vs. Cp (c), thermocline intensity vs. Cp (d) and zonal SST gradient vs. Cp (e).*
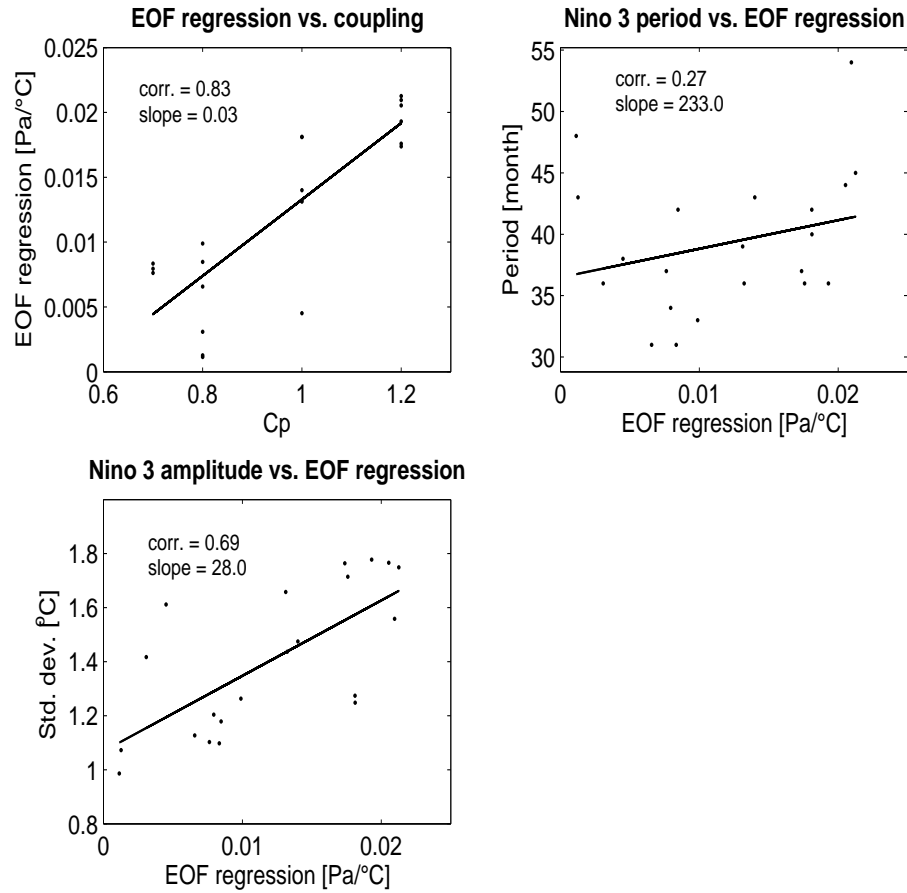
**Fig. 3.7:** *Upper left: Scatter plots of the EOF regression coefficient $C_{1,1}$ versus the associated coupling coefficient $Cp$, calculated for the coupled model experiments. Upper right: Nino-3 period versus $C_{1,1}$. Lower panel: Nino-3 standard deviations versus $C_{1,1}$. Each plot contains a linear fit (solid line) and the associated slopes and correlations (corr.).*

## 3.4   Comparison with other model results

In this section, the results of the HCM runs are compared to model studies using intermediate complexity models (ICMs) and to studies with fully coupled GCMs. Although all models vary profoundly in their physical and numerical setup, all models are generally designed to simulate a realistic ENSO variability. It should be noted however, that the ICM models used in this section were actually designed for the purpose of simulating ENSO with a changed climatic background state, while the purpose of the AOGCM studies was different.

### 3.4.1   Comparison to ICM studies

Fedorov and Philander (2000, 2001) used an ICM based on a shallow water model with an embedded mixed layer. The model is similar to the models by Zebiak and Cane (1987) and Jin and Neelin (1993). Their ICM allowed to simulate ENSO with prescribed mean wind stress, mean thermocline depth and thermocline intensity. Thus, they were able to survey a large volume of the parameter space. Their results for the dependence of period on mean wind stress and mean thermocline depth is shown in Fig. 3.8 (upper left panel). The plot corresponds to Figure 4 shown in the study by Fedorov and Philander (2001)[1]. Here, the colours denote the period of the Nino-3 anomalies, where blue colours denote relatively low periods (2-4 years), while yellow to red denotes relatively high periods (4-8 years).

It is now possible to compare the results of this study by adapting the parameters appropriately. Fig. 3.8 (upper right panel) shows the values of thermocline depth and mean wind stress for the HCM runs. The synthesis of the two upper panels is shown in Fig. 3.8 (middle panel). From this, periods can be estimated, according to the ICM. For instance, with a mean wind stress of 1.0 times OMIP and coupling coefficient Cp=1.0 the HCM has a mean thermocline depth of 114.9 meters (see Table 6.3, in Appendix 6.2). With these values of mean wind stress and mean thermocline depth, the associated ENSO period of 3.5 years is estimated from Fig. 3.8 (middle panel).

It is noted, that in the ICM, the equatorial mean stress is idealized as an analytical function, defined for the area between 130°E-85°W and 5°N-5°S. Furthermore, in the standard case the mean stress used in the ICM, averaged for the defined area, is -0.0294 Pa. The OMIP mean wind stress averaged for the defined area is -0.0257 Pa. Therefore, the standard mean wind stress in the ICM is 1.14 times stronger than in the HCM.

---

[1] Permission by the American Meteorological Society to use the figures is kindly acknowleged.
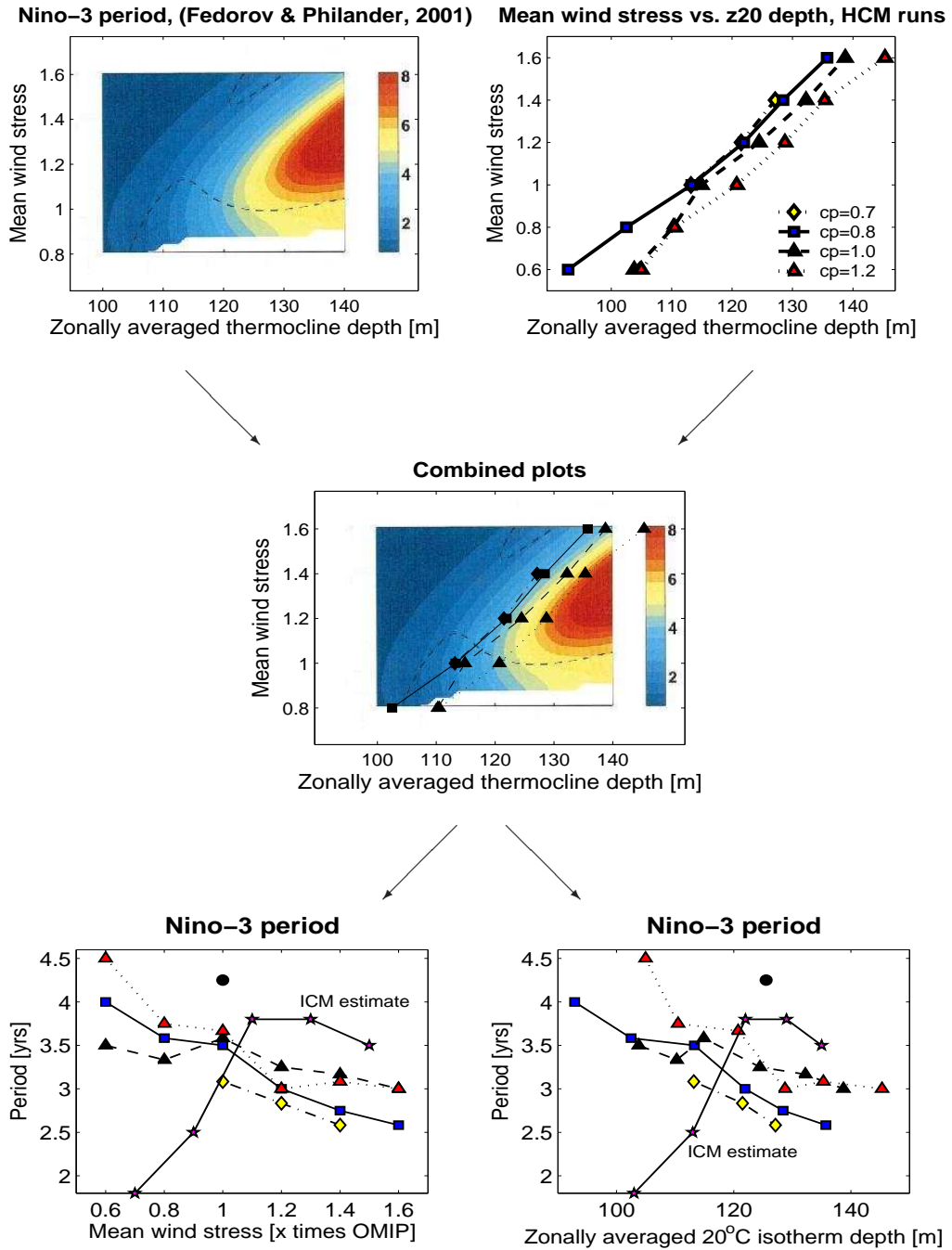
**Fig. 3.8:** *Comparison of the HCM and ICM results. Upper left: ENSO period as function of the parameters mean wind stress and zonally averaged thermocline depth from the ICM study by Fedorov and Philander (2001). The colours represent the periods of the Nino-3 time series (in years). Upper right: the mean wind stress versus thermocline depth from the HCM experiments. Middle panel: synthesis of the upper panels. Lower panels: The estimated periods from the ICM are inserted in the panels of Figure 3.1*

As an example, the coupled HCM experiments with Cp=1.0 are taken and the periods for the mean wind stress of 0.8-1.6 times OMIP are estimated from the middle panel of Fig. 3.8. The upper panel of Fig. 3.1 is redrawn in Fig. 3.8 (lower left panel) together with the ICM estimates. As can be seen, the period estimates from the ICM show a non-linear behavior, different to the curves of the HCM experiments. In the same manner, the lower panel of Figure 3.1 is redrawn in Fig. 3.8 (lower right panel) together with the ICM estimates, but as function of the mean thermocline depth. The non-linear behavior of the ICM estimates disagree with the HCM results.

In further experiments, Fedorov and Philander (2001) analyzed the relationships between ENSO period, the mean wind stress and the thermocline intensity. In their ICM, the thermocline intensity is prescribed as the temperature difference in °C over a 50 meter depth variation across the thermocline. The behavior of the Nino-3 period with respect to the mean wind stress and the thermocline intensity according to Fedorov and Philander (2001) is displayed in Fig. 3.9 (upper panel). The colours denote the modelled ENSO period. As can be seen, variations in the thermocline intensity have a large impact on the ENSO period. For the coupled HCM experiments the thermocline intensities are recalculated in similar manner to the ICM values, and the mean wind stress and thermocline relationship are shown in Fig. 3.9 (middle panel). The HCM results are inserted and displayed in 3.9 (lower panel). It can be seen, that the HCM estimates are mostly located outside of the abscissa. Nonetheless, it can be seen that the variations of the thermocline intensities in the HCM experiments lead to large variations of the estimated ENSO periods.

It is concluded that the parameterization of the thermocline intensities is responsible for the disagreement of the modelled ENSO periods as simulated among the models. In the ICM the thermocline intensity is a prescribed parameter, while in the HCM the thermocline structure is a modelled physical value. Thus, the differences in the simulated ENSO periods are partly explained by the different complexity of the models. The differences in the simulated ENSO variability highlight the difficulties of comparisons among simple models, fully developed GCMs and observations.
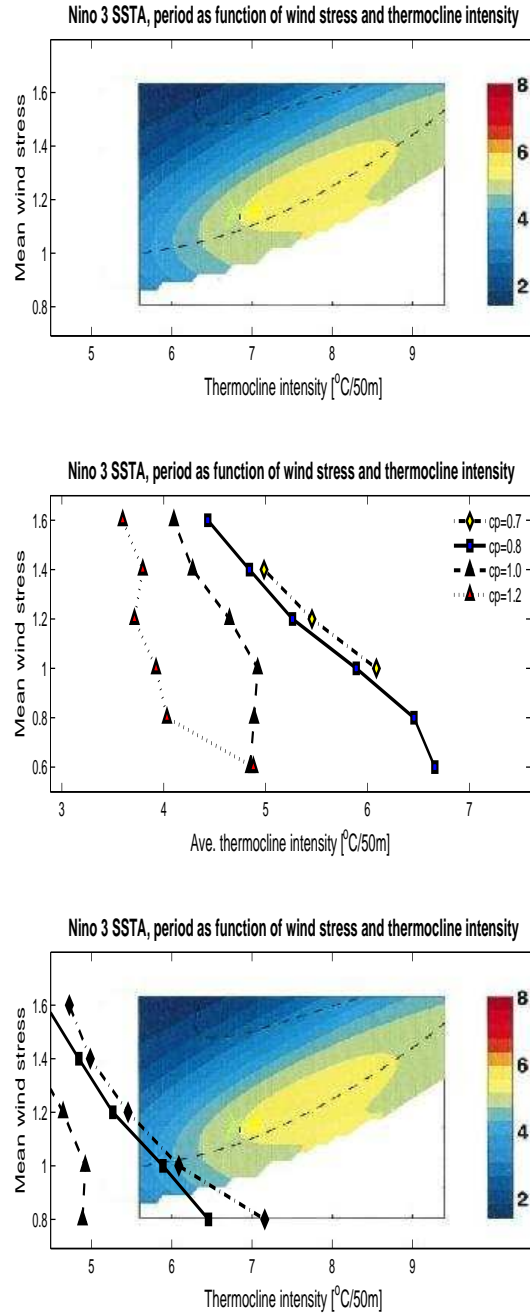
**Fig. 3.9:** *Comparison of ICM with HCM results. Upper panel: the period as function of the mean wind stress and the thermocline intensity, measured as the average temperature variation across 50 meters of the thermocline (after Fedorov and Philander (2001)). The colours represent the periods of the Nino-3 time series (in years). Middle panel: The mean wind stress and thermocline intensities from the HCM experiments. The thermocline intensities are calculated similar to the ICM values. Lower panel: synthesis of the upper and middle panel.*

## 3.4.2   Comparison to AOGCM studies

In this section, data from the El Niño simulation intercomparison study (ENSIP) by Latif *et al.* (2001) are used to compare the results of the previous section to AOGCM results. Intercomparison studies of coupled atmosphere and ocean general circulation models provide assessment of whether these models are able to capture the principal structures of ocean-atmosphere dynamics. The ENSIP study assessed the performance of 24 state-of-the-art AOGCMs, with respect to the simulation of the tropical Pacific climatology and interannual variability. For this study 11 of the original 24 AOGCM simulations were chosen which fulfilled criteria on the simulated ENSO period (2-7 years period) and amplitude (0.45-2.0°C standard deviation), of the Nino-3 SSTA time series. The chosen models are listed in Figures 3.10 and 3.11 (see Latif *et al.* (2001) for further details on the models). For these models, the mean wind stress and zonal SST gradients were calculated as described in Section 3.2. The calculated values can be found in Table 6.4 in Appendix 6.2.

The simulated Nino-3 amplitudes and mean wind stresses for the AOGCM experiments are shown in Fig. 3.10 (upper panel), together with coupled HCM experiments. The AOGCM results show a large spread among the experiments, but generally the Nino-3 amplitude is weaker in the AOGCM simulations than in the HCM experiments. As a function of the zonal SST gradient, the estimated values from the AOGCMs show a weaker gradient in comparison to the HCM results ( Fig. 3.10, lower panel). The AOGCM amplitude-to-zonal-SST-gradient relationship is non-linear.

In Fig. 3.11 (lower panel) the AOGCM results for the ENSO period are illustrated as function of the mean wind stress, together with the results of the HCM simulations. A large spread of the period among the AOGCM experiments is visible, where some models show a relatively low period near or below 2.5 years. The apparent linear relationships found in the HCM experiments could not be reproduced for the AOGCM results. As a function of the zonal SST gradient, the ENSO period for the AOGCM simulations is distributed non-linearly.

In summary, the AOGCM results do not indicate relationships similar to the HCM results. Reasons for this absence may lie in the different setups and parameters used for the various models. A reasonable comparison of the variability in terms of the mean climatologies is only to a very limited extent feasible. Furthermore, as noted by Latif *et al.* (2001), at the time of the study many model still had difficulties in simulating a reasonable climatic background state and tropical Pacific variability.
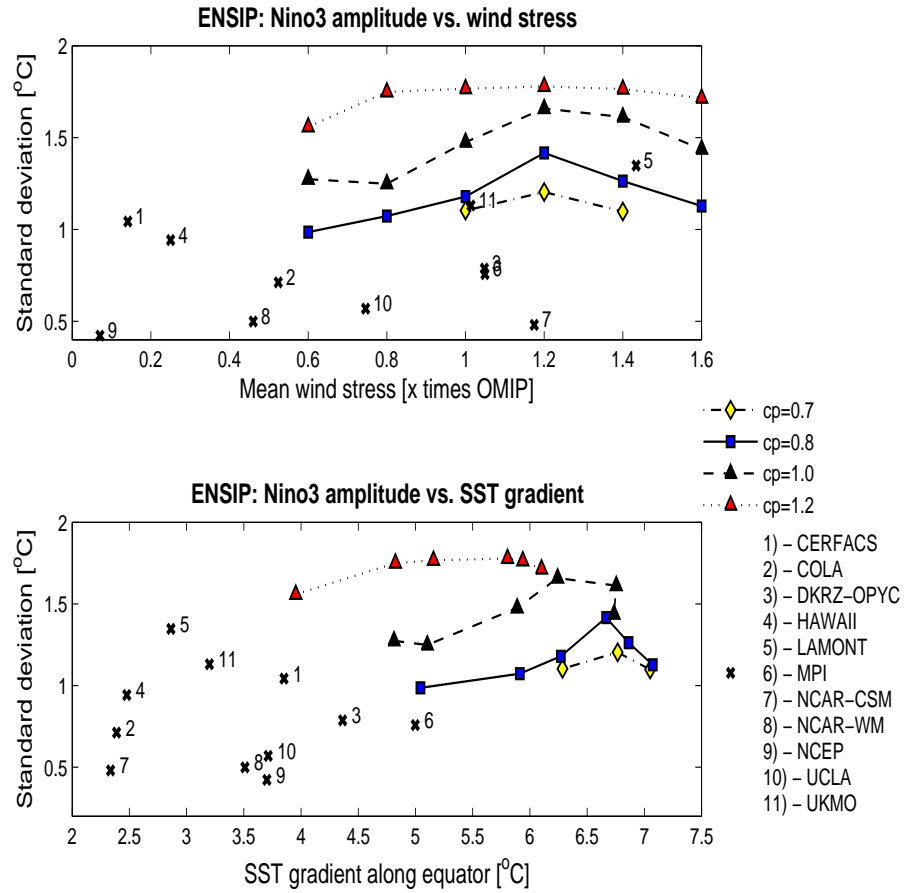
**Fig. 3.10:** *Comparison to AOGCM studies taken from the ENSIP study by Latif* et al. *(2001). Upper panel: standard deviations of the Nino-3 anomalies of the models from ENSIP together with the HCM results drawn as a function of the mean wind stress. Lower panel: standard deviations as a function of the zonal SST gradient.*
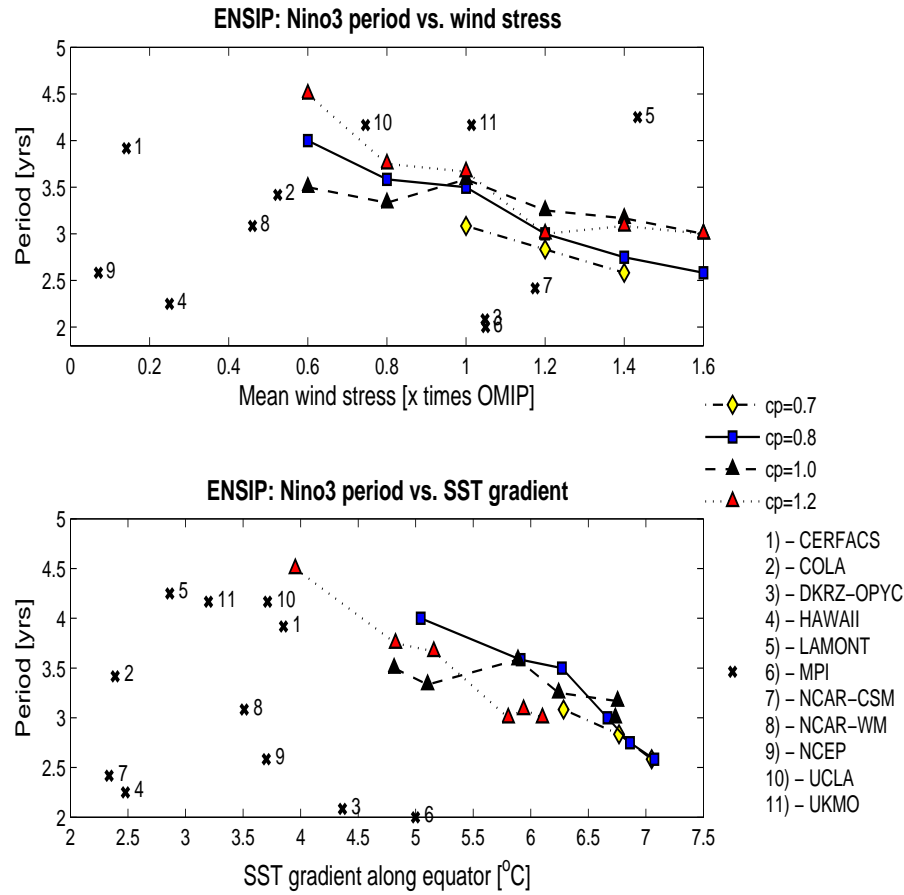
**Fig. 3.11:** *Comparison to AOGCM studies taken from the ENSIP study by Latif et al. (2001). Upper panel: periods of the Nino-3 anomalies of the models from ENSIP together with the HCM results drawn as a function of the mean wind stress. Lower panel: periods as a function of the zonal SST gradient.*

## 3.5 Summary and Conclusions

Several simulations with a hybrid coupled model were performed to get an overview of possible changes in the variability and mean state of the tropical Pacific ocean-atmosphere system due to changes in the mean wind field. Two parameters, the strength of the ocean-to-atmosphere coupling and the magnitude of the zonal mean wind stress, are varied within realistic boundaries. The ENSO amplitude, period and the oceans thermal structure were investigated. Results showed that ENSO amplitude is mainly a function of the ocean-to-atmosphere coupling and increases linearly with increasing coupling strength. Furthermore, increased coupling leads to weaker thermocline intensities and to higher EOF regression coefficients, which is calculated as a measure of the anomalous ocean-to-atmosphere coupling. The ENSO period is mainly affected by the increase in mean wind stress and the associated increase in zonal SST gradient and thermocline depth. The least squares linear regression coefficients for the different quantities are listed in Table 3.2.

|           | SST-$\Delta$ | Z20    | Z20 int. | Cp-EOF  | Period  | Stdv.   |
|-----------|--------------|--------|----------|---------|---------|---------|
| $\tau$    | **2.12**     | **39.17** | 23.92  | -0.0027 | **-14.1** | 0.1641  |
| Cp        | -2.63        | 13.92  | **52.37** | **0.0295** | 12.03   | **1.264** |
| SST-$\Delta$ | 1         | 10.26  | 1.17     | -0.0045 | **-5.80** | -0.079  |
| Z20       | 0.041        | 1      | **0.76** | 0.000060 | -0.31   | 0.008   |
| Z20 int.  | 0.0049       | **0.79** | 1      | 0.000299 | -0.11   | **0.016** |
| Cp-EOF    | -73.98       | 248.01 | 1177.92  | 1       | 232.91  | 27.91   |

**Tab. 3.2:** *Linear regression coefficients for the coupled experiments. The left column depicts the independent variables and the upper row depicts the dependent variables. $\tau$ denotes the mean wind stress (times OMIP) and Cp is the dimensionless coupling coefficient. SST-$\Delta$ denotes the zonal SST gradient (in $^\circ C$), Z20 is the mean thermocline depth (in meters), Z20 int. is the thermocline intensity (in meters), Cp-EOF is the EOF regression coefficient (in Pa/$^\circ C$), period is the Nino-3 SSTA period (in month), Stdv. is the Nino-3 SSTA standard deviation (in $^\circ C$). Values with absolute correlations higher than 0.7 are depicted bold. The associated correlations can be found in Appendix 6.2 (Table 6.3).*

On average, a 10% increase of the mean wind stress leads to an increase of the zonal SST gradient by 0.212°C, deepens the mean thermocline by 3.9 meters and decreases the ENSO period by 1.4 month. Furthermore, 10% increase of the coupling strength increases the 16-22°C isotherm distance by 5.2 meters and increases the Nino-3 standard deviation by 0.13°C. The sensitivity of the amplitude to the coupling strength is in agreement with theoretical studies, which favor an increase in amplitude when the cou-

pling is increased (e.g. Zebiak and Cane (1987); Jin and Neelin (1993); Jin (1997)).

The connection between the mean wind stress and period of ENSO is less clear. The increased trade winds may lead to a faster build-up of heat in the eastern tropical Pacific and thus to increased ENSO frequency (period decrease), according to the recharge-discharge paradigm (described in Section 2.5.1). Furthermore, the thermocline in the east is lifted and thus, the system is more sensitive, which leads to faster transition and lower ENSO periods. Thus, the period should decrease with increasing EOF regression coefficient $C_{1,1}$, which serves as a measure of the ocean-to-atmosphere sensitivity. However, a scatter plot shows an increase of period with increasing EOF regression coefficient, $C_{1,1}$, which is a caveat on the given explanation.

A comparison to recent studies with ICMs and AOGCMs draws a somewhat elusive picture. An ICM study by Fedorov and Philander (2001), which investigates the period of ENSO as a function of the mean background state, at first view contradicts the findings of this study. In their model, an increase in wind stress and thermocline intensity leads to a non-linear change in period, which differs significant from the HCM results. However, in their model the thermocline intensity is a prescribed parameter. In further studies, Fedorov and Philander (2001) also showed how dramatic the vertical temperature structure affects the ENSO frequency. In the HCM the thermocline intensity is a modelled quantity and thus the different behavior in frequency may be explained. It might be assumed that the HCM results might explain better the AOGCM results and observations. However, the comparison to AOGCM results from the ENSIP study (Latif *et al.* (2001)) does not exhibit relationships similar to the HCM results. Reasons for this may lie in the very different physics among the AOGCMs. As pointed out by the authors, at the time of the ENSIP study many AOGCMs had difficulties in simulating a reasonable tropical Pacific mean state and ENSO variability.

# 4. ENSO SENSITIVITY TO WIND STRESS CORRECTED FOR SURFACE MOTIONS

**Abstract**

The common bulk formula for the calculation of wind stress over the open oceans usually does not take the sea surface motions into account. This is a reasonable approximation over most of the oceans, since surface current velocities are usually relatively slow compared to surface winds. Thereby, these wind stress products can reasonably be applied to force ocean general circulation models (GCMs). However, in the tropical Pacific, where wind speeds are relatively low, while current velocities can exceed 1.0 m/s, this approximation may lead to biased results in the simulation of the long term climatology and the interannual variability. Using a hybrid coupled GCM (HCM) the impact of wind stress corrected for surface currents on tropical dynamics is examined. Furthermore, different parameterizations of the drag, $C_d$, which is modelled as a function of the wind speed, are tested. The results show that a different formulation can lead to an improved representation of the mean sea surface temperature (SST). Furthermore, simulations of the El Niño/Southern Oscillation (ENSO) phenomenon show weaker variability and changes in the periods. In some cases the ENSO mode changes from an unstable sustained to a stable damped mode. The results indicate that moderate variations in the parameterizations can affect ENSO simulations strongly. In coupled GCM studies of the tropics, a careful consideration of correcting the wind stress for surface motions should be taken into account.

## 4.1   Introduction

Coupled atmosphere-ocean general circulation models (AOGCMs) of the tropical system have undergone a continuous development in the recent decades. Despite these advances, problems in simulating ENSO variability have stayed remarkably rigid. Intercomparison studies (Latif *et al.* (2001); AchutaRao and Sperber (2002); Davey *et al.* (2002)) with a number of state-of-the-art AOGCMs came to the conclusion that many models still have

problems in simulating a correct background climatology, especially in the sensitive equatorial Pacific, and only a few models simulate the interannual variability reasonably well. The studies concluded that substantial model improvements are needed, especially with respect to the simulated ENSO variability and the mean ocean thermal structure.

In this chapter the impact of the representation of the momentum flux at the ocean to atmosphere boundary on the simulations of tropical Pacific climate is investigated. A common practice for the parameterization of wind stress at the ocean-to-atmosphere boundary is the following empirical formula (Gill (1983); Peixoto and Oort (1992)):

$$\vec{\tau} = C_d \, \rho \, |\vec{u}| \, \vec{u} \tag{4.1}$$

In this equation $\vec{\tau}$ is the wind stress vector, $C_d$ is a dimensionless drag coefficient, $\rho$ is the air density at sea level, and $\vec{u}$ is the vector of zonal and meridional wind speed at a given reference level. The wind speed is usually given with respect to a fixed reference surface under neutral conditions (Stewart (2002)). This is a reasonable approximation for the open ocean, where surface current speeds are usually 1 to 2 magnitudes lower than the wind speeds. Close to the Pacific equator this assumption is not valid anymore. Here, the prevailing trade wind speeds are low, around 5-9 m/s on average, while surface current speeds can exceed 1.0 m/s (Halpern (1988); Kelly *et al.* (2001)).

A first order correction would be to correct the wind speed for the ocean current speed i.e.

$$\vec{\tau}^* = C_d \, \rho \, |\vec{u}^*| \, \vec{u}^* \tag{4.2}$$

with

$$\vec{u}^* = \vec{u} - \vec{u}_c \tag{4.3}$$

where $\vec{u}_c$ denotes the vector of surface current motions. In the following, this parameterization is referred to as shear correction. An early model study of the equatorial Atlantic by Pacanowski (1987) showed that this leads to an improved representation of the equatorial Atlantic SST, which increased by 1°C due to reduced easterly wind stress. To the best of the author's knowledge, these first studies were largely ignored and the use of these corrections was not widespread. A reason for this might be the relatively poor quality of equatorial wind stress products before the 1990s (Stockdale *et al.* (1998)). McPhaden *et al.* (1998) noted that a robust estimate of monthly mean wind speeds with an accuracy of 0.5-1.0 m/s requires daily measurements of wind speeds, which where not regularly sampled prior
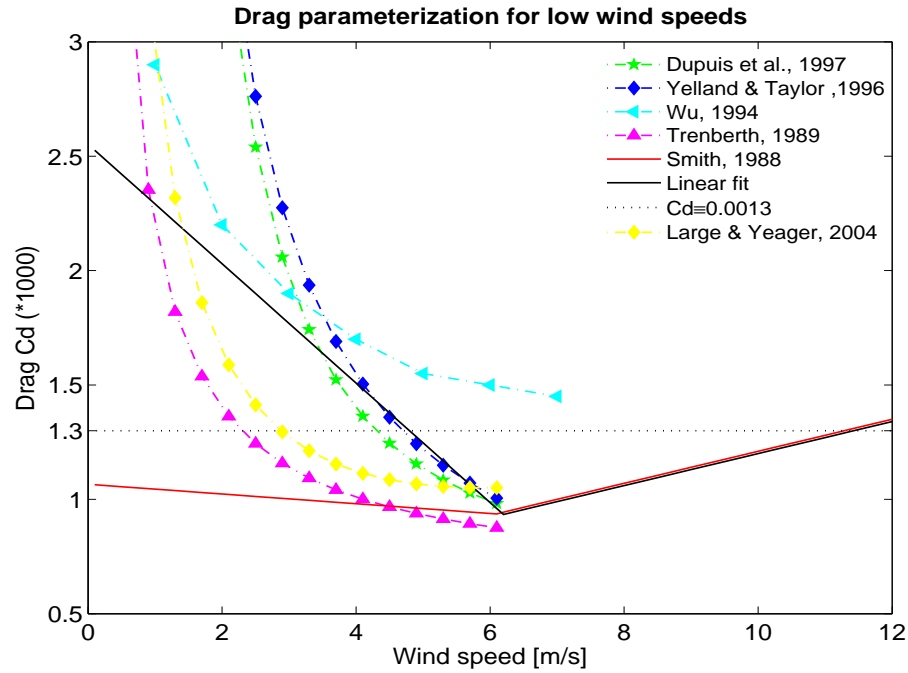
**Fig. 4.1:** *Drag parameterization for low wind speeds according to various studies. Solid lines indicate the linear parameterizations used in this study.*

to and during the early stages of the Tropical Oceans-Global Atmosphere (TOGA) program.

Recently, shear corrections of surface motions have been used in AOGCM studies (e.g. Luo *et al.* (2005); Jungclaus *et al.* (2006)). They showed improvements of the equatorial SST structure and ENSO variability. Some of the results by Jungclaus *et al.* (2006) will be used for comparison in the later sections.

Another critical point in determining wind stress is the value of the drag coefficient $C_d$. It was a common practice for forced OGCMs to set the drag coefficient to a constant value, usually about 0.0013. However, measurements of the drag coefficient over open oceans suggest that $C_d$ should be formulated as a function of the wind speed. An approximation of the measurements is the following parameterization by Smith (1980, 1988):

$$1000 C_d = \begin{cases} \sim 1.0 & if \quad u \leq 6.0 m/s \\ 0.07u + 0.5 & if \quad u > 6.0 m/s \end{cases} \qquad (4.4)$$

where $u = |\vec{u}|$ denotes the absolute wind speed. The drag is nearly constant for a wind speed below 6.0 m/s and increases linearly above 6.0 m/s. The graph of the function is sketched as a solid red line in Fig. 4.1.

Other studies (e.g. Trenberth *et al.* (1989); Wu (1994); Yelland and Taylor (1996); Yelland *et al.* (1998); Dupuis *et al.* (1997); Large and Pond (2004)) show a different behavior for low wind speeds (Fig. 4.1). The studies show similar increase for wind speeds higher than 6.0 m/s. For simplicity, the parameterization for wind speeds higher than 6.0 m/s is approximated by the linear function $1000C_d = 0.07u + 0.5$, adopted from Yelland *et al.* (1998). In contrast to the observations by Smith, however, the parameterizations show an increase for wind speeds below 6.0 m/s. It can be seen, that there are large uncertainties in how strongly wind stress increases with wind speeds below 6 m/s. This results from the general difficulties in measuring momentum fluxes at low wind.

For the purpose of this study, a linear approximation of the increasing curves (sketched in Fig. 4.1) for values below 6.0 m/s is estimated by the following formula:

$$1000C_d = \begin{cases} -0.261u + 2.552 & if \quad u \leq 6.0m/s \\ 0.07u + 0.5 & if \quad u > 6.0m/s \end{cases} \tag{4.5}$$

The linear approximation is sketched as a solid black line in Fig. 4.1.

In this study the effect of different parameterizations for wind stress shall be investigated. For this purpose a number of HCM sensitivity runs in uncoupled and coupled mode are performed, with and without shear correction (equations 4.2 and 4.3) and with parameterizations after equations 4.4 and 4.5.

The analysis focuses on the climatological SST, the mean wind stress and the ocean thermal structure. These factors are of main importance for ENSO and are also relatively easy to access. Furthermore, the El Niño simulations are investigated with respect to the ENSO amplitudes and periods, as well as the spatial structure of the tropical variability.

## 4.2 Uncoupled simulations

### 4.2.1 Experimental setup

In the uncoupled case the model is forced with the OMIP climatological fluxes as described in Chapter 2. The wind stress anomalies from the FSU pseudo wind stress product (Stricherz *et al.* (1997)) are added to the climatological forcing, where a drag of $C_d = 0.0013$ and $\rho = 1.026kg/m^3$ is used to calculate the wind stress. To obtain the wind speed, which is necessary for the calculation of the shear correction and the drag functions, the vector of wind speed is first derived from equation 4.1, that is:

$$\vec{u} = \sqrt{\frac{|\vec{\tau}|}{C_d \, \rho}} \; \vec{\tau_e} \tag{4.6}$$

where $\vec{\tau_e}$ is the unit vector $\vec{\tau}/|\vec{\tau}|$. With $\vec{u}$ surface corrections and drag can be calculated according to the experimental setting.

ENSO is simulated with six different surface stress parameterizations given in Table 4.1.

| Experim. | Drag param. | Shear | Comment |
|----------|-------------|-------|---------|
| CTRL | $C_d = 0.0013$ | no | standard run |
| SHEAR | $C_d = 0.0013$ | yes | shear correction only |
| DRAG | Definition 4.5 | no | drag correction only |
| BOTH | Definition 4.5 | yes | both corrections |
| DRAG_S | Definition 4.4 | no | drag corr. only (Smith (1988)) |
| BOTH_S | Definition 4.4 | yes | both corr. (Smith (1988)) |

**Tab. 4.1:** *Parameterizations for the different experiments in uncoupled mode.*

In the standard run (CTRL) no surface correction is applied, and the drag coefficient is set to a constant value of $C_d = 0.0013$. In the SHEAR experiment the surface currents are used to correct the wind speed by applying equation 4.2. In the drag adaption case (DRAG), the only modification with respect to the control simulation is to calculate the drag coefficient according to equation 4.5. In another experiment (BOTH) the surface wind speed is corrected toward the surface motion, and the drag coefficient is calculated as a function of the corrected wind speed. Furthermore, in the DRAG_S and BOTH_S experiments, the drag is calculated as in DRAG and BOTH, respectively, but the drag coefficient is calculated via equation 4.4.

## 4.2.2 Results

The changes in mean SST due to the different parameterizations are shown in Fig. 4.2. The SST biases are shown with respect to Levitus and Boyer (1994) observations. In panel (a) the mean wind stress vectors of the CTRL experiment are superimposed. In panels (b-f) the difference vectors of the modelled wind stress with respect to the CTRL experiment are superimposed. In the standard run (CTRL) the modelled SSTs show a temperature bias of 2°C in the eastern equatorial region (Fig. 4.2 a). The SST bias is slightly reduced in the SHEAR experiment (Fig. 4.2 b). With respect to the CTRL experiment, a slight weakening of the equatorial trade winds is noted. In the DRAG experiment the SST bias is further reduced, with a cold bias of 1.0°C (Fig. 4.2 c). A reduction of the off-equatorial mean wind stress, in the western Pacific near 12°N and in the eastern Pacific near 12°S is noted. A further reduction of the SST bias occurs in the BOTH experiment, together with decreasing trade winds (Fig. 4.2 d). The eastern equatorial SST further improves in the DRAG_S experiment (Fig. 4.2 e), however, in the far eastern Pacific, a warm bias appears. Furthermore, a reduction of the trade winds for the whole equatorial Pacific is noted. Trade wind reduction is strongest in the BOTH_S experiment (Fig. 4.2 f). The cold bias is reduced to a patch near 140°W. Warmer than observed SST occurs in the western and the far eastern equatorial Pacific.

To further illustrate the climatological changes among the experiments, equatorial (2°N-2°S) averages of wind stress, SST, thermocline depth and thermocline intensity are calculated. The mean thermocline depth is calculated as the annual mean 20°C isotherm depth. The thermocline intensity is calculated as the difference in meters between the 16°C and 22°C isotherm depths.
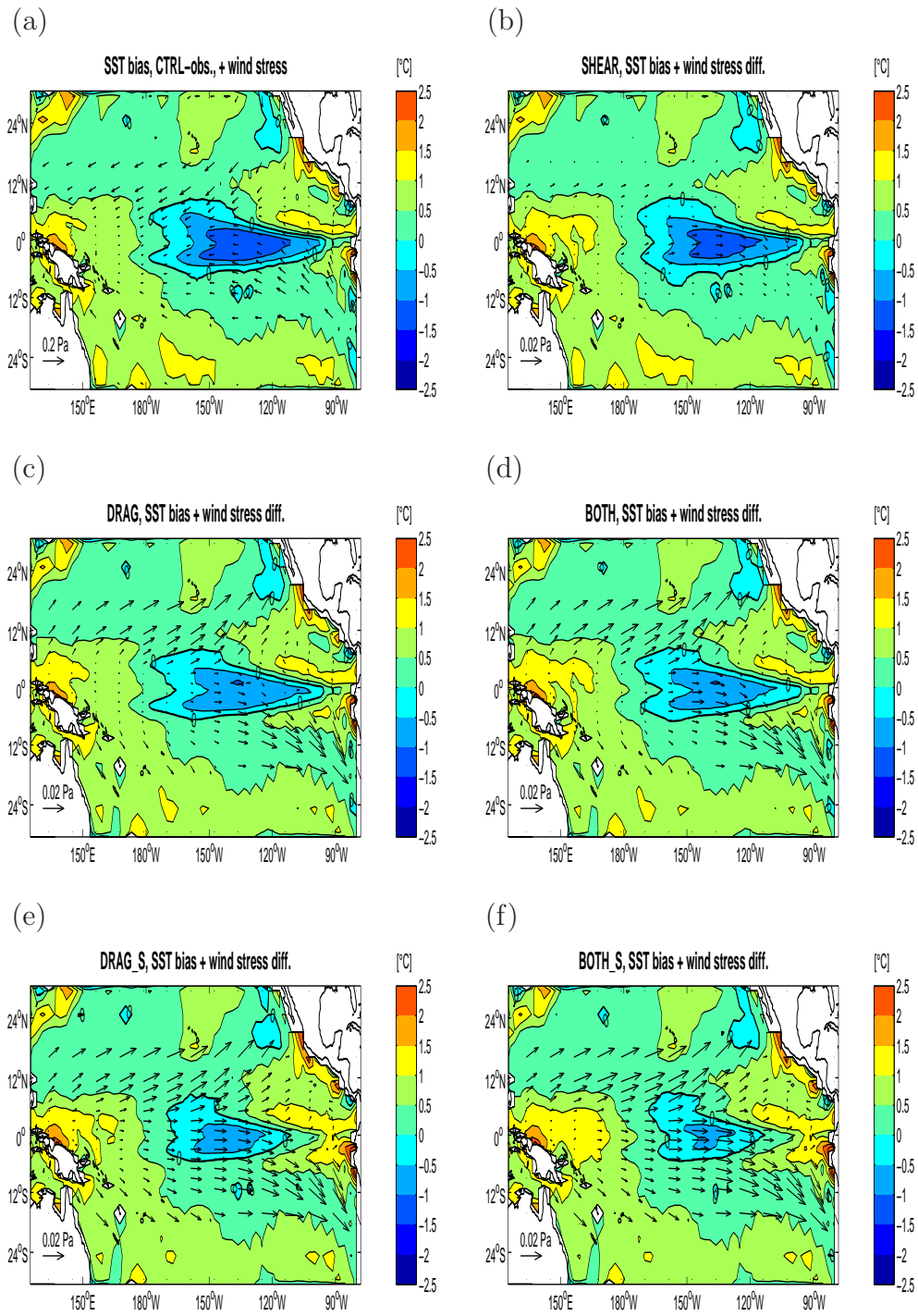
**Fig. 4.2:** *Mean SST bias of the uncoupled experiments. The SST bias is calculated with respect to Levitus and Boyer (1994) observations (shaded, in °C). Shown experiments: CTRL (a), SHEAR (b), DRAG (c), BOTH (d), DRAG_S (e) and BOTH_S (f). In panel (a) the wind stress vectors of the CTRL experiment are superimposed. In (b-f) the difference vectors of the modelled mean wind stresses with respect to the CTRL experiment are superimposed.*

(a)



(b)



(c)



(d)
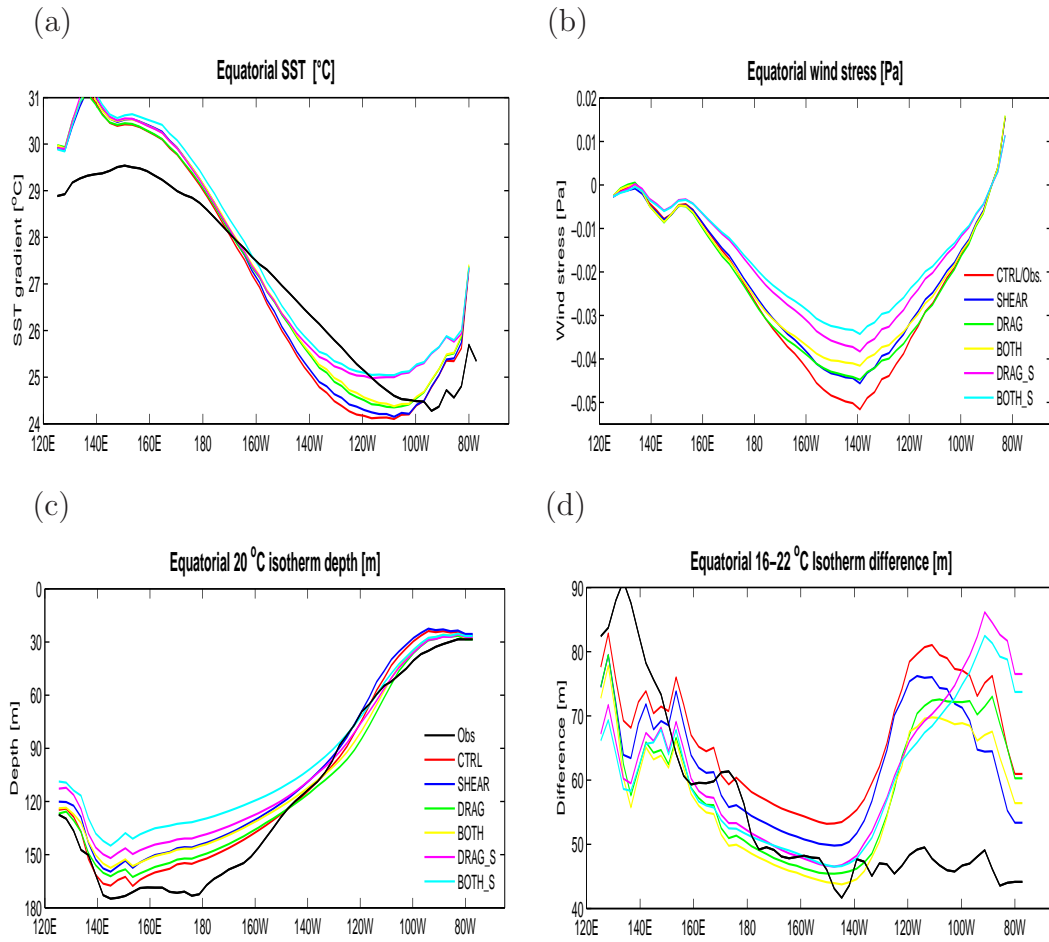


**Fig. 4.3:** *Equatorial (2°N-2°S) averages of the uncoupled experiments: (a) SST (°C), (b) wind stress (Pa), (c) thermocline depth (m) and (d) thermocline intensity (m). In (a), (c) and (d) observed values from Levitus and Boyer (1994) are depicted as solid black line. In (b) the OMIP mean wind stress from the CTRL experiment is used as reference observation (solid red line)*

The simulated equatorial averages for SST exhibit a 1-2°C higher temperature, west of the dateline, compared to Levitus and Boyer (1994) observations (Fig. 4.3 a). The warm bias is already noted in Chapter 2 and changes only slightly among the experiments. In the eastern equatorial Pacific, the SST bias is reduced. In the DRAG_S and BOTH_S experiments the SST improves between the dateline and 120°W, however, further to the east the cold bias switches to a warm bias. In the DRAG and BOTH experiments an improved simulation of SST is visible between 170°W-100°W.

The equatorial averages of mean wind stress show a general weakening for all experiments. The maximum decrease is simulated in the BOTH_S experiment, where the absolute mean wind stress near 140°W reduces by 0.01-0.02 Pa (Fig. 4.3 b). Overall, the simulated mean thermocline depths

are shallower in the western Pacific, while east of 140°W a deepening occurs (Fig. 4.3 c). In the eastern Pacific the model has difficulties to simulate the observed thermocline intensities (Fig. 4.3 d). In the experiments the thermocline intensities are partly improving, with best values for DRAG and BOTH parameterization. East of 100°W the thermocline intensity degrades in the DRAG_S and BOTH_S experiments.

The simulated SST variability, as given by the standard deviations for each spatial grid point, is shown in Figure 4.4. The panels on the left (Fig. 4.4 a,c,e) denote the experiments without shear correction (CTRL, DRAG, DRAG_S), while the panels in the right column (Fig. 4.4 b,d,f) denote the experiments with shear correction (SHEAR, BOTH, BOTH_S). The variability shows the typical structure, with a maximum in the equatorial eastern Pacific. Overall, the variability is decreasing from left to right and from top to bottom panels. Very weak variabilities are found in the BOTH and BOTH_S experiments (Fig. 4.4 d and e).
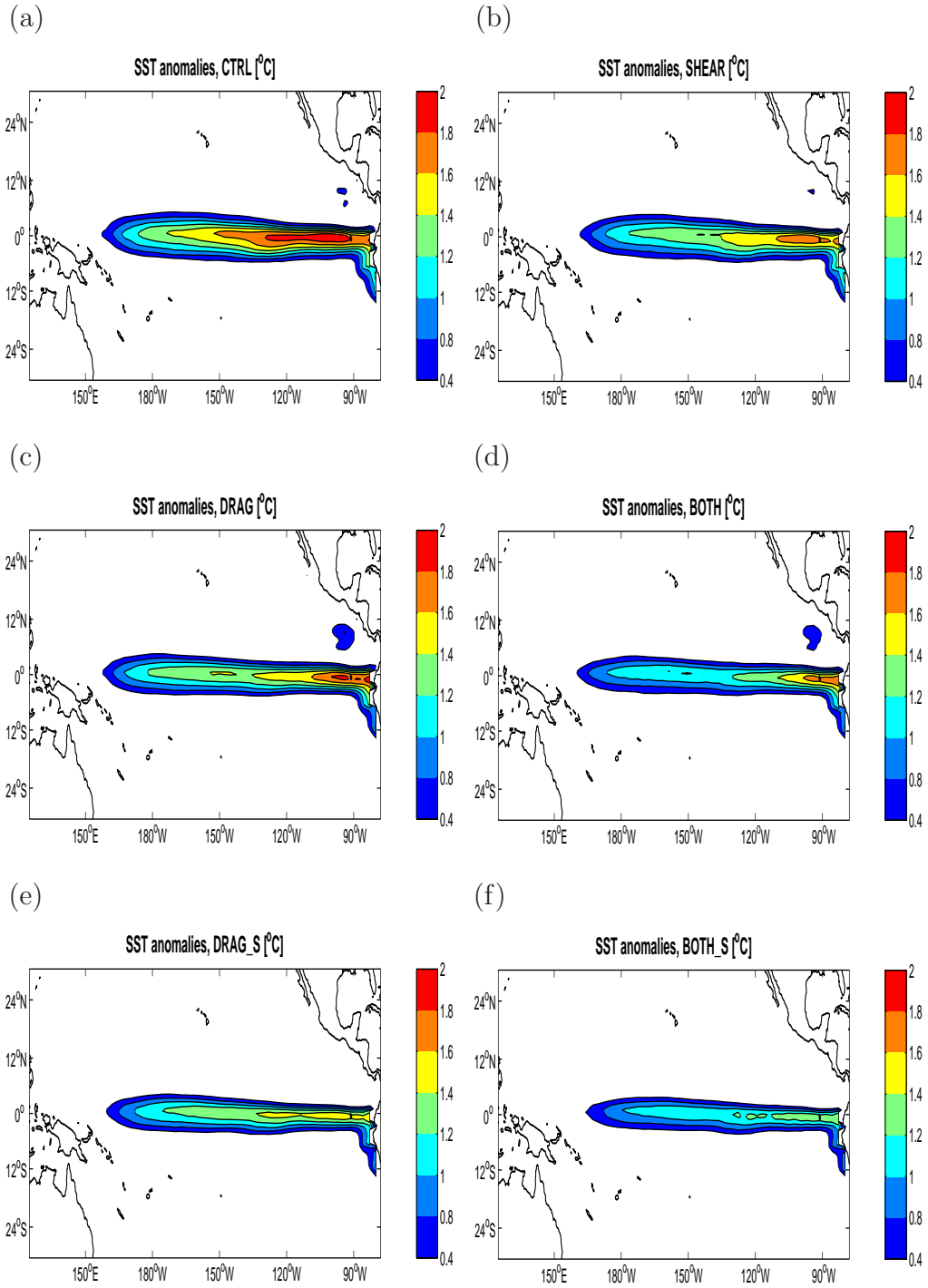
**Fig. 4.4:** *Standard deviation of SST variability for the uncoupled simulations (shaded, in °C) . Shown are the standard deviations for (a) CTRL, (b) SHEAR, (c) DRAG, (d) BOTH, (e) DRAG_S and (f) BOTH_S experiments.*

**Equatorial SST variabillity**
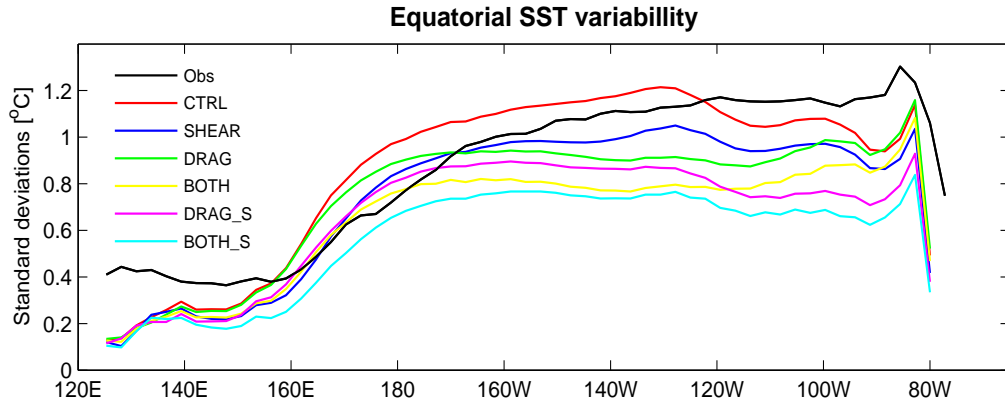


**Fig. 4.5:** *Equatorial (2°N-2°S) averages of the SST variability (in °C) for the uncoupled experiments.*

Equatorial (2°N-2°S) averages of the SST variability are shown in Figure 4.5. The general decrease in the experiments is further highlighted. In the CTRL experiment (red line) the variability declines east of 130°W. The relative decline is also noted in the other experiments, but is absent in the DRAG (green line) and BOTH (yellow line) experiments.

The simulated zonal wind stress variability, calculated as standard deviations for each spatial grid point is illustrated in Figure 4.6. The zonal wind stress variability shows two pronounced local maxima, both at the equator near the dateline and between 120°W and 140°W (Fig. 4.6 a). As for the SST variability, the wind stress variability is decreasing from left to right and from top to bottom panels. Some qualitative differences can be seen in the structure of the zonal wind stress anomalies. In the DRAG and BOTH experiments (Fig. 4.7 c,d) the anomalies are markedly reduced between 120°W and 140°W. Furthermore, the local maximum near the dateline is shifted westward to 170°E. The equatorial (2°N-2°S) averages of the zonal wind stress variability further illustrates the decreasing trend (Fig. 4.7), and the relative spatial reduction and shift in the DRAG and BOTH experiments.

Estimates of the Nino-3 index (averages for 5°N-5°S and 90°W-150°W) of the SST anomalies as well as Nino-4 index (averages for 5°N-5°S and 160°E-150°W) for zonal wind stress anomalies were calculated and their respective standard deviations are summarized in Table 4.2. The application of shear correction reduces the variability of the Nino-3 (Nino-4) time series by 9-13 (8-14) percent. The impact of the DRAG_S parameterization on variability is about 10 percent stronger than the impact of the DRAG parameterization.

As mentioned in Chapter 2 the relationship between the eastern equatorial SST anomalies and the western equatorial wind stress anomalies is an important parameter for the ENSO dynamics. Here, the regression coefficient between Nino-3 SST and Nino-4 zonal wind stress time series are
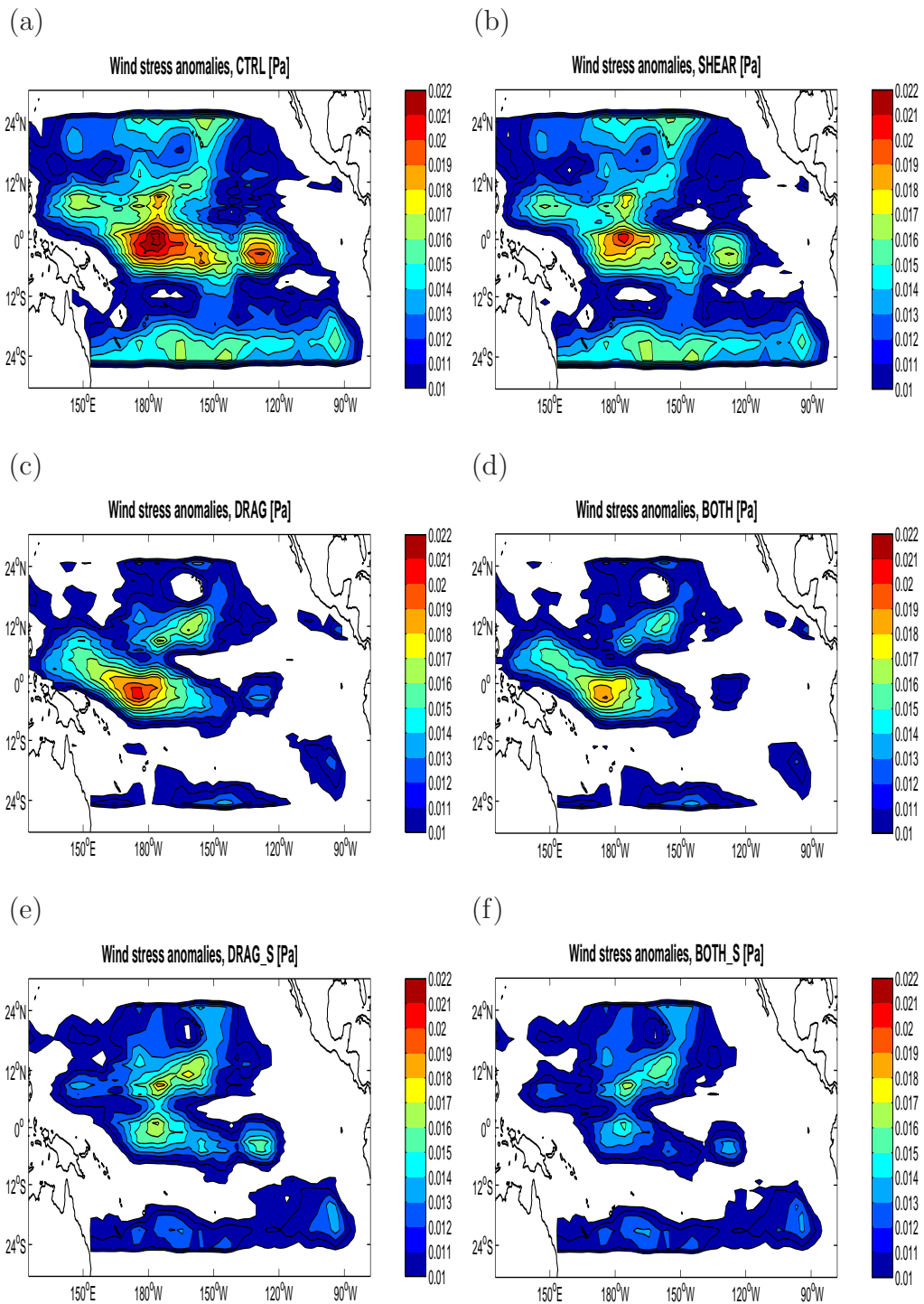
**Fig. 4.6:** *Standard deviation of zonal wind stress anomalies for the uncoupled simulations (in Pa). Shown are the standard deviations for (a) CTRL, (b) SHEAR, (c) DRAG, (d) BOTH, (e) DRAG_S and (f) BOTH_S experiments.*
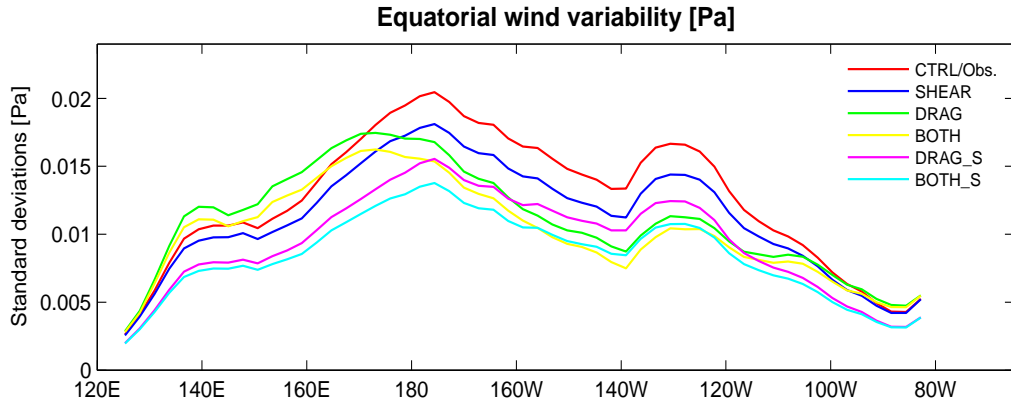
**Fig. 4.7:** *Equatorial (2°N-2°S) of the zonal wind stress anomalies (Pa) for the uncoupled experiments.*

calculated and summarized in Table 4.2. The coefficients and correlations vary only slightly in the different experiments.

| Experiment | Nino-3 [°C] | Nino-4 [Pa] | Regression [Pa/°C] |
|:---:|:---|:---|:---|
| CTRL | 0.93 | 0.0142 | 0.0106 (0.70) |
| SHEAR | 0.81 (-13%) | 0.0122 (-14%) | 0.0106 (0.71) |
| DRAG | 0.77 (-17%) | 0.0121 (-15%) | 0.0109 (0.70) |
| BOTH | 0.67 (-28%) | 0.0110 (-23%) | 0.0116 (0.71) |
| DRAG_S | 0.68 (-27%) | 0.0106 (-25%) | 0.0113 (0.73) |
| BOTH_S | 0.059 (-36%) | 0.0091 (-36%) | 0.0111 (0.72) |

**Tab. 4.2:** *Standard deviations for Nino-3 SST anomalies and Nino-4 wind stress anomalies in uncoupled mode, and the estimated regression coefficients for Nino-3 SST versus Nino-4 wind stress. For Nino-3 and Nino-4 the values in parentheses denote the increase or reduction in comparison to the CTRL run. For the regression coefficient, the value in parentheses denotes the correlation.*

In summary, the various formulations have a large impact on the simulated climatological state of SST, wind stress and thermal structure. The simulated cold SST bias is reduced with respect to observations. In some experiments the cold bias turns into a warm bias in the western and far eastern equatorial Pacific. Overall the mean wind stresses are reduced due to the parameterizations, especially in the DRAG_S and BOTH_S experiments. Mean thermocline depth and thermocline intensity improve in the eastern equatorial Pacific. Overall, the simulated SST and wind stress variabilities decrease due to the parameterizations. The application of the shear correction (equation 4.2) reduces the Nino-3 variability by 9-13 percent.

In the following section, similar analyses will be performed using the HCM in coupled mode.

# 4.3   Coupled simulations

## 4.3.1   Experimental setup

In coupled mode, HCM simulations where carried out for all parameterizations as in the uncoupled mode. Coupled mode experiments with a coupling coefficient set to Cp=1.0, 1.25 and 1.4 are performed. For a coupling of 1.4 the CTRL and SHEAR experiments showed unrealistically high amplitude and where therefore neglected. The different experiments are summarized in Table 4.3.

| Experiment | Cp | Drag param. | Shear | Comment |
|---|---|---|---|---|
| CTRL | 1.0 | $C_d = 0.0013$ | no | standard experiment |
| SHEAR | 1.0 | $C_d = 0.0013$ | yes | shear corr. only |
| DRAG | 1.0 | Eq. 4.5 | no | drag corr. only |
| BOTH | 1.0 | Eq. 4.5 | yes | shear + drag |
| DRAG_S | 1.0 | Eq. 4.4 | no | drag (Smith, 1988) |
| BOTH_S | 1.0 | Eq. 4.4 | yes | shear + drag (Smith, 1988) |
| CTRL(1.25) | 1.25 | $C_d = 0.0013$ | no | Control run |
| SHEAR(1.25) | 1.25 | $C_d = 0.0013$ | yes | shear only |
| DRAG(1.25) | 1.25 | Eq. 4.5 | no | drag only |
| BOTH(1.25) | 1.25 | Eq. 4.5 | yes | shear + drag |
| DRAG_S(1.25) | 1.25 | Eq. 4.4 | no | drag (Smith, 1988) |
| BOTH_S(1.25) | 1.25 | Eq. 4.4 | yes | shear + drag (Smith, 1988) |
| DRAG(1.4) | 1.40 | Eq. 4.5 | no | drag corr. only |
| BOTH(1.4) | 1.40 | Eq. 4.5 | yes | shear + drag |
| DRAG_S(1.4) | 1.40 | Eq. 4.4 | no | drag (Smith, 1988) |
| BOTH_S(1.4) | 1.40 | Eq. 4.4 | yes | shear + drag (Smith, 1988) |

**Tab. 4.3:** *Table of parameterizations for the coupled experiments.*

The different experiments are analyzed with respect to the simulated interannual variability. For this purpose, the Nino-3 time series for SST anomalies and the Nino-4 time series for wind stress anomalies are calculated. Furthermore, the first EOFs of SST and wind stress anomalies and their associated principal components are calculated for the experiments, as described in Chapter 2, Section 2.3. From this, the associated EOF regression coefficients $C_{1,1}$ as defined in Section 2.3 are calculated.

The results will be compared to a sensitivity study by Jungclaus *et al.* (2006), where experiments with the ECHAM 5/MPI-OM coupled AOGCM in control and shear-like setup where performed. The simulations are called AOGCM CTRL and AOGCM SHEAR.

## 4.3.2 Results

Table 4.4 summarizes the results of the coupled model experiments. The ENSO amplitude is calculated as the standard deviation of the Nino-3 time series. The period is calculated as the second maximum of the autocorrelation function of the Nino-3 index. A couple of experiments show a damped ENSO mode, which makes it difficult to calculate meaningful amplitudes and periods. For simplicity, the values for amplitude and period are calculated as for the self-sustained modes, except for the strongly damped cases, where the mode collapses within a few month after the initialization.

| Experiment | Stdv. [°C] | Period [month] | Regression [0.1Pa/°C] | Skew- ness | Oscillatory mode |
|---|---|---|---|---|---|
| CTRL | 1.01 | 39 | 0.105/0.128 | -2.03 | self sustained |
| SHEAR | 0.33 | 60 | 0.080/0.173 | 0.14 | weakly damped |
| DRAG | 0.49 | 37 | 0.141/0.128 | -0.68 | self sustained |
| BOTH | 0.27 | 38 | 0.165/0.136 | -0.13 | weak self sustained |
| DRAG_S | 0.12 | – | – | – | strongly damped |
| BOTH_S | 0.10 | – | – | – | strongly damped |
| CTRL(1.25) | 1.77 | 44 | 0.140/0.232 | -1.26 | self sustained |
| SHEAR(1.25) | 1.55 | 38 | 0.127/0.219 | -1.15 | self sustained |
| DRAG(1.25) | 0.47 | 38 | 0.063/0.208 | -1.61 | self sustained |
| BOTH(1.25) | 0.31 | 48 | 0.140/0.178 | -0.72 | weak self sustained |
| DRAG_S(1.25) | 0.25 | 53 | 0.142/0.208 | 0.09 | damped |
| BOTH_S(1.25) | 0.14 | – | – | – | strongly damped |
| DRAG(1.4) | 1.13 | 43 | 0.055/0.020 | -1.91 | self sustained |
| BOTH(1.4) | 0.35 | 49 | 0.044/0.208 | -0.56 | weak self sustained |
| DRAG_S(1.4) | 1.17 | 50 | 0.286/0.314 | -2.20 | self sustained |
| BOTH_S(1.4) | 0.21 | – | – | – | strongly damped |
| AOGCM CTRL | 1.76 | 37 | 0.040/0.074 | 0.032 | – |
| AOGCM SHEAR | 1.34 | 44 | 0.048/0.014 | 0.010 | – |
| Observed | 0.8 | 36-72 | 0.090/– | 0.86 | – |

**Tab. 4.4:** *Indices for the coupled experiments. Stdv. denotes the standard deviation of the simulated Nino-3 SST time series. Period denotes the period of the Nino-3 time series. Regression coefficients are calculated for the Nino-3 SST anomalies and Nino-4 wind stress anomalies (left values) and for the EOF regression coefficient $C_{1,1}$ (right values). Furthermore, the skewness of the Nino-3 SST time series is calculated. In the DRAG_S, BOTH_S, BOTH_S(1.25) and BOTH_S(1.40) the system was overdamped and thus meaningful values for regression, period and skewness could not be calculated. For the AOGCM and observations the oscillatory mode cannot be determined.*

There is a large spread of the periods, amplitudes and regression co-efficients among the experiments. Overall, the variability decreases if the shear correction (equation 4.2) is applied. With the coupling parameter set to 1.0 the amplitude decreases from a standard deviation of 1.01°C to values below 0.5°C in the experiments. In the SHEAR experiment the oscillation is slightly damped. The DRAG and BOTH parameterization exhibit self sustained modes with weak amplitudes. The period of the oscillations is around 38 month, except for the SHEAR experiment, where the cycle is 60 month. Except for the SHEAR experiment, the skewness is negative in the experiments, but improves in comparison to the CTRL experiment. In the DRAG_S and BOTH_S case the mode immediately collapses, so a meaningful calculation of skewness and period was not feasible.

The regression coefficient of Nino-3 SST anomalies to Nino-4 wind stress anomalies is close to the observed values (taken from Latif *et al.* (2001)) in the CTRL and SHEAR experiment, but is higher in the DRAG and BOTH experiments. From the uncoupled experiments it is clear that the spatial patterns of variability may differ considerably between the experiments. Thus, the regression coefficients between Nino-3 SST anomalies and Nino-4 wind stress anomalies may not take the important spatial pattern into account. Therefore, the first EOF regression coefficient $C_{1,1}$ is calculated, which takes the spatial patterns into account.

With a coupling of 1.25 the amplitude increases in the CTRL(1.25) and SHEAR(1.25) experiments. The overall characteristics of the SHEAR(1.25) experiment changes in comparison to the SHEAR, with higher amplitudes, lower periods, a negative skewness and a self sustained ENSO mode. The DRAG(1.25) and BOTH(1.25) experiments show weak self sustained modes. A general notion is the reduction of the amplitude due to the shear param-eterization (equation 4.2).

The DRAG_S(1.25) and BOTH_S(1.25) experiments show nearly no variance. Further experiments with a coupling of 1.4 lead to self sus-tained modes with amplitude above 1.0 in the DRAG(1.4) and BOTH(1.4) case but only to a very weak mode in the DRAG_S(1.4) case. Even with this relatively high coupling, no reasonable variability was achieved in the BOTH_S(1.4) case.

In addition to the HCM experiments two results from a study with the ECHAM-5/MPI-OM AOGCM from the study by Jungclaus *et al.* (2006) are added to the table, where CTRL and SHEAR like sensitivity exper-iments were performed. The AOGCM experiment underlines the general notion that the application of the shear correction (equation 4.2) leads to a reduced Nino-3 amplitude. However, there are no simple trends visible in the relationships between amplitude, period and regression coefficients. The comparison to the AOGCM results show a decrease when shear correction is applied, but the period increases in the AOGCM SHEAR. This is con-
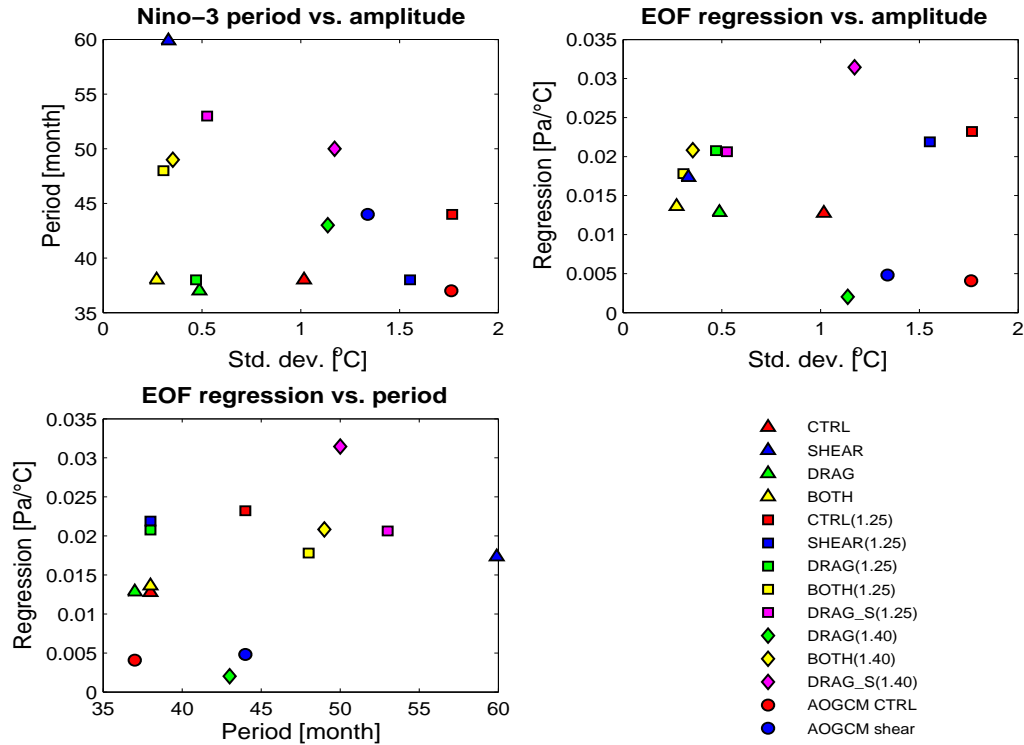
**Fig. 4.8:** *Nino-3 Indices of the coupled experiments. Upper left panel: period versus standard deviation. Upper right panel: EOF regression coefficient $C_{1,1}$ versus standard deviation. Lower panel: EOF regression coefficients $C_{1,1}$ versus period.*

sistent with the CTRL and SHEAR experiments but inconsistent with the CTRL(1.25) and SHEAR(1.25) experiments, where the period decreases.

There is a large spread of the periods, amplitudes and regression coefficients among the experiments. To make the results more accessible, scatter plots of the standard deviation, period and EOF regression $C_{1,1}$ are shown in Figure 4.8. The experiments do not exhibit a linear relationship between period and amplitude (Fig. 4.8, upper left panel). Also, no clear relationship is visible between $C_{1,1}$ and amplitude (Fig. 4.8, right panel). The period versus EOF regression coefficient $C_{1,1}$ indicates a trend, where a higher $C_{1,1}$ is associated with a higher period (Fig. 4.8, lower panel).

In Chapter 3 it was shown that the period of the simulated Nino-3 is decreasing as a function of the mean wind stress. According to Chapter 3 the amplitude can be estimated as a linear function of the ocean to atmosphere coupling, where the EOF regression coefficient $C_{1,1}$ was used as a measure of the coupling. For comparison, the simulated mean wind stress for the experiments is calculated for the area between 130°E-85°W and 5°N-5°S. Scatter plots of period versus EOF regression coefficients, period versus mean wind stress and amplitude versus EOF regressions coefficients are
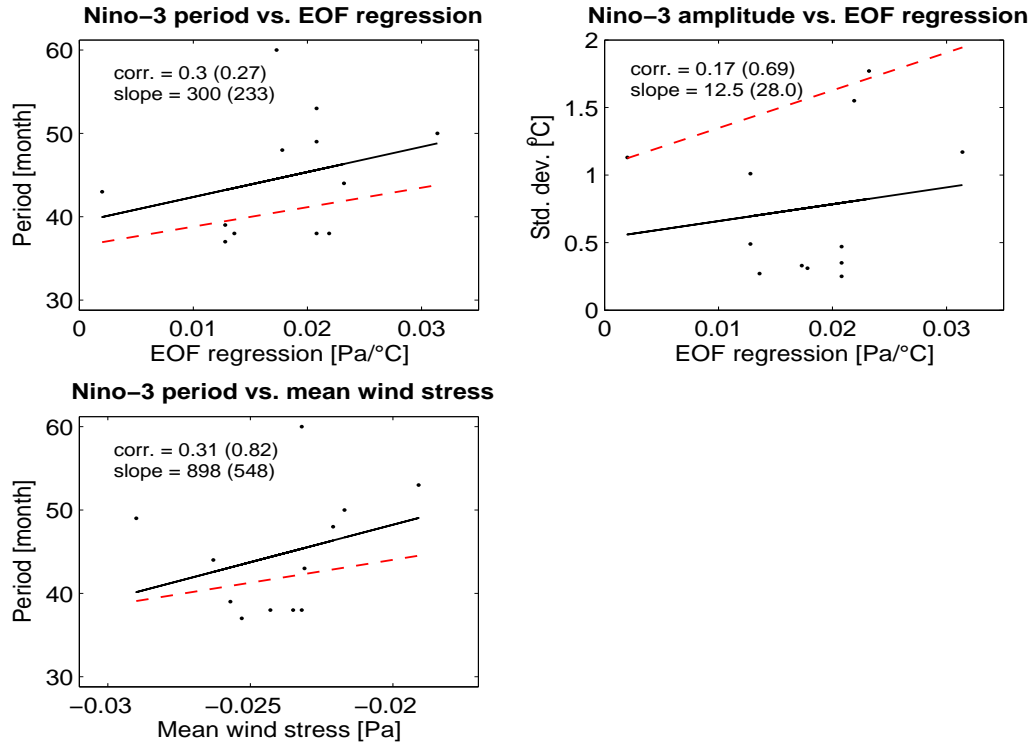
**Fig. 4.9:** *Comparison of the Nino-3 indices of the coupled experiments with results of Chapter 3. Upper left panel: scatter plot of the Nino-3 period versus the EOF regression coefficient $C_{1,1}$. Upper right panel: Nino-3 SST amplitude versus $C_{1,1}$. Lower panel: Nino-3 period versus mean wind stress. The linear regression curves (solid black) are plotted together with the regression curves estimated in Chapter 3 (dashed red curve). The numbers in brackets depict the associated slopes and correlations from Chapter 3, Tables 3.2.*

shown (Fig. 4.9). Furthermore, the least squares linear regression estimates (black solid lines) and the regression curves (red dashed lines) calculated in Chapter 3 (Table 3.2) are drawn. The results suggest that the relationship between period and EOF regression coefficients is weak (correlation of 0.3) (Fig. 4.9, upper left panel). However, in comparison to the results from Chapter 3, the linear regression estimates are comparable. The relationships between period and mean wind stress, which were a prominent feature of the results in Chapter 3, are much lower in the sensitivity experiments of this chapter (Fig. 4.9, lower panel). The relationship of amplitude and ocean-to-atmosphere coupling (Fig. 4.9, right panel) was not reproduced.
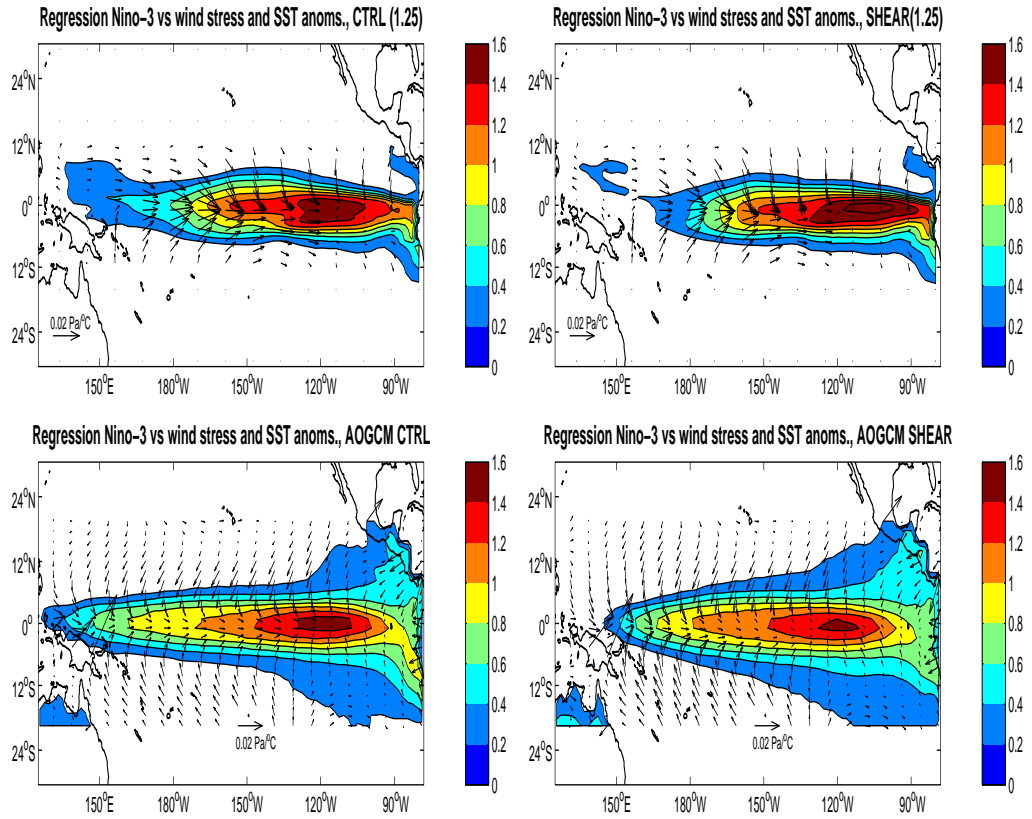
**Fig. 4.10:** *Spatial regression of the Nino-3 SST time series versus SST and wind stress anomalies. Upper panels: regressions for the CTRL(1.25) and SHEAR(1.25) experiments. Lower panels: regressions for the AOGCM experiments from Jungclaus* et al. *(2006).*

The spatial regression of Nino-3 SST anomalies versus SST and wind stress anomalies for the CTRL(1.25) and SHEAR(1.2) experiment (upper panels) and the AOGCM experiments from Jungclaus *et al.* (2006) (lower) are shown in Fig. 4.10. The AOGCM SHEAR experiment shows a wider latitudinal extension and is more confined to the eastern basin in comparison to the AOGCM CTRL experiment. The SHEAR(1.25) also shows a concentration in the eastern basin but no latitudinal extension in comparison to the CTRL(1.25) experiment. The AOGCM results differ in strength and extension to the HCM experiments, but are more realistic in comparison to observations (see Jungclaus *et al.* (2006)).

## 4.4   Summary and conclusions

In this chapter a hybrid coupled model is used to investigate the sensitivity of ENSO to various wind stress parameterizations. Starting from the common empirical bulk formula 4.1 first the ocean surface currents are taken into account. Specifically, the wind speed $u$ is corrected for the surface motion with the formula $u^* = u - u_o$, where $u_o$ denotes the ocean surface speed. In further tests, the constant drag $C_d$ is replaced by a function of the wind speed $C_d = C_d(u^*)$. Two drag parameterizations were analyzed: First, a parameterization (following Smith (1980, 1988)) with a nearly constant value for wind speeds below 6.0 m/s, and second, a parameterization with a linearly increasing drag for decreasing wind speed below 6.0 m/s, which is an estimate of recent ocean measurements (e.g. Trenberth *et al.* (1989); Wu (1994); Yelland and Taylor (1996); Yelland *et al.* (1998); Large and Pond (2004)). Sensitivity studies in coupled and uncoupled are carried out to give an overview of possible changes due to the different parameterizations.

In uncoupled mode the easterly trade winds generally decrease in all experiments. A general feature is the decrease in wind stress and SST variability, when the shear adaption $u^* = u - u_o$, is taken into account, however, the formulations of the drag $C_d = C_d(u^*)$ generally have a stronger impact on the wind speed reduction than the shear correction alone. The reduction of easterly wind stress leads to a reduced eastern Pacific cold bias, which improves by 1-1.5°C in some experiments, but is also accompanied by a warm bias in the far eastern equatorial Pacific. In uncoupled mode, the variability of wind stress and SST generally decreases, but spatial differences in the decrease are seen, particularly in the eastern versus western Pacific variability.

The reduction in variability carries over to the coupled simulations, where the variability immediately decreases when the extended bulk formula is applied. In coupled mode a large spread in ENSO characteristics among the different experiments is apparent. Generally, the shear parameterization ($u^* = u - u_o$) alone leads to reduced variability in comparison to the standard run. In some experiments, the ENSO mode changes from self sustained to damped mode. Especially, the first drag parameterization (after Smith (1980, 1988)) generally leads to a strongly damped mode, while the second parameterization leads to reduced but relatively robust self sustained variability.

In comparison with the results of Chapter 3 the behavior of ENSO period versus mean wind stress and ENSO amplitude versus coupling, which were prominent in Chapter 3, could not be reproduced. The relationship between EOF regression coefficient $C_{1,1}$, which serves as a measure of the anomalous ocean-to-atmosphere coupling, and the ENSO period are positively correlated. This is confirmed by the results of Chapter 3, where the

least squares linear regressions exhibits correlations and slopes of similar magnitude.

In comparison to the AOGCM study by Jungclaus *et al.* (2006), where a shear-like sensitivity experiment was performed with the coupled ECHAM5/ MPI-OM, the ENSO amplitude shows a similar behavior for the experiments, i.e. the amplitude is decreasing when shear correction $(u^* = u - u_o)$ is applied. However, in the shear experiment with stronger coupling the ENSO period is decreasing, while in the ECHAM5/MPI-OM the period is increasing.

Generally, the coupled experiments show the large sensitivity of the coupled system to small changes in the parameterizations. The formulations of the drag as function of the wind speed, $C_d = C_d(u^*)$, differs only for wind speeds below 6.0 m/s, however, some experiments showed nearly no variability and some experiments showed robust ENSO amplitudes and periods. The experiments emphase the need for correct ocean-atmosphere parameterizations also for low wind speeds and seemingly low momentum fluxes. Since the parameterizations generally lead to reduced tropical Pacific variability, especially those models, where the variability is too high, an improved momentum flux might lead to better results.

# 5. CONCLUSIONS AND OUTLOOK

In this thesis the El Niño-Southern Oscillation (ENSO) phenomenon was investigated with a hybrid coupled general circulation model of the tropical Pacific ocean-atmosphere system. Two main questions were addressed: First, the interactions between the climatological mean state and the ENSO variability were investigated. The motivation to address this question stems from the relatively sparse knowledge regarding future climatic conditions and its impacts on ENSO dynamics. The second question addressed the potential improvement of the momentum flux at the ocean-to-atmosphere boundary in coupled atmosphere-ocean general circulation models (AOGCMs). Here, it was investigated how the standard bulk formula for wind stress (equation 4.1) could be improved with respect to a moving ocean surface and a parameterization of the drag, $C_d$, as a function of wind speed.

For these purposes a hybrid coupled model (HCM) of the tropical Pacific basin was constructed and used. The advantages of the HCM, with respect to intermediate complexity models (ICMs) and fully coupled AOGCMs, are threefold: First, in contrast to ICMs, the HCM takes nonlinear interactions between the ocean interannual variability and processes with lower periods into account. Second, the setup of the HCM allows to prescribe the climatological background state via the mean wind stress forcing and the anomalous ocean-to-atmosphere coupling, and third, the lower complexity, i.e. computational cheapness in comparison to fully developed AOGCMs, allows a large volume in parameter space to be surveyed.

To address the question of the interactions between the mean state and El Niño variability, a set of experiments was carried out, where the mean wind stress strength was varied between 60 percent and 160 percent of the OMIP climatological wind stress. Furthermore, the anomalous ocean to atmosphere coupling was varied between 0.7 and 1.2, a range where self-sustained ENSO activity with realistic periods and amplitudes occurred. Results showed that the mean zonal thermocline depth deepens, and the mean zonal SST gradient increases with increasing mean wind stress, while the intensity of the thermocline decreases. Furthermore, increased wind stress decreases the period of ENSO. The ENSO amplitude is strongly affected by the coupling coefficient and less affected by the mean wind stress.

The stronger amplitude due to higher coupling reduces the thermocline intensity and the surface temperature gradient. Various regression coefficients and associated correlations were calculated and summarized in Table 3.2 and Table 6.3. Results of ICM studies by Fedorov and Philander (2001), who investigate the ENSO period as a function of the mean background state, at first view disagree with the results of this study. A further analysis indicates that this is due to the prescribed thermocline intensity in the ICM, which, when varied, has a large effect on the period. The comparison highlights the difficulties to compare results from models with reduced physics, such as ICMs, to complex general circulation models. On the other hand, a comparison of AOGCM simulations from the ENSIP study (Latif *et al.* (2001)) showed no relationships comparable to the HCM results. Reasons for this absence may lie in the known problems of AOGCMs to simulate both realistic climatologies as well as tropical Pacific variabilities (e.g. Latif *et al.* (2001); Davey *et al.* (2002); AchutaRao and Sperber (2002); Stockdale *et al.* (1998)).

To address the question of the atmosphere-to-ocean momentum flux, the common bulk formula (equation 4.1) was reformulated to include the motion of surface currents. Furthermore, the drag constant was extended to a function of the wind speed. Two drag parameterizations were analyzed: A parameterization (following Smith (1980, 1988)) with a nearly constant value for wind speeds below 6.0 meters per second, and a parameterization with a linearly increasing drag for decreasing wind speed below 6.0 meters per second, which is an estimate of recent ocean measurements (e.g. Trenberth *et al.* (1989); Wu (1994); Yelland and Taylor (1996); Yelland *et al.* (1998); Large and Pond (2004)). In uncoupled mode the parameterizations lead to a mean reduction of wind stress and consequently to a reduction in the mean equatorial zonal SST gradient and the eastern Pacific SST bias. The SST bias could spatially be reduced by 1°C. Furthermore, in uncoupled mode, El Niño amplitude reduces as a consequence of reduced wind stress anomalies. In some experiments, local maximum wind stress anomalies were reduced and zonally shifted. In the coupled mode, the improved parameterization generally leads to reduced El Niño amplitudes. Furthermore, according to the parameterization, the system can change from self sustained to damped mode. A weak relationship between anomalous coupling, measured as the EOF regression coefficient $C_{1,1}$, and the period is noted, and sustained by the results of Chapter 3. However, the relationships between mean wind stress and period, and anomalous coupling and amplitude which where apparent in Chapter 3 could not be reproduced. Further, it can be seen that the model studies roughly agree with results from a study by Jungclaus *et al.* (2006), where the sensitivity to surface corrections was investigated in the coupled ECHAM5/MPI-OM AOGCM. Taken together, relatively small changes lead to large spread of amplitude, period and overall ENSO characteristics among the experiments, which em-

phasize the need for realistic wind stress parameterization.

The aim of this thesis was to give an overview of possible changes of the mean and anomalous wind stress formulation on ENSO variability. The investigations focused on the ocean mean thermal structure, SST and the ocean to atmosphere coupling. These values are relatively easy to obtain from other model studies and from observations, therefore, relatively quick comparisons among the models are feasible. In future studies, the HCM results should be used to obtain a clearer view of the relationships between the mean background state and ENSO characteristics. The AOGCM results in Chapter 3 did not reveal a consistent picture, however, the continuous efforts to improve AOGCMs may lead to more settled results.

The existing body of theory for ENSO dynamics explains the relationship between amplitude and anomalous ocean to atmosphere coupling. Future theoretical studies should give a more detailed explanation for both the relationship of ENSO period and mean background state, and the weak relationship between anomalous coupling and ENSO period, as simulated by the HCM.

In the experimental setups the effect of weather or short term climatic noise is rigorously neglected. The neglection of the noise component reduces potential masking effects and thus allows to study the eigenmodes of the oscillation. However, a self sustained ENSO mode without noise forcing requires a relatively high coupling, which leads to ENSO amplitudes higher than observed and may also cause the unrealistic negative skewness of the modelled ENSO. Further, it is generally believed that the observed ENSO dynamics is near the bifurcation between a self sustained mode and damped mode sustained by noise forcing (Kessler (2002); Philander (2003)). Therefore, future HCM studies should include a noise component to investigate ENSO characteristics near the bifurcation point.

# 6. APPENDIX

## 6.1 Linear regression on a sphere

The spatial distribution of geophysical data on a sphere is usually not uniform. To do a meaningful linear regression, it is thus necessary to weight the data with respect to the associated spatial area (e.g. Cohen and Jones (1969); Buell (1971)). The linear regression scheme described in Chapter 3 for the statistical atmosphere model changes as follows: Given a discrete data set of temperatures $T_{i,j} = T(x_i, t_j)$ and wind stress anomalies $\tau_{i,j} = \tau(x_i, t_j)$. For simplicity it is assumed that both data sets are of equal size, $i = 1, \ldots N, j = 1, \ldots M$ and sampling rate is a constant. With a weighting function $\omega_i = \omega(x_i)$, where $\sum_i \omega_i = 1$, one needs to calculate:

$$T_{i,j}^{\omega} = T_{i,j} (\omega_i)^{\frac{1}{2}} \tag{F.1.1}$$

$$\tau_{i,j}^{\omega} = \tau_{i,j} (\omega_i)^{\frac{1}{2}} \tag{F.1.2}$$

The corresponding principal component decomposition is

$$T_{i,j}^{\omega} = \sum_m \alpha_{m,i}^{\omega} e_{m,i}^{\omega} \tag{F.1.3}$$

$$\tau_{i,j}^{\omega} = \sum_n \beta_{n,j}^{\omega} f_{n,i}^{\omega} \tag{F.1.4}$$

where $e_m^{\omega}(x)$ and $f_n^{\omega}(x)$ are the Eigenvectors of the associated covariance matrices $R_{\omega} = Cov(T_{\omega})$ and $S_{\omega} = Cov(\tau_{\omega})$.

The matrix of regression coefficients can be estimated as:

$$C_{n,m}^{\omega} = \frac{< \alpha_m^{\omega} \beta_n^{\omega} >}{< (\alpha_m^{\omega})^2 >} \tag{F.1.5}$$

where $< \ldots >$ denotes time average. Thus, with a given SST anomaly $\hat{T}(x_i, t_j)$ a linear wind stress anomaly $\hat{\tau}(x_i, t_j)$ can be obtained via

$$\hat{T}_{\omega}(x_i, t_j) = \hat{T}(x_i, t_j) (\omega_i)^{\frac{1}{2}} \tag{F.1.6}$$

$$\hat{\alpha}_m^\omega(t_j) \;=\; \sum_i \hat{T}_\omega(x_i, t_j)\, e_m^\omega(x_i) \tag{F.1.7}$$

$$\hat{\beta}_n^\omega(t_j) \;=\; \sum_m C_{n,m}\, \hat{\alpha}_m(t_j), \tag{F.1.8}$$

$$\hat{\tau}_\omega(x_i, t_j) \;=\; \sum_n \hat{\beta}_n(t_j)\, f_n^\omega(x_i) \tag{F.1.9}$$

$$\hat{\tau}(x_i, t_j) \;=\; \hat{\tau}_\omega(x_i, t_j)/(\omega_i)^{\frac{1}{2}} \tag{F.1.10}$$

# 6.2 Addendum to Chapter 3

## 6.2.1 Tables

| Exp. | Cp = 0.7 | Cp = 0.8 | Cp = 1.0 | Cp = 1.2 |
|---|---|---|---|---|
| $\tau$=0.6 | –/–/– | 5.0/92.8/57.7 | 4.8/103.8/74.1 | 4.0/105.0/78.1 |
| $\tau$=0.8 | –/–/– | 5.9/102.5/59.2 | 5.1/110.3/72.5 | 4.8/110.5/88.6 |
| $\tau$=1.0 | 5.2/113.2/62.7 | 6.3 /113.3/65.3 | 5.9/114.9/75.7 | 5.2/120.7/90.8 |
| $\tau$=1.2 | 5.8/121.5/69.0 | 6.7/121.9/72.9 | 6.2/124.5/83.0 | 5.8/128.7/98.3 |
| $\tau$=1.4 | 6.8/127.1/76.2 | 6.9 /128.4/79.1 | 6.8/132.2/91.0 | 5.9/135.3/98.4 |
| $\tau$=1.6 | –/–/– | 7.1/135.7/85.6 | 6.7/138.7/92.9 | 6.1/145.3/104.4 |

**Tab. 6.1:** *Indices for the coupled model experiments of Chapter 3. The upper row denotes the coupling coefficient and the left column denotes the fraction of the OMIP mean wind stress, as described in Chapter 3. The listed values are the mean climatological values: SST gradient [°C]/mean thermocline depth [meter]/thermocline intensity [meter].*

| Exp. | Cp = 0.7 | Cp = 0.8 | Cp = 1.0 | Cp = 1.2 |
|---|---|---|---|---|
| $\tau$=0.6 | –/–/– | 48/0.99/0.0011 | 42/1.27/0.0181 | 54/1.56/0.0210 |
| $\tau$=0.8 | –/–/– | 43/1.07/0.0013 | 40/1.25/0.0181 | 45/1.75/0.0213 |
| $\tau$=1.0 | 37/1.1/0.0076 | 42 /1.18/0.0085 | 43/1.48/0.0140 | 44/1.77/0.0205 |
| $\tau$=1.2 | 34/1.2/0.0079 | 36/1.42/0.0031 | 39/1.66/0.0131 | 36/1.78/0.0193 |
| $\tau$=1.4 | 31/1.1/0.0083 | 33 /1.26/0.0099 | 38/1.61/0.0045 | 37/1.76/0.0174 |
| $\tau$=1.6 | –/–/– | 31/1.13/0.0066 | 36/1.44/0.0132 | 36/1.71/0.0176 |

**Tab. 6.2:** *Indices for the coupled model experiments of Chapter 3. The values are: Period of the Nino-3 time series/amplitude of the Nino-3 time series/EOF-1 regression coefficient. The units are [month], [°C] and [Pa/°C]. Note that the regression coefficients are absolute values.*

| | SST-$\Delta$ | Z20 | Z20 int. | Cp-EOF | Period | Std. |
|---|---|---|---|---|---|---|
| $\tau$ | **0.82** | **0.96** | 0.60 | -0.13 | **-0.82** | 0.20 |
| Cp | -0.58 | 0.19 | **0.74** | **0.83** | 0.4 | **0.89** |
| SST-$\Delta$ | 1 | 0.65 | 0.08 | -0.58 | **-0.88** | -0.25 |
| Z20 | 0.65 | 1 | **0.78** | 0.12 | **-0.73** | 0.43 |
| Z20 int. | 0.08 | **0.78** | 1 | 0.59 | -0.27 | **0.83** |
| Cp-EOF | -0.58 | 0.12 | 0.59 | 1 | 0.27 | 0.69 |

**Tab. 6.3:** *Correlation coefficients for the regressions in Table 3.2. Values with absolute correlations higher than 0.7 are printed bold.*

| Model | Std. dev. [°C] | Period [month] | SST [°C] | $\tau$ [x OMIP] |
|-------|------|------|------|------|
| CERFACS | 1.04 | 47 | 3.85 | 0.14 |
| COLA | 0.71 | 41 | 2.38 | 0.52 |
| DKRZ-OPYC | 0.79 | 25 | 4.36 | 1.04 |
| HAWAII | 0.94 | 27 | 2.48 | 0.25 |
| LAMONT | 1.35 | 51 | 2.86 | 1.43 |
| MPI | 0.76 | 24 | 5.00 | 1.05 |
| NCAR-CSM | 0.48 | 29 | 2.34 | 1.17 |
| NCAR-WM | 0.50 | 37 | 3.51 | 0.46 |
| NCEP | 0.42 | 31 | 3.70 | 0.07 |
| UCLA | 0.57 | 50 | 3.71 | 0.75 |
| UKMO | 1.13 | 50 | 3.20 | 1.01 |

**Tab. 6.4:** *ENSIP values used in Section 3.4.2. The values are calculated as described in Chapter 3.*

## 6.2.2 Calculation of observed bounds

Observed mean wind stresses are calculated from the NCEP (Kalnay *et al.* (1996)) and FSU (Kalnay *et al.* (1996); Stricherz *et al.* (1997)) wind stress products. The used upper and lower bounds are calculated as the climatological means from FSU (upper bound) and NCEP (lower bound) wind stress. The observed mean thermocline depth is calculated from the SODA dataset (Carton and Giese (2007)). The SODA dataset consists of monthly values from Jan 1958-Dec 2001. To obtain upper and lower bounds, monthly averages for the thermocline depth are calculated as described in Chapter 3. From this time series, the upper and lower bounds are calculated as the maximum and minimum values of a 30-years running mean. In the same manner, the upper and lower bound of the zonal SST gradient is calculated from the HadISST dataset (Rayner *et al.* (2003)).

# BIBLIOGRAPHY

AchutaRao, K. and K. Sperber, 2002. Simulation of the El Niño Southern Oscillation: Results from the coupled model intercomparison project. *Clim. Dyn.*, **19**, 191–209.

Adams, J. B., M. E. Mann and C. M. Ammann, 2003. Proxy evidence for an El Niño-like response to volcanic forcing. *Nature*, **426**, 274–278.

An, S.-I. and B. Wang, 2000. Interdecadal change of the structure of the ENSO mode and its impact on ENSO frequency. *J. Climate*, **13**, 2044–2055.

Barnett, T., M. Latif, N. Graham, M. Fluegel, S. Pazan and W. White, 1993. ENSO and ENSO-related predictability. Part I: Prediction of equatorial Pacific sea surface temperature with a hybrid coupled ocean-atmosphere model. *J. Climate*, **6**, 1545–1566.

Battisti, D. and A. C. Hirst, 1989. Interannual variability in a tropical atmosphere-ocean model: Influence of the basic state, ocean geometry and nonlinearity. *J. Atmos. Sci.*, **46**, 1687–1712.

Bjerknes, J., 1969. Atmospheric teleconnections from the equatorial Pacific. *Mon. Wea. Rev.*, **97**, 163–172.

Blanke, B., J. D. Neelin and D. Gutzler, 1997. Estimating the effect of stochastic wind stress forcing on ENSO irregularity. *J. Climate*, **10**, 1473–1485.

Buell, C. E., 1971. Integral equation representation for factor analysis. *J. Atmos. Sci.*, **28**, 1502–1505.

Burgers, G., F.-F. Jin and G. J. van Oldenborgh, 2006. The simplest ENSO recharge oscillator. *Geophys. Res. Lett.*, **32**. L13706, doi:10.1029/2005GL022951.

Burgers, G. and D. B. Stephenson, 1999. The "Normality" of El Niño. *Geophys. Res. Lett.*, **26**, 1027–1030.

Cane, M. A., 2005. The evolution of El Niño, past, present and future. *Earth and Planetary Science Letters*, **230**, 227–240.

Carton, J. A. and B. A. Giese, 2007. A reanalysis of ocean climate using SODA. *Submitted to Monthly Weather Review*.

Chagnon, S. A., 1999. Impacts of 1997-98 El Niño-generated weather in the United States. *Bulletin of the American Meteorological Society*, **80**, 1819–1827.

Clement, A. C., R. Seager and M. Cane, 1999. Orbital controls of the El Niño/Southern Oscillation and the tropical climate. *Paleoceanography*, **14**, 441–456.

Clement, A. C., R. Seager and M. Cane, 2000. Suppression of El Niño during the mid-Holocene by changes in the Eearth's orbit. *Paleoceanography*, **15**, 731–737.

Cobb, K., C. D. Charles, H. Cheng and R. L. Edwards, 2003. El Niño/Southern Oscillation and tropical Pacific climate during the last millennium. *Nature*, **424**, 271–276.

Cohen, A. and H. Jones, 1969. Regression on a random field. *J. Am. Stat. Assoc.*, **64**, 1172–1182.

Collins, M. and The CMIP Modeling Groups, 2005. El Niño- or la Niña-like climate change? *Clim. Dyn.*, **24**, 89–104.

Davey, M. K., M. Huddleston, K. Sperber, P. Braconnot, F. Bryan, D. Chen, A. Colman, U. Cubasch, C. Cooper, P. Delecluse, D. DeWitt, L. Fairhead, G. Flato, C. Gordon, T. Hogan, M. Ji, M. Kimoto, A. Kitoh, T. Knutson, M. Latif, H. Le Treut, T. Li, S. Manabe, C. Mechoso, G. A. Meehl, S. P. Power, E. Roeckner, L. Terray, I. Vintzileos, R. Voss, B. Wang, W. W., I. Yoshikawa, J. Yu, S. Yukimoto and S. Zebiak, 2002. STOIC: a study of coupled model climatology and variability in the tropical ocean regions. *Clim. Dyn.*, **18**, 403–420.

Delecluse, P., M. K. Davey, Y. Kitamura, S. G. H. Philander, M. Suarez and L. Bengtsson, 1998. Coupled general circulation modeling of the tropical Pacific. *J. Geophys. Res.*, **103**, 14357–14373.

Diaz, H. F., M. P. Hoerling and J. K. Eischeid, 2001. ENSO variability, teleconnections and climate change. *Int. J. Climatol.*, **21**, 1845–1862.

Dijkstra, H. D. and G. Burgers, 2002. Fluid dynamics of El Niño variability. *Annu. Rev. Fluid. Mech.*, **34**, 531–558.

Dijkstra, H. D. and J. D. Neelin, 1995. Ocean-atmosphere interactions and the tropical climatology. Part II: Why the Pacific cold tongue is in the east. *J. Climate*, **8**, 1343–1359.

Dijkstra, H. D. and J. D. Neelin, 1999. Ocean-atmosphere interactions and the tropical climatology. Part III: Instabilities of the fully coupled climatology. *J. Climate*, **12**, 1630–1643.

Dupuis, H., P. K. Taylor, A. Weill and K. Katsaros, 1997. Initial dissipation method applied to derive turbulent fluxes over the ocean during the Surface of the Ocean, Fluxes and Interactions with Atmosphere/Atlantic Stratocumulus Transition experiment (SOFIA/ASTEX) and Structure des Echanges Mer-Atmosphere, Propietes des Heterogeneites Oceaniques: Recherche Experimentale (SEMAPHORE) experiments with low to moderate wind speeds. *J. Geophys. Res.*, **102**, 21115–21129.

Eckert, C. and M. Latif, 1997. Predictability of a stochastically forced hybrid coupled model of the tropical ocean-atmosphere system. *J. Climate*, **10**, 1488–1504.

Fedorov, A. and S. G. H. Philander, 2000. Is El Niño changing? *Science*, **288**, 1997–2002.

Fedorov, A. and S. G. H. Philander, 2001. A stability analysis of tropical ocean-atmosphere interactions: Bridging measurements and theory for El Niño. *J. Climate*, **14**, 3086–3101.

Gibson, J. K., P. Kållberg, S. Uppala, A. Nomura, A. Hernandez and E. Serrano, 1997. ERA description. ECMWF re-analysis final rep. Technical Report 1, European Center for Medium Range forecasts.

Gill, A. G., 1983. *Atmosphere-Ocean Dynamics*. International Geophysics Series, Vol. 30.

Glantz, M. G., 2000. *Currents of Change. Impacts of El Niño and La Niña on Climate and Society.*. Cambridge University Press.

Goddard, L. and M. Dilley, 2005. El Niño: Catastrophe or opportunity. *J. Climate*, **18**, 651–665.

Halpern, D., 1988. Moored surface wind observations at four sites along the Pacific equator between 140°O and 95°W. *J. Climate*, **1**, 1251–1260.

Harrison, D. E., A. Rosati, B. J. Soden, E. Galanti and E. Tziperman, 2002. An evaluation of air-seas flux products of ENSO simulation and prediction. *Mon. Wea. Rev.*, **130**, 723–732.

Houghton, J. T., D. J. Ding, D. J. Griggs, M. Noguer, P. M. van der Linden, X. Dai, K. Maskell and C. A. Johnson, 2001. *Climate Change 2001: The Scientific Basis*. Cambridge University Press.

Jin, F.-F., 1997. An equatorial ocean recharge paradigm for ENSO. Part I: Conceptual model. *J. Atmos. Sci.*, **54**, 811–829.

Jin, F.-F., S. K. Kim and L. Bejarano, 2006. A coupled stability index for ENSO. *Geophys. Res. Lett.*, **33**, 1–4. L23708, doi:10.1029/2006GL027221.

Jin, F.-F. and D. Neelin, 1993. Modes of interannual tropical ocean-atmosphere interaction–a unified view. Part III: Analytical results in fully coupled cases. *J. Atmos. Sci.*, **50**, 3523–3540.

Jin, F.-F., D. Neelin and M. Ghil, 1994. ENSO on the devil's staircase. *Science*, **264**, 70–72.

Jones, P. D. and M. E. Mann, 2004. Climate over past millennia. *Rev. Geophys*, **42**, 1–42. RG2002.

Jungclaus, J. H., M. Botzet, H. Haak, N. Keenlyside, J.-J. Luo, M. Latif, J. Marotzke, U. Mikolajewicz and E. Roeckner, 2006. Ocean circulation and tropical variability in the coupled model ECHAM5/MPI-OM. *J. Climate*, **19**, 3952–3972.

Kalnay, E., M. Kanamitsu, R. Kistler, W. Collins, D. Deaven, L. Gandin, M. Iredell, S. Saha, G. White, J. Woollen, Y. Zhu, M. Chelliah, W. Ebisuzaki, W. Higgins, J. Janowiak, K. C. Mo, C. Ropelewski, J. Wang, A. Leetmaa, R. Reynolds, R. Jenne and D. Joseph, 1996. The NCEP/NCAR 40-year reanalysis project. *Bull. Amer. Meteor. Soc.*, **77**, 437–470.

Kelly, K. A., S. Dickinson, M. J. McPhaden and G. Johnson, 2001. Ocean currents evident in satellite wind data. *Geophys. Res. Lett.*, **28**, 2469–2472.

Kessler, W., 2002. Is ENSO a cycle or a series of events? *Geophys. Res. Lett.*, **29**, 2125–2129.

Landsea, C. W. and J. Knaff, 2000. How much skill was there in forecasting the very strong 1997-98 El Niño? *Bulletin of the American Meteorological Society*, **91**, 2107–2119.

Large, W. G. and S. G. Pond, 2004. Diurnal to decadal global forcing for ocean and sea-ice models: the data sets and flux climatologies. NCAR Technical Note, NCAR, Boulder, Colorado. NCAR/TN-460+STR.

Latif, M., D. Anderson, T. Barnett, M. Cane, R. Kleeman, A. Leetmaa, J. O'Brien, A. Rosati and E. Schneider, 1998. A review of the predictability and prediction of ENSO. *J. Geophys. Res.*, **103**, 14375–14393.

Latif, M. and M. Fluegel, 1991. An investigation of short-range climate predictability in the tropical Pacific. *J. Geophys. Res.*, **96**, 2661–2673.

Latif, M., K. Sperber, J. M. Arblaster, P. Braconnot, D. Chen, A. Colman, U. Cubasch, C. Cooper, P. Delecluse, D. DeWitt, L. Fairhead, G. Flato, T. Hogan, M. Ji, M. Kimoto, A. Kitoh, T. Knutson, H. Le Treut, T. Li, S. Manabe, O. Marti, C. Mechoso, G. A. Meehl, S. P. Power, E. Roeckner, J. Sirven, L. Terray, I. Vintzileos, R. Voss, B. Wang, W. W., I. Yoshikawa, J. Yu and S. Zebiak, 2001. ENSIP: the El Niño intercomparison project. *Clim. Dyn.*, **18**, 255–276.

Latif, M. and A. Villwock, 1990. Interannual variability as simulated in a coupled ocean-atmosphere models. *J. Mar. Syst.*, **1**, 51–60.

Levitus, S. and T. Boyer, 1994. World Ocean Atlas 1994: Vol. 4: Temperature. NOAA Atlas NESDIS 4, NOAA, U.S. Gov. Printing Office, Wash., D.C.

Lohmann, K. and M. Latif, 2005. Pacific decadal variability and the subtropical-tropical cells. *J. Climate*, **18**, 5163–5178.

Luo, J.-J., S. Mason, E. Roeckner, M. Madec and T. Yamagata, 2005. Reducing climatology bias in an ocean-atmosphere CGCM with improved coupling physics. *J. Climate*, **18**, 2344–2360.

Maćias, J., 2000. *ENSO and seasonal variability in a hybrid coupled model of the tropical Pacific*. Grupo de Ecuaciones Diferenciales, Analisis Numérico y Alicaciones de la Universidad de Málaga.

Maćias, J., D. B. Stephenson and A. Kearsley, 1999. A basic reference state suitable for anomaly-coupled ocean-atmosphere climate models. *App. Math. Lett.*, **12**, 21–24.

Mann, M. E., M. A. Cane, S. E. Zebiak and A. Clement, 2005. Volcanic and solar forcing of the tropical Pacific over the past 1000 years. *J. Climate*, **18**, 447.

Mann, M. E. and P. D. Jones, 2003. Global surface temperature over the past two millennia. *Geophys. Res. Lett.*, **30(15)**, 1–4. 1820, doi:10.1029/2003GL01784.

Marsland, S. J., H. Haak, J. H. Jungclaus, M. Latif and F. Röske, 2003. The Max-Planck-Institute global ocean/sea ice model with orthogonal curvilinear coordinates. *Ocean Modelling*, **5**, 91–127.

Matei, D., 2007. *Pacific Decadal Variability: Internal Variability and Sensitivity to the Subtropics*. Ph.D. thesis, University of Hamburg, Germany.

McPhaden, M. J., 2004. The evolution of the 2002/03 El Niño. *Bull. Amer. Meteor. Soc.*, pp. 677–695. Doi: 10.1175/BAMS-85-5-677.

McPhaden, M. J., A. J. Busalacci, R. Cheney, J.-R. Donguy, K. S. Gage, D. Halpern, M. Ji, P. Julian, G. Meyers, M. G. T., P. P. Niiler, J. Picaut, R. W. Reynolds, N. Smith and K. Takeuchi, 1998. The Tropical Ocean-Global Atmosphere observing system: A decade of progress. *J. Geophys. Res.*, **103**, 14169–14240.

Mechoso, C., J. Neelin and J.-Y. Yu, 2003. Testing simple models of ENSO. *J. Atmos. Sci.*, **60**, 305–318.

Meehl, G. A., P. R. Gent, J. M. Arblaster, B. Otto-Bliesner, E. Brady and A. Craig, 2001. Factors that affect the amplitude of El Nino in global coupled climate models. *Clim. Dyn.*, **17**, 515–526.

Meinen, C. and M. McPhaden, 2000. Observations of warm water volume changes in the equatorial Pacific and their relationship to El Niño and La Niña. *J. Climate*, **13**, 3551–3559.

Meinen, C., M. McPhaden and G. C. Johnson, 2001. Vertical velocities and transports in the equatorial Pacific during 1993-99. *J. Phys. Oceanogr.*, **31**, 3230–3248.

Merkel, U., 2003. *ENSO teleconnections in high resolution experiments*. Ph.D. thesis, University of Hamburg, Germany.

Moy, C. M., G. O. Seltzer, D. T. Rodbell and D. M. Anderson, 2002. Variability of El Niño/Southern Oscillation activity at millennial timescales during the Holocene epoch. *Nature*, **420**, 162–165.

Neelin, J. D., 1990. A hybrid coupled general circulation model for El Ninño studies. *J. Atmos. Sci.*, **47**, 674–693.

Neelin, J. D., D. S. Battisti, A. C. Hirst, F.-F. Jin, Y. Wakata, T. Yamagata and S. E. Zebiak, 1998. ENSO theory. *J. Geophys. Res.*, **103**, 14261–14290.

Office of Global Programs, 1999. An experiment in the application of climate forecasts: NOAA-OGP activities related to the 1997-98 El Niño event. *NOAA Office of Global Programs*, **18**.

Pacanowski, R. C., 1987. Effect of equatorial currents on surface stress. *J. Phys. Oceanogr.*, **17**, 833–838.

Peixoto, J. P. and A. H. Oort, 1992. *Physics of Climate*. American Inst. of Physics, New York.

Pezzulli, S., D. B. Stephenson and A. Hannachi, 2005. The variability of seasonality. *J. Climate*, **18**, 71–88.

Philander, S. G. H., 1990. *El Niño, La Niña,and the Southern Oscillation*. Academic Press, San Diego.

Philander, S. G. H., 2003. Is El Niño sporadic or cyclic. *Annu. Rev. Earth Planet. Sci.*, **32**, 579–594.

Picaut, J., F. Masia and Y. du Penhoat, 1997. An advective-reflective conceptual model for the oscillatory nature of the ENSO. *Science*, **277**, 663–666.

Preisendorfer, R. W., 1988. *Principal Component Analysis in Meteorology and Oceanography (Developments in Atmospheric Science, Vol 17)*. Elsevier Science Ltd.

Rasmussen, E. and T. Carpenter, 1982. Variations in the tropical sea surface temperature and surface wind field associated with the Southern Oscillation/El Niño. *Mon. Wea. Rev.*, **110**, 354–384.

Rayner, N. A., D. E. Parker, E. B. Holton, C. K. Folland, L. V. Alexander, D. P. Rowell, E. C. Kent and A. Kaplan, 2003. Global analysis of sea surface temperature, sea ice, and night marine air temperature since the late nineteenth century. *J. Geophys. Res.*, **108(D14)**. 4407, doi:10.1029/2002JD002670.

Reverdin, G., C. Frankignoul, E. Kestenare and M. J. McPhaden, 1994. Seasonal variability in the surface currents of the equatorial Pacific. *J. Geophys. Res.*, **99**, 20323–20344.

Reynolds, R. W. and T. M. Smith, 1994. Improved global sea surface temperature analysis using optimum interpolation. *J. Climate*, **7**, 928–948.

Rodbell, D. T., G. O. Seltzer, D. M. Anderson, M. B. Abbott, D. B. Enfield and J. H. Newman, 1999. An 15,000- year record of El Niño-driven alluviation in southwestern Ecuador. *Science*, **283**, 516–520.

Rodgers, K. B., P. Friedrichs and M. Latif, 2004. Tropical Pacific decadal variability and its relationship to decadal modulation of ENSO. *J. Climate*, **17**, 3761–3774.

Rodó, X. and M.-A. Rodriguez-Arias, 2003. El Niño-Southern Oscillation:absent in the early Holocene? *J. Climate*, **17**, 423–226.

Röske, F., 2001. An atlas of surface fluxes based on the ECMWF Re-Analysis - a climatological dataset to force global ocean general circulation models. Report 323, Max-Planck-Institut für Meteorologie, Hamburg, Germany.

Röske, F., 2006. A global heat and freshwater forcing dataset for ocean models. *Ocean Modelling*, **11**, 235–297.

Schopf, P. and M. Suarez, 1988. Vacillations in a coupled ocean-atmosphere model. *J. Atmos. Sci.*, **45**, 3283–3287.

Smith, S. D., 1980. Wind stress and heat flux over the ocean in gale force winds. *J. Phys. Oceanogr.*, **10**, 709–726.

Smith, S. D., 1988. Coefficients for sea-surface wind stress, heat flux, and wind profiles as a function of wind speed and temperature. *J. Geophys. Res.*, **93**, 15476–15472.

Stewart, R. H., 2002. *Introduction to Physical Oceanography*. Texas A & M University.

Stockdale, T. N., A. J. Busalacchi, D. E. Harrison and R. Seager, 1998. Ocean modelling for ENSO. *J. Geophys. Res.*, **103**, 14325–14355.

Stricherz, J. N., D. M. Legler and J. J. O'Brien, 1997. TOGA pseudo-stress atlas 1985-1994, Volume II: Pacific ocean. Technical report, Florida State University, Tallahassee, Florida.

Syu, H.-H., J. D. Neelin and D. Gutzler, 1995. Seasonal and interannual variability in a hybrid coupled GCM. *J. Climate*, **8**, 2121–2143.

Tang, Y., W. W. Hsieh, B. Tang and K. Haines, 2001. A neural network atmospheric model for hybrid coupled modelling. *Clim. Dyn.*, **17**, 445–455.

Timmermann, A., F.-F. Jin and M. Collins, 2004. Intensification of the annual cycle in the tropical Pacific due to greenhouse warming. *Geophys. Res. Lett.*, **31**, 1–4. L12208, doi: 10.1029/2004GL019442.

Timmermann, A., J. Oberhuber, A. Bacher, M. Esch, M. Latif and E. Roeckner, 1999. Increased El Niño frequency in a climate model forced by future greenhouse warming. *Nature*, **398**, 694–697.

Trenberth, K. E., 1997. The definition of El Niño. *Bulletin of the American Meteorological Society*, **78**, 2771–2777.

Trenberth, K. E., G. W. Branstator, D. Karoly, A. Kumar, N.-C. Lau and C. Ropelewski, 1998. Progress during TOGA in understanding and modelling global teleconnections associated with tropical seas surface temperature. *J. Geophys. Res.*, **103**, 14291–14324.

Trenberth, K. E., G. Large and J. Olson, 1989. The effective drag coefficient for evaluating wind stress over the oceans. *J. Climate*, **2**, 1507–1516.

Tudhope, A. W., C. P. Chilcott, M. T. McCulloch, E. R. Cook, J. Chappell, R. M. Ellam, D. W. Lea, J. M. Lough and G. B. Shimield, 2001. Variability in the El Niño-Southern Oscillation through a glacial-interglacial cycle. *Science*, **291**, 1511–1516.

Tziperman, E., L. Stone, M. Cane and H. Jarosh, 1994. El Niño chaos: Overlapping of resonances between the seasonal cycle and the Pacific ocean atmosphere oscillator. *Science*, **264**, 72–74.

Tziperman, E., S. E. Zebiak and M. Cane, 1997. Mechanisms of seasonal - ENSO interactions. *J. Atmos. Sci.*, **54**, 61–71.

Uppala, S., 2001. ECMWF reanalysis, 1957-2001. Technical Report 10, European Center for Medium Range forecasts.

van Oldenborgh, G. J., S. Philip and M. Collins, 2005. El Niño in a changing climate: a multi-model study. *Ocean Science Discussions, www.ocean-science.net/osd/2/267/*, **2**, 267–298.

von Storch, H. and F. Zwiers, 1999. *Statistical Analysis in Climate Research*. Cambridge University Press.

Walker, G. T., 1924. Correlation in seasonal variations of weather. IX. A further study of world weather. *Mem. India Meteorol. Dep.*, **24**, 275–332.

Wang, B. and S.-I. An, 2001. Why the properties of El Niño changed during the late 1970s. *Geophys. Res. Lett.*, **28**, 3709–3712.

Wang, C., 2001. A unified oscillator model for the El Niño-Southern Oscillation. *J. Climate*, **14**, 98–115.

Wilson, S., 2000. How ocean vertical accumulation of warm surface water influence the "sharpness" of the equatorial thermocline. *J. Climate*, **13**, 3638–3656.

Wu, J., 1994. The sea surface is aerodynamically rough even under light winds. *Boundary Layer Meteorology*, **69**, 149–158.

Wyrtki, K., 1975. El Nino–the dynamic response of the equatorial Pacific ocean to atmosphere forcing. *J. Phys. Oceanogr.*, **5**, 572–584.

Xie, S.-P., 1995. Interactions between the annual and interannual variations in the equatorial Pacific. *J. Phys. Oceanogr.*, **25**, 1930–1940.

Yan, X.-H., C.-R. Ho, Q. Zheng and V. Klemas, 1992. Temperature and size variabilities of the Western Pacific Warm Pool. *Science*, **258**, 1643–1645.

Yeh, S.-W. and B. P. Kirtman, 2005. Pacific decadal variability and decadal ENSO amplitude modulation. *Geophys. Res. Lett.*, **132**, 1–5. L05703, doi:10.1029/2004GL02173.

Yeh, S.-W. and B. P. Kirtman, 2006. Origin of decadal El Niño-Southern Oscillation-like variability in a coupled general circulation model. *J. Geophys. Res.*, **111**, 1–12. C01009, doi:10.1029/2005JC002985.

Yelland, M., B. I. Moat, P. K. Taylor, R. Pascal, J. Hutchings and V. Cornell, 1998. Wind stress measurements from the open ocean corrected for airflow distortion by the ship. *J. Phys. Oceanogr.*, **28**, 1511–1526.

Yelland, M. and P. K. Taylor, 1996. Wind stress measurements from the open ocean. *J. Phys. Oceanogr.*, **26**, 541–558.

Zebiak, S. E. and M. A. Cane, 1987. A model for El Niño-Southern Oscillation. *Mon. Wea. Rev.*, **115**, 2262–2278.

# Acknowledgments